

# Combustion instabilities in combined cycle gas turbines

Analysis and modelling of the impact of operating conditions on combustion instability

R.C.A. Voets



# Combustion instabilities in combined cycle gas turbines

Analysis and modelling of the impact of operating  
conditions on combustion instability

by

R.C.A. (Roel) Voets

to obtain the degree of **Master of Science** in

**Mechanical Engineering**

at the Delft University of Technology,  
to be defended publicly on Friday April 24, 2020 at 1:00 PM.

Student number: 4216067  
Thesis committee: Prof. dr. ir. S.A. Klein, TU Delft, supervisor  
Dr. ir. J.W.R. Peeters, TU Delft  
Dr. ir. R. Pecnik, TU Delft  
T.D. van Ketel, Vattenfall

Delft University of Technology  
Faculty of Mechanical, Maritime and Materials Engineering  
Department of Process and Energy  
Section of Gas Turbines

An electronic version of this thesis is available at <http://repository.tudelft.nl/>.



# Preface

This thesis will be my final project to conclude my Master of Science program for Mechanical Engineering at the Delft University of Technology. When I started with my bachelor studies in Industrial Design Engineering, I did not expect to end up writing my master thesis on a subject like this. I have learned a whole lot over the last year, in Matlab, (thermo-)acoustics, one-dimensional waves, but most of all in the world of combined cycle gas turbines. Grasping the complex dynamics of the combustion instabilities in a gas turbine has proven to be challenging, but also rewarding when looking back to the progress made.

I would firstly like to express my sincerest gratitude to Sikke Klein, for all his help in guiding me in the right direction, while also keeping me motivated throughout my thesis process. His knowledge and both in-depth and clear explanations of combustion dynamics have been very helpful during this entire process. I would also like to thank Jurriaan Peeters and Rene Pecnik for taking part in my thesis committee.

I would also like to thank Vattenfall for providing me with the ability to perform my thesis project at a very interesting and ambitious company. Special thanks go out to Willem van der Valk, for allowing me to work in your department and providing me with a very warm and pleasant place to work. This also applies to the entire Technical Training Centre department at Vattenfall, you all made me feel very welcome. Also thanks to Taco van Ketel, for providing your guidance on the content of my thesis and pointing me in the interesting directions for research into the combustion dynamics. In addition I would like to thank Frederik Aalbersberg, for your support in both data collection for the combustion dynamics and your knowledge about the sensitivities of the SGT5-4000F. Lastly I would like to thank André van Beelen for allowing me to do both my internship and master thesis on this interesting subject.

Thanks to my family, who have supported me throughout my entire time of studying and for supporting me in my decision to switch towards a master studies in Mechanical Engineering. Also thanks to all my friends, for making my time in Delft and Rotterdam as a student very special and truly unforgettable. Enjoy reading my thesis.

*R.C.A. (Roel) Voets  
Rotterdam, April 2020*



# Abstract

With increasing discussion and legislation around emissions, gas turbines have evolved to limit their emissions, especially  $\text{NO}_x$  emissions. The way of operating the gas turbine, with lean premixed combustion reduces the flame temperature in the combustion chamber which results in low  $\text{NO}_x$  emissions. The downside of this way of operating is the increased sensitivity of the combustion system to thermo-acoustic instabilities. These instabilities arise due to an interaction between unsteady heat release at the flame and the acoustics of the combustion system. At lean premixed conditions, a fluctuation in equivalence ratio results in a large fluctuation in flame speed which is related to the heat release. This makes the lean premixed combustion very susceptible to acoustic pressure waves travelling through and reflecting inside the combustion system, as these pressure waves can influence the mass flow of gas and air in the premixing duct and thus changing the composition of the fuel mixture that is convected towards the flame. An additional effect to the unsteady heat release are fluctuations of the total mass flow at the burner outlet, which are convected towards the flame front, an increase in combusted fuel will result in an increase in heat release.

To analyze the sensitivities of the combustion system, a thermo-acoustic model will be constructed. The model will be a one-dimensional and linearised system, where conservation equations across the (thermo-)acoustic elements of the combustion system are rewritten into transfer matrix form. Validation will be done by analyzing operational data from the HW09 power plant and comparing this with the model response. The combustion dynamics are analysed for frequencies in the range 0 - 300 Hz.

It was found that the HW09 is susceptible to combustion instabilities when the pressure drop across the premix gas nozzles is low, which results in a decrease in fuel supply impedance. This increases the pressure amplitude in the 90 Hz range, this behaviour corresponds to the modelled results when changes to the gas preheating temperature or fuel nozzle compositions are made in the thermo-acoustic model, which influence the pressure drop over the gas nozzles. This is accompanied with a decreased amplification at the critical 120 Hz range. This is a known side-effect, as the 90 Hz needs to remain dominant for a stable combustion system. This means the pressure drop over the gas nozzles balances on a fine line, too low will result in high 90 Hz pressure waves and too high will result in a more unstable 120 Hz frequency.

Several of the hybrid burners in the annular combustion chamber are fitted with a cylindrical burner outlet. This changes the flow field out of the burner and is used to allow a higher maximum load for the gas turbine. The inclusion of this burner ring makes the combustion system upstream of the burner outlet more resistant to acoustic pressure fluctuations in the frequency range up to 120 Hz. The burner system does become more sensitive to acoustic pressure fluctuations for frequencies higher than 120 Hz.

Fuel composition influences the combustion behaviour of a fuel mixture. Low-calorific fuel shows to be inherently more unstable in this gas turbine configuration as opposed to high-calorific fuel. If hydrogen is added to high-calorific fuel, the flame speed is increased as is the influence of both equivalence ratio perturbations and velocity perturbations on unsteady heat release. The increase in flame speed results in a reduction of flame length, which changes the convective time delay and shifts the instability of the combustion system from the 120 Hz area towards the 180 Hz area.

The thermo-acoustic model responds to changes of operational parameters in an equal manner as was found from data analysis. The results are comparable up to 200 Hz, after which the flame can no longer be assumed to be compact, which means compressibility, 2D and 3D effects have to be taken into account. Fuel composition analysis shows the importance of flame length and convective time delay on combustion stability. For hydrogen addition it can shift the critical frequency towards the second harmonic frequency of the combustion chamber, this will result in rapidly increasing pressure waves and high accelerations. With increased knowledge of the effects of hydrogen addition or low-calorific fuel on the flame dynamics, the model can be a predictive tool to investigate the combustion behaviour when the change to this fuel mixture will be made. The ability to predict the influence of different operational parameters or changes to burner geometry on the stability of the combustion system can be very beneficial for analysis of future changes to the gas turbine and its operation.



# Contents

<b>Preface</b>	<b>iii</b>
<b>Abstract</b>	<b>v</b>
<b>List of Figures</b>	<b>xi</b>
<b>List of Tables</b>	<b>xv</b>
<b>1 Introduction</b>	<b>1</b>
1.1 Energy generation in gas turbines . . . . .	1
1.1.1 Combined cycle power plants . . . . .	1
1.1.2 Combustion instabilities in combined cycle power plants . . . . .	3
1.2 Problem statement . . . . .	3
1.3 Research objective . . . . .	4
1.3.1 Research questions . . . . .	4
1.3.2 Scope . . . . .	4
1.4 Thesis outline . . . . .	5
<b>2 Literature review</b>	<b>7</b>
2.1 Acoustics . . . . .	7
2.1.1 Introduction . . . . .	7
2.1.2 Analogy of Lighthill . . . . .	7
2.1.3 The flame as a source of sound. . . . .	8
2.2 Acoustic wave solution . . . . .	9
2.2.1 Homogeneous wave equation . . . . .	9
2.2.2 Convective homogeneous wave equation . . . . .	9
2.2.3 One dimensional wave solutions. . . . .	9
2.2.4 Harmonic wave solutions . . . . .	10
2.3 Combustion. . . . .	11
2.3.1 Introduction . . . . .	11
2.3.2 Combustion process . . . . .	11
2.3.3 Equivalence ratio . . . . .	12
2.3.4 Combustor types. . . . .	12
2.3.5 Lean premixed combustion . . . . .	13
2.3.6 Gas composition. . . . .	13
2.4 Thermo-acoustic combustion instabilities . . . . .	15
2.4.1 Introduction . . . . .	15
2.4.2 Physics of combustion instabilities . . . . .	15
2.4.3 Rayleigh's Instability Criterion . . . . .	16
2.4.4 Energy loss in the combustion system . . . . .	16
2.4.5 Characteristic time-delay and phasing analysis . . . . .	17
2.5 Transfer matrix method. . . . .	18
2.5.1 Introduction . . . . .	18
2.5.2 Transfer matrix element structure . . . . .	18
2.5.3 Element for an acoustic duct. . . . .	18
2.5.4 Element for an area change . . . . .	19
2.5.5 Element for a junction . . . . .	20
2.5.6 Element for a Helmholtz resonator. . . . .	21
2.5.7 Acoustic boundary conditions . . . . .	23

2.6	Flame transfer function . . . . .	25
2.6.1	Introduction . . . . .	25
2.6.2	Conservation equations . . . . .	25
2.6.3	$n - \tau$ method for flame transfer function. . . . .	27
2.6.4	Flame transfer function . . . . .	27
2.6.5	Flame transfer function response . . . . .	31
2.6.6	Unsteady heat release . . . . .	32
2.6.7	Flame transfer matrix . . . . .	33
<b>3</b>	<b>Transfer matrix method validation</b>	<b>35</b>
3.1	Introduction . . . . .	35
3.2	Thermo-acoustics of a Rijke Tube. . . . .	35
3.2.1	Introduction . . . . .	35
3.2.2	Model set-up. . . . .	35
3.2.3	Rijke tube stability . . . . .	37
3.3	Simple combustor model . . . . .	38
3.3.1	Introduction . . . . .	38
3.3.2	Combustor geometry . . . . .	38
3.3.3	Acoustic combustor model stability . . . . .	38
3.3.4	Thermo-acoustic combustor model stability. . . . .	40
3.4	Reflection factor validation . . . . .	42
3.4.1	Introduction . . . . .	42
3.4.2	Methodology. . . . .	42
3.4.3	Magnitude reflection factor . . . . .	43
3.4.4	Time delay influence. . . . .	44
3.4.5	Reflection factor as input . . . . .	45
<b>4</b>	<b>Vattenfall operated SGT5-4000F plants</b>	<b>47</b>
4.1	SGT5-4000F combined cycle power plant . . . . .	47
4.1.1	Annular hybrid burner ring . . . . .	48
4.1.2	Cylindrical burner outlet. . . . .	49
4.2	Combustion monitoring at Vattenfalls gas turbines . . . . .	49
4.2.1	Stability margin controller . . . . .	50
4.3	Combustion instabilities prevention . . . . .	51
4.3.1	Influence of fuel preheating temperature . . . . .	51
4.3.2	Influence of premix gas nozzles . . . . .	51
4.3.3	Influence of cylindrical burner outlet . . . . .	52
<b>5</b>	<b>Cold flow model hybrid burner</b>	<b>53</b>
5.1	Network model hybrid burner . . . . .	53
5.2	Burner impedance . . . . .	55
5.3	Burner validation . . . . .	56
<b>6</b>	<b>Thermo-acoustic model SGT5-4000F</b>	<b>59</b>
6.1	Thermo-acoustic network model . . . . .	59
6.2	Flame transfer matrix element . . . . .	59
6.3	Expected (un)stable frequencies . . . . .	61
6.4	Model set-up . . . . .	61
6.4.1	Burner and flame reflection factor . . . . .	61
6.4.2	Reflection factor response . . . . .	61
6.4.3	Thermo-acoustic model . . . . .	62
6.4.4	Stability plot . . . . .	63
6.5	Reflection factor sensitivity . . . . .	64
6.5.1	Introduction . . . . .	64
6.5.2	Flame length influence. . . . .	64
6.5.3	Time delay influence. . . . .	65
6.5.4	Flame speed influence. . . . .	66
6.5.5	Flame length influence. . . . .	67

6.5.6	Conclusion . . . . .	68
<b>7</b>	<b>Case studies</b>	<b>69</b>
7.1	Fuel preheating temperature . . . . .	69
7.1.1	Gas supply impedance . . . . .	70
7.1.2	Unsteady heat release . . . . .	71
7.1.3	Reflection factor . . . . .	72
7.1.4	Stability plot . . . . .	72
7.1.5	Pressure spectra . . . . .	73
7.1.6	Conclusion and discussion. . . . .	74
7.2	Premix burner modification. . . . .	75
7.2.1	Gas supply impedance . . . . .	76
7.2.2	Unsteady heat release . . . . .	76
7.2.3	Reflection factor . . . . .	77
7.2.4	Stability plot . . . . .	78
7.2.5	Pressure spectra . . . . .	78
7.2.6	Conclusion and discussion. . . . .	79
7.3	Cylindrical burner outlet . . . . .	80
7.3.1	Cold flow burner impedance. . . . .	81
7.3.2	Unsteady heat release . . . . .	81
7.3.3	Reflection factor . . . . .	82
7.3.4	Stability plot . . . . .	83
7.3.5	Pressure spectrum . . . . .	83
7.3.6	Conclusion and discussion. . . . .	84
7.4	Low calorific fuel . . . . .	85
7.4.1	Gas supply impedance . . . . .	85
7.4.2	Unsteady heat release . . . . .	86
7.4.3	Reflection factor . . . . .	86
7.4.4	Stability plot . . . . .	87
7.4.5	Conclusion and discussion. . . . .	88
7.5	Hydrogen addition . . . . .	89
7.5.1	Unsteady heat release . . . . .	89
7.5.2	Reflection factor . . . . .	90
7.5.3	Stability plot . . . . .	91
7.5.4	Conclusion and discussion. . . . .	91
<b>8</b>	<b>Conclusion and recommendations</b>	<b>93</b>
8.1	Conclusion . . . . .	93
8.2	Recommendations . . . . .	95
8.2.1	Thermo-acoustic model . . . . .	95
8.2.2	Further research . . . . .	96
	<b>Bibliography</b>	<b>97</b>
<b>A</b>	<b>Thermo-acoustic source term</b>	<b>105</b>
<b>B</b>	<b>Fuel temperature influence</b>	<b>109</b>
<b>C</b>	<b>Fuel supply sensitivity</b>	<b>111</b>
<b>D</b>	<b>Acoustics of a clarinet</b>	<b>113</b>



# List of Figures

1.1	Electricity production in the Netherlands from 2000 onwards . . . . .	1
1.2	Schematic representation of combined cycle gas turbine system . . . . .	2
1.3	Vattenfalls combined cycle power plant in Amsterdam - HW09 . . . . .	2
1.4	Vattenfalls combined cycle power plant in Diemen - DM34 . . . . .	2
1.5	CO and NO <sub>x</sub> emissions versus combustion temperature [36] . . . . .	3
1.6	Damaged cover on a gas turbine burner due to excessive combustion dynamics [24] . . . . .	3
1.7	Laminar flame speed vs equivalence ratio at STP; Points, experiments; Lines, modeling by Dirrenberger [9] . . . . .	4
1.8	Acoustic coupling with heat release [33] . . . . .	4
1.9	Schematic overview of thesis outline . . . . .	5
2.1	Wave propagation in simple cylindrical duct . . . . .	10
2.2	Siemens SGT5-4000F Gas turbine . . . . .	11
2.3	Ideal Brayton cycle . . . . .	12
2.4	Rolls-Royce can-type combustor [7] . . . . .	13
2.5	Annular combustor [2] . . . . .	13
2.6	Laminar flame speed versus equivalence ratio; 50% CH <sub>4</sub> :50%H <sub>2</sub> fuel mixture [30] . . . . .	14
2.7	Laminar flame speed versus equivalence ratio; 10% CH <sub>4</sub> :90%H <sub>2</sub> fuel mixture [30] . . . . .	14
2.8	Interactions within combustion system - flame as an active source of sound [33] . . . . .	15
2.9	Thermodynamic interpretation of Rayleigh's stability criterion [33] . . . . .	16
2.10	Evolution of pressure disturbances in an LNGT combustor [25] . . . . .	17
2.11	Representation of pressure disturbances through combustor system . . . . .	17
2.12	Transfer matrix element . . . . .	18
2.13	Cylindrical duct with nodes 1 and 2, at these nodes to duct can be coupled to other elements . . . . .	19
2.14	Area change element . . . . .	19
2.15	T-junction element . . . . .	20
2.16	Helmholtz Resonator with mean flow . . . . .	21
2.17	Choked nozzle outlet . . . . .	24
2.18	Choked nozzle inlet . . . . .	24
2.19	Thin premixed, compact flame; 1 denotes pre-combustion conditions; 2 denotes post-combustion conditions . . . . .	25
2.20	Simple combustor interpretation showing the perturbations convecting through the system . . . . .	28
2.21	Laminar flame speed of a methane/air mixture as a function of the equivalence ratio at various temperatures and atmospheric pressure; symbols - experimental data; lines - modelled data; from Wu et al. [45] . . . . .	29
2.22	Laminar flame speed of a methane/air mixture as a function of the equivalence ratio at various pressure and room temperature; symbols - experimental data; lines - empirical correlation; from Distaso [10] . . . . .	29
2.23	Direct and indirect influence of equivalence ratio fluctuations on heat release . . . . .	29
2.24	Conical flame on burner outlet, fluctuating flame position . . . . .	30
2.25	Direct influence of velocity fluctuations at burner outlet on heat release . . . . .	30
2.26	Flame transfer function magnitude for $\phi = 0.5$ versus Strouhal number . . . . .	31
2.27	Flame transfer function phase for $\phi = 0.5$ versus Strouhal number . . . . .	31
2.28	Flame transfer function magnitude for $\phi = 0.5$ versus frequency . . . . .	31
2.29	Flame transfer function phase $\phi = 0.5$ versus frequency . . . . .	31
2.30	Simple combustor interpretation with nodes of perturbation; a - air; g - gas; b - burner outlet; f - downstream of flame . . . . .	33
3.1	Rijke tube geometry; heat release zone in upstream half of the cylindrical duct . . . . .	35

3.2	Rijke tube network model . . . . .	36
3.3	Simple combustor model [12] . . . . .	38
3.4	Stability plot from [12] compared with modelled stability . . . . .	39
3.5	Stability plot from [12] compared with modelled stability . . . . .	40
3.6	Simple combustor model from Dowling & Stow [12] with acoustic waves at flame front . . . . .	42
3.7	Reflection factor used as input in combustion chamber; 1 left boundary; 2 passive sound source; 3 right boundary . . . . .	42
3.8	Flame and burner system reflection factor; Lieuwen [6] flame model . . . . .	43
3.9	Stability plot; Lieuwen [6] flame model; Dowling [12] combustor model . . . . .	43
3.10	Influence of convective time-delay from burner outlet on reflection factor magnitude . . . . .	44
3.11	Influence of convective time-delay from burner outlet on stability plot . . . . .	44
3.12	Full system model pressure spectrum at 0.2 m in combustion chamber . . . . .	45
3.13	Reflection factor model pressure spectrum at 0.2m in combustion chamber . . . . .	45
4.1	SGT5-4000F Gas turbine . . . . .	47
4.2	Sketch of the SGT5-4000F annular combustion chamber [17] . . . . .	48
4.3	Hybrid burner layout - without CBO [42] . . . . .	48
4.4	CBO fitted to the final hybrid burner [42] . . . . .	49
4.5	Harmonic frequencies of annular combustion chamber . . . . .	49
4.6	Reacting flowfield for burner configurations with no CBO, a short CBO or a long CBO [22] . . . . .	52
5.1	Acoustic network model of the hybrid burner . . . . .	53
5.2	Geometric model of single burner with connection to annular combustion chamber . . . . .	54
5.3	Interpretation of Siemens hybrid burner model with numbers indicating nodes . . . . .	54
5.4	Comparison of magnitude and phase of burner impedance in the gas turbine combustion system from Kruger et al. [23] and modelled results . . . . .	56
6.1	Acoustic network model of the hybrid burner with feedback . . . . .	59
6.2	Geometrical representation of the hybrid burner with feedback . . . . .	60
6.3	Initial reflection factor magnitude response for HW09 combustion system . . . . .	62
6.4	Initial reflection factor phase response for HW09 combustion system . . . . .	62
6.5	Graphical representation of burner fitted into combustion chamber . . . . .	62
6.6	Pressure node (black) and pressure anti-node (red); system will be modelled at pressure node with input modelled at 1 . . . . .	62
6.7	Stability plot HW09 burner; negative growth rate is unstable . . . . .	63
6.8	Reflection factor magnitude for different flame lengths . . . . .	64
6.9	Reflection factor phase for different flame length . . . . .	64
6.10	Reflection factor magnitude for different time-delay correction factors . . . . .	65
6.11	Reflection factor phase for different time-delay correction factors . . . . .	65
6.12	Influence of $K_c$ on flame speed versus equivalence ratio . . . . .	66
6.13	Reflection factor magnitude for different correction factors . . . . .	66
6.14	Reflection factor phase for different correction factors . . . . .	66
6.15	Reflection factor magnitude for different flame lengths . . . . .	67
6.16	Reflection factor phase for different flame lengths . . . . .	67
6.17	Pressure spectrum 80 - 280 Hz for different flame lengths . . . . .	67
6.18	Pressure spectrum around 95 Hz for different flame lengths . . . . .	68
6.19	Pressure spectrum around 185 Hz for different flame lengths . . . . .	68
7.1	Impedance gas supply for different fuel temperatures . . . . .	70
7.2	Magnitude of unsteady heat release due to equivalence ratio fluctuations . . . . .	71
7.3	Phase of unsteady heat release due to equivalence ratio fluctuations . . . . .	71
7.4	Magnitude of unsteady heat release due to velocity fluctuations at the burner mouth . . . . .	71
7.5	Phase of unsteady heat release due to velocity fluctuations at the burner mouth . . . . .	71
7.6	Fuel preheating temperature influence on reflection factor magnitude . . . . .	72
7.7	Fuel preheating temperature influence on reflection factor phase . . . . .	72
7.8	Fuel preheating temperature influence on stability plot . . . . .	72
7.9	Pressure spectrum between 80 - 280 Hz for different fuel preheating temperatures . . . . .	73

7.10	Fuel preheating temperature influence on pressure amplitude in FB2 . . . . .	73
7.11	Fuel preheating temperature influence on pressure amplitude in FB5 . . . . .	73
7.12	Fuel preheating temperature influence on pressure amplitude in FB7 . . . . .	73
7.13	Normalized pressure amplitude versus relative power at FB2 and FB3 [41] . . . . .	75
7.14	Impedance gas supply for different nozzle configurations . . . . .	76
7.15	Magnitude of unsteady heat release due to equivalence ratio fluctuations . . . . .	77
7.16	Phase of unsteady heat release due to equivalence ratio fluctuations . . . . .	77
7.17	Influence of amount of premix gas nozzles on reflection factor magnitude . . . . .	77
7.18	Influence of amount of premix gas nozzles on reflection factor phase . . . . .	77
7.19	Influence of amount of premix gas nozzles on stability . . . . .	78
7.20	Pressure spectrum between 80 - 280 Hz for different nozzle configurations . . . . .	78
7.21	Nozzle configuration influence on pressure amplitude in FB2 . . . . .	78
7.22	Nozzle configuration influence on pressure amplitude in FB5 . . . . .	79
7.23	Nozzle configuration influence on pressure amplitude in FB7 . . . . .	79
7.24	Influence of cylindrical burner outlet ring on flow field [22] . . . . .	80
7.25	Influence of cylindrical burner outlet ring on burner system impedance . . . . .	81
7.26	Magnitude of unsteady heat release due to equivalence ratio fluctuations . . . . .	81
7.27	Phase of unsteady heat release due to equivalence ratio fluctuations . . . . .	81
7.28	Magnitude of unsteady heat release due to velocity fluctuations at the burner mouth . . . . .	82
7.29	Phase of unsteady heat release due to velocity fluctuations at the burner mouth . . . . .	82
7.30	Reflection factor magnitude for the CBO burner configuration with different flame lengths . . . . .	82
7.31	Reflection factor phase for the CBO burner configuration with different flame lengths . . . . .	82
7.32	Stability plot for the CBO burner configuration with different flame lengths . . . . .	83
7.33	Pressure spectrum between 80 - 280 Hz for the CBO burner configuration . . . . .	83
7.34	Pressure spectrum at FB2 for the CBO burner configuration . . . . .	84
7.35	Pressure spectrum at FB5 for the CBO burner configuration . . . . .	84
7.36	Impedance of the gas supply for different configurations . . . . .	85
7.37	Magnitude of unsteady heat release due to equivalence ratio fluctuations . . . . .	86
7.38	Phase of unsteady heat release due to equivalence ratio fluctuations . . . . .	86
7.39	: Magnitude of unsteady heat release due to velocity fluctuations at the burner mouth . . . . .	86
7.40	Phase of unsteady heat release due to velocity fluctuations at the burner mouth . . . . .	86
7.41	Fuel composition influence on reflection factor magnitude . . . . .	87
7.42	Fuel composition influence on reflection factor phase . . . . .	87
7.43	Stability plot for low-calorific fuel composition . . . . .	87
7.44	Magnitude of unsteady heat release due to equivalence ratio fluctuations . . . . .	89
7.45	Phase of unsteady heat release due to equivalence ratio fluctuations . . . . .	89
7.46	Magnitude of unsteady heat release due to velocity fluctuations at the burner mouth . . . . .	90
7.47	Phase of unsteady heat release due to velocity fluctuations at the burner mouth . . . . .	90
7.48	Hydrogen addition influence on reflection factor magnitude . . . . .	90
7.49	Hydrogen addition influence on reflection factor phase . . . . .	90
7.50	Stability plot for hydrogen addition . . . . .	91
B.1	Change in acoustic pressure amplitude as a result of gas preheating temperature reduction - FB2	109
B.2	Change in acoustic pressure amplitude as a result of gas preheating temperature reduction - FB3	109
B.3	Change in acoustic pressure amplitude as a result of gas preheating temperature reduction - FB5	110
B.4	Change in acoustic pressure amplitude as a result of gas preheating temperature reduction - FB6	110
B.5	Change in acoustic pressure amplitude as a result of gas preheating temperature reduction - FB7	110
C.1	Reflection factor magnitude for different Helmholtz resonator volumes . . . . .	111
C.2	Reflection factor phase for different Helmholtz resonator volumes . . . . .	111
C.3	System stability for different Helmholtz resonator volumes . . . . .	112
C.4	Reflection factor magnitude for different fuel piping lengths . . . . .	112
C.5	Reflection factor phase for different fuel piping lengths . . . . .	112
C.6	System stability for different fuel piping lengths . . . . .	112
D.1	Acoustic network model clarinet . . . . .	113
D.2	Eigenfrequencies of the clarinet . . . . .	114

---

D.3	Pressure spectrum at node 3 and 5 of the clarinet . . . . .	115
D.5	Normalized pressure fluctuations evaluated at each node for the three found eigenfrequencies .	116
D.6	Pressure spectrum at node 3 for varying source strength . . . . .	117

# List of Tables

3.1	Rijke tube parameters from Heckl [16] . . . . .	36
3.2	Fundamental frequency and growth rate of the Rijke tube from different papers . . . . .	37
3.3	Resonant modes from Dowling & Stow [12] compared with modelled resonant modes, for $k = 0$ . . . . .	39
3.4	Flame resonant modes from Dowling & Stow [12] compared with modelled flame resonant resonant modes . . . . .	40
4.1	Monitored frequency bands by stability margin controller . . . . .	50
5.1	Transfer matrix element representation . . . . .	54
6.1	Frequency areas of interest of SGT5 combustion system . . . . .	61
6.2	Base-case values for model input at base load . . . . .	68
7.1	Basic operating conditions for analysis of influence of gas preheating temperature . . . . .	70
7.2	Frequency areas and expected responses for a gas preheating temperature decrease from 200C to 100C . . . . .	70
7.3	Basic operating conditions for analysis of influence of premix nozzles . . . . .	75
7.4	Basic operating conditions for analysis of influence of CBO . . . . .	80
7.5	Basic operating conditions for analysis of influence of low calorific fuel influence . . . . .	85
7.6	Basic operating conditions for analysis of influence of hydrogen addition . . . . .	89
D.1	First resonance/eigenfrequencies for the clarinet . . . . .	113



# Introduction

## 1.1. Energy generation in gas turbines

The demand for energy is rising on a global scale. The percentage of electricity generated by renewable energy is increasing, but most electricity is still generated using other sources, with a significant part coming from natural gas. Figure 1.1 shows the electricity production for the Netherlands from 2000 onwards. The problem with renewable energy production, like wind and solar energy, is that it is not as reliable as one is dependent on wind and solar power. Natural gas is used in combined cycle power plants, which provide a reliable way for energy production. Combined cycle power plants are also known to be flexible in their energy production, as they can scale up or down relatively fast if the demand for energy fluctuates.

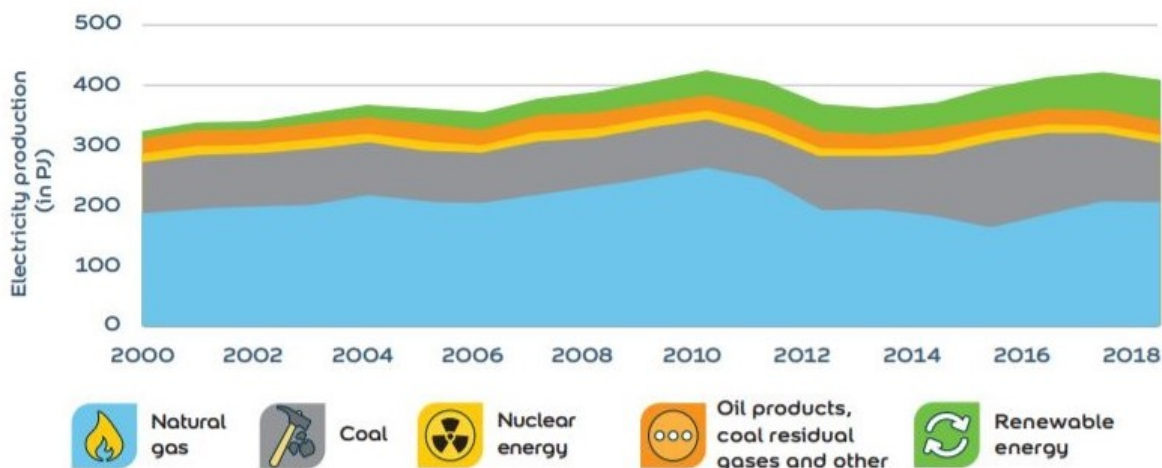


Figure 1.1: Electricity production in the Netherlands from 2000 onwards. Retrieved from: <https://www.energiein nederland.nl/infographic/>

### 1.1.1. Combined cycle power plants

Combined cycle power plants, see figure 1.2, are a combination of a gas turbine (2) and a steam turbine (4), where fuel is combusted in the gas turbine and the heat of these combustion gases is used to generate steam for the steam turbine. The combustion in the gas turbine happens in the combustion chamber (1), which is located between the compressor and the turbine. In this combustion chamber the chemical energy which is present in the fuel will be converted into thermal energy. The compressor feeds compressed air into the combustion chamber, after which the air is mixed with fuel. This mixture reacts and is combusted, after which the hot combustion gases are delivered into the turbine, which converts the thermal energy to mechanical energy, which drives the shaft of the generator. This specific gas turbine has an efficiency between 35% to 40%.

The combustion gases are still around 580-590°C when they leave the turbine. The heat in these combustion gases is recovered and is used to generate steam (3), the energy in the steam is turned into mechanical energy by the steam turbine (4). This takes the efficiency of the combined cycle system upwards of 58%.

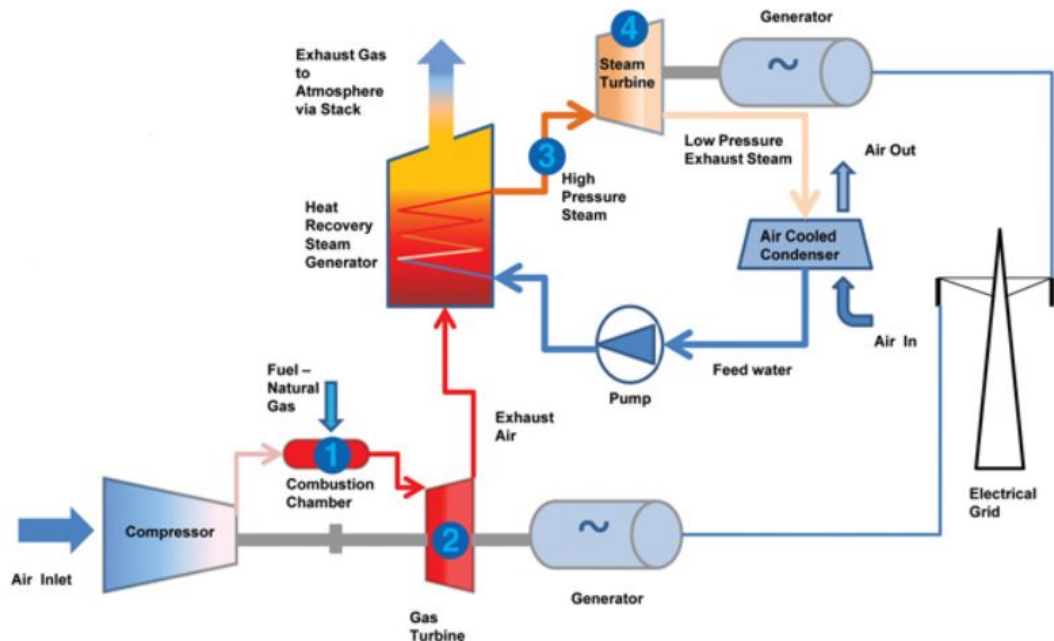


Figure 1.2: Schematic representation of combined cycle gas turbine system; retrieved from: [http://www.meaford-energy.com/images/CCGT-Schematic\\_1.jpg](http://www.meaford-energy.com/images/CCGT-Schematic_1.jpg)

Vattenfall operates two combined cycle power plants of the same type, equipped with the Siemens SGT5-4000F gas turbine. These power plants will be referred to as Hemweg 9 (HW09), which is located in Amsterdam, and Diemen 34 (DM34), which is located in Diemen. Single cycle production, with just the gas turbine, can reach a power output of 300 MW, but as these are both operated in combined cycle, which means there is a steam turbine coupled with the gas turbine, they both can generate up to 420 MW. These units are nearly identical, but are operated on a different type of natural gas. HW09 is operated on high-calorific natural gas, while DM34 is operated on low-calorific natural gas (Groninger-gas).



Figure 1.3: Vattenfalls combined cycle power plant in Amsterdam - HW09



Figure 1.4: Vattenfalls combined cycle power plant in Diemen - DM34

### 1.1.2. Combustion instabilities in combined cycle power plants

With increasing discussion and legislation around emissions, gas turbines have evolved to limit their emissions, especially  $\text{NO}_x$  emissions. This is done by operating the gas turbine with lean premixed combustion, which ensures that the combustion temperature remains low, which heavily reduces  $\text{NO}_x$  emissions, see figure (1.5). The system that is used to reduce the flame temperature is called Dry Low  $\text{NO}_x$  (DLN). This system reduces the flame temperature without the addition of wet components, such as water, for cooling of the combustion system. With a DLN system, the temperature is reduced by an excess of air. The combustion system makes use of a premixed fuel, which means that air and gas are mixed upstream of the burner outlet. The excess of air thus also reduces the equivalence ratio. The problem with this operating procedure is that the combustion system becomes increasingly sensitive to combustion instabilities. These instabilities can result in a temporary reduction of power or even worse, damage to the combustion chamber or burner, see figure 1.6.

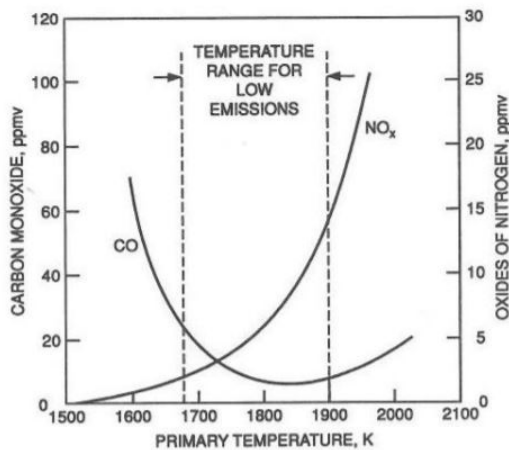


Figure 1.5: CO and  $\text{NO}_x$  emissions versus combustion temperature [36]



Figure 1.6: Damaged cover on a gas turbine burner due to excessive combustion dynamics [24]

## 1.2. Problem statement

The premixed combustion system makes the combustion of modern gas turbines susceptible to combustion instabilities. These instabilities arise due to a coupling between the acoustics of the combustion system and the heat release at the flame front. At low equivalence ratio the flame speed is heavily changed by a small perturbation in the equivalence ratio, see figure 1.7. When the flame speed is altered, the heat release at the flame front will be altered as well and thus resulting in unsteady heat release. The unsteady heat release results in an unsteady volume flux downstream of the flame front and thus acoustic pressure waves will be created. When these pressure waves reflect in the combustion chamber and influence the flame again, a feedback cycle between the acoustics of the system and the unsteady heat release is established. This is the driving force for combustion instabilities, the effects and feedback loops that can influence the heat release are shown in figure 1.8. The feedback loop between the acoustic system and the unsteady heat release can amplify the acoustic pressure in the system to infinity if the system is linear, but the amplitude will be limited by non-linear effects. This can still result in damage to the combustion system or a required reduction in gas turbine load to stabilize the system.

To limit the occurrence of combustion instabilities several measures have been taken, to both the operational control system and the physical system. These measures include the reduction of fuel preheating temperature and/or the reduction of turbine outlet temperature, as well as reducing the amount of gas nozzles. Some of those parameters have a direct and negative effect on the efficiency of the combined cycle and thus result in a loss of potential power output. Stable operation at high gas temperature and high turbine outlet temperature results in the highest efficiency and thus highest power output, which is desired. Modelling the combustion system correctly can allow for optimization of the combustion system and operational control system, which can result in improved stability and thus improved efficiency of the combined cycle power plant. It can also function as a predictive tool to analyze the effects of different fuel mixtures on combustion stability.

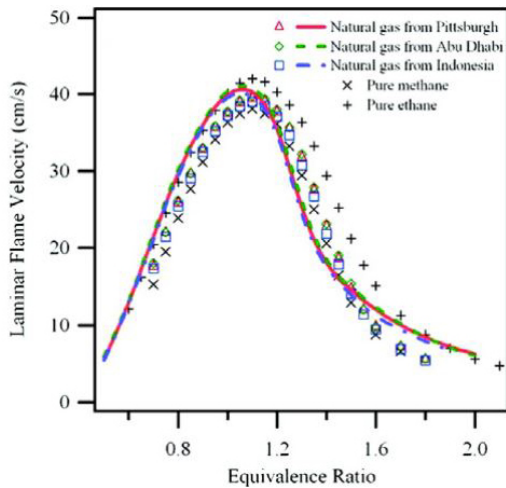


Figure 1.7: Laminar flame speed vs equivalence ratio at STP; Points, experiments; Lines, modeling by Dirrenberger [9]

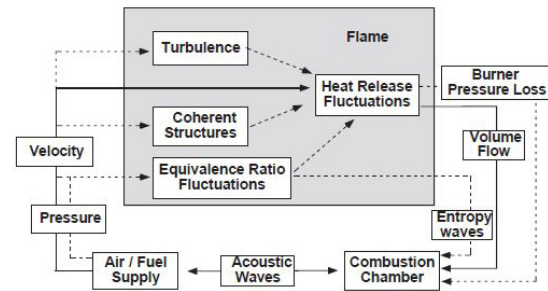


Figure 1.8: Acoustic coupling with heat release [33]

### 1.3. Research objective

Using the problem statement, the main goal of this thesis is defined as:

*What is the impact of operating conditions on thermo-acoustic combustion instabilities in Vattenfalls SGT5-4000F combined cycle gas turbine?*

#### 1.3.1. Research questions

- What is the dominant mechanism to drive combustion instabilities?
- How can the (thermo-)acoustic system be modelled?
- What relations exist between physical or operational parameters and combustion instabilities in the SGT5-4000F?
- What is the impact of the fuel composition upon combustion instability?

#### 1.3.2. Scope

This research will focus on the combustion dynamics in the Siemens SGT5-4000F gas turbine at base load operation. This system will be modelled from air inlet into the burner up to and including combustion in the combustion chamber. The boundaries of the system are thus downstream of the compressor outlet and upstream of the turbine inlet.

#### Premix burner system

As input in the combustion chamber, only the premix burner system will be taken into account. The pilot system provides a certain amount of stability at base load, but is mainly used during start-up and as intervention measure to re-stabilize an unstable system. As the scope of this research is to determine what parameters influence the instability, the premix burner system itself should suffice.

#### Time independent results

The results will be time-independent. The increase/decrease of the stability of the system will be analyzed. Assumed will be that an increase in stability will result in damped acoustics as time progresses. For a decrease in stability it will be assumed that the acoustics will be amplified as time progresses.

#### Frequency range

Stability will be analysed for frequencies up to 300 Hz, this is the range of frequencies that provide most issues in the analysed gas turbine.

## 1.4. Thesis outline

Chapter 2 will introduce background information on acoustics, one-dimensional waves, combustion, combustion instabilities, the transfer matrix method and the flame transfer function. In chapter 3 the transfer matrix method will be validated using thermo-acoustic systems derived from literature. The SGT5-4000F gas turbine and the hybrid burners, as well as some of the measures that have been taken to improve the stability of the investigated combustion system will be introduced in chapter 4. In chapter 5 the cold flow model for the burner geometry will be set-up, where in chapter 6 the flame behaviour will be included to transform the model into a thermo-acoustic model. Chapter 6 will also feature a sensitivity analysis of the flame behaviour to determine the base-case parameters, for operation at base load, that provide the expected flame behaviour. Known relationships between combustion parameters and the combustion dynamics will be tested in chapter 7 to validate the thermo-acoustic model. After the model is validated, the influence of a cylindrical burner ring and different fuel compositions will be researched. The final chapter of this thesis will talk about the conclusion of the research and recommendations for further research.

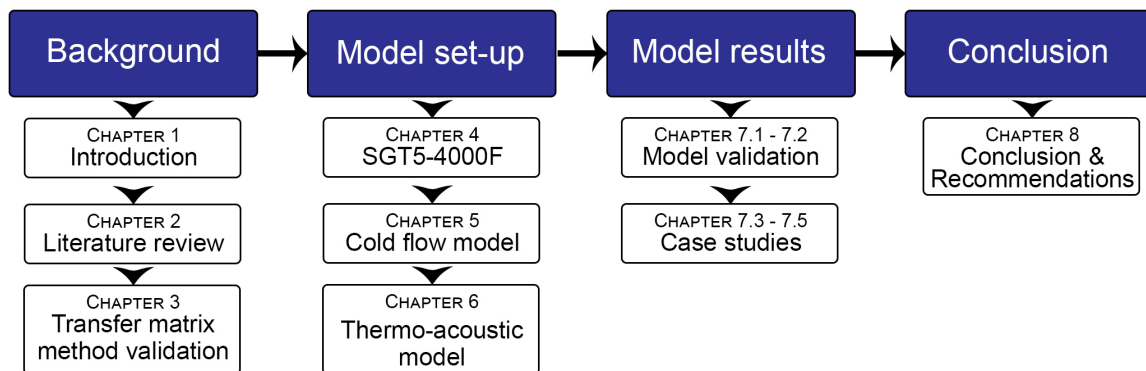


Figure 1.9: Schematic overview of thesis outline



# 2

## Literature review

In this chapter background information on acoustics, one-dimensional waves, combustion, combustion instabilities, the transfer matrix method and the flame transfer function will be introduced. This will provide the tools to comprehend the nature of combustion instabilities and how they occur, as well as understanding the way they can be modelled. In chapter 3 this information will be used to model a thermo-acoustic system with an active heat source and a thermo-acoustic system with an active flame.

### 2.1. Acoustics

#### 2.1.1. Introduction

When one talks about acoustics, they talk about the propagation and generation of sound [21]. Sound is defined as a pressure perturbation, referred to as  $p'$ , which propagates as a wave with the speed of sound [38]. Acoustics are governed by three equations: the conservation of mass (2.1), the conservation of momentum (2.2) and an energy equation (2.3) [38]. For the energy equation an equation in terms of enthalpy is used, which is easier to describe combustion processes with [21].

$$\frac{\partial \rho}{\partial t} + \nabla \cdot (\rho \underline{u}) = 0 \quad (2.1)$$

$$\frac{\partial \rho \underline{u}}{\partial t} + \nabla \cdot (\rho \underline{u} \underline{u}) = -\nabla p + \nabla \cdot \underline{\underline{\tau}} + \underline{f} \quad (2.2)$$

$$\rho \frac{Dh}{Dt} = -(\nabla \cdot \underline{D}_q) - (\underline{\underline{\tau}} : \nabla \underline{u}) + \frac{Dp}{Dt} \quad (2.3)$$

#### 2.1.2. Analogy of Lighthill

These equations can be used to get to the acoustic wave equation, which is done by following the analogy of Lighthill [28] [29]. First the time derivative is taken of the conservation of mass equation (2.1).

$$\frac{\partial^2 \rho}{\partial t^2} + \frac{\partial}{\partial t} (\nabla \cdot (\rho \underline{u})) = 0 \quad (2.4)$$

Then the divergence of the momentum equation (2.2) is taken:

$$\nabla \cdot \left( \frac{\partial \rho \underline{u}}{\partial t} \right) + \nabla \cdot (\nabla \cdot (\rho \underline{u} \underline{u})) = -\nabla^2 p + \nabla^2 \cdot \underline{\underline{\tau}} + \nabla \cdot \underline{f} \quad (2.5)$$

Equation (2.4) is subtracted from (2.5), which removes the first term in (2.5) and adds the (negative) first term of (2.4):

$$-\frac{\partial^2 \rho}{\partial t^2} + \nabla \cdot (\nabla \cdot (\rho \underline{u} \underline{u})) = -\nabla^2 p + \nabla^2 \cdot \underline{\underline{\tau}} + \nabla \cdot \underline{f} \quad (2.6)$$

The Lighthill analogy rewrites this equation to get a wave equation in terms of an acoustic density fluctuation,  $\rho'$ . The acoustic fluctuations are defined as,  $\rho' = \rho - \rho_0$  and  $p' = p - p_0$ . For this thesis, a wave equation in

terms of acoustic pressure fluctuation,  $p'$ , is derived. To rewrite this in terms of  $p'$  a relationship between density and pressure is used (2.7), which is valid in case of an isentropic process. Writing this in terms of  $p'$  also changes the structure of the source term, which is advised and more convenient for cases where unsteady heat release occurs [38]. To get to the wave equation, first equation (2.6) is rewritten and assumed is that  $\nabla \cdot \underline{f} = 0$ . This assumption is valid as the only external force will be gravity, which is uniform. Then the term  $\frac{1}{c_0^2} \frac{\partial^2 p'}{\partial t^2}$  is subtracted which results in:

$$p' = c_0^2 \rho' \quad (2.7)$$

$$\frac{1}{c_0^2} \frac{\partial^2 p'}{\partial t^2} - \nabla^2 p' = \nabla \cdot (\nabla \cdot (\rho \underline{u} \underline{u} - \underline{\tau})) + \frac{\partial^2}{\partial t^2} \left( \frac{p'}{c_0^2} - \rho' \right) \quad (2.8)$$

This concludes the analogy of Lighthill. The terms on the left hand side of (2.8) describe the propagation of the pressure fluctuation with the speed of sound  $c_0$ . Both terms on the right hand side of the equation are defined as source terms.  $\nabla \cdot (\nabla \cdot (\rho \underline{u} \underline{u} - \underline{\tau}))$  is called the flow noise term, but will be neglected as an order of magnitude analysis by Klein [21] shows that the other term is most important. Besides that, due to the high Reynolds number of the flow, the viscous stress tensor  $\underline{\tau}$  is negligible as viscous forces will have a small contribution.  $\frac{\partial^2}{\partial t^2} \left( \frac{p'}{c_0^2} - \rho' \right)$  is the other term and is called the thermo-acoustic source term.  $\left( \frac{p'}{c_0^2} - \rho' \right)$  is equal to the negative of the excess density,  $\rho_e$ . This thermo-acoustic source term is mainly driven by the heat release,  $q$ , in the flame. The term on the RHS of equation (2.9) can be rewritten in terms of a fluctuating heat release rate as seen in equation (2.10) [19], this derivation will be shown in Appendix A.

$$\frac{1}{c_0^2} \frac{\partial^2 p'}{\partial t^2} - \nabla^2 p' = \frac{\partial^2}{\partial t^2} \left( \frac{p'}{c_0^2} - \rho' \right) \quad (2.9)$$

$$\frac{1}{c_0^2} \frac{\partial^2 p'}{\partial t^2} - \nabla^2 p' = \frac{\partial}{\partial t} \left[ \frac{\gamma - 1}{c_0^2} q' \right] \quad (2.10)$$

### 2.1.3. The flame as a source of sound

The source of sound present in the combustion system is a result of the fluctuating heat release rate at the flame, as mentioned in the previous paragraph. This source can either be a passive or an active source, which influences the stability of the system [21].

#### Passive source of sound

In this case the passive source of sound is defined as the source in the case that the heat release fluctuation is not influenced by the acoustic pressure fluctuations in the combustion system. These fluctuations in heat release are caused by e.g. random turbulent fluctuations, vortex shedding. These pressure fluctuations can generate a lot of sound, but since there is no feedback-loop between the acoustic pressure and the combustion dynamics, the amplitude does not grow in time and the system remains stable.

#### Active source of sound (amplifier)

The active source of sound is defined as the source in the case that the heat release fluctuation is influenced by the acoustic pressure fluctuation in the combustion system, in this case the flame acts as an amplifier of sound. A fluctuation in heat release will generate an acoustic pressure fluctuation, this pressure fluctuation can be reflected of the boundaries in the combustion chamber, either upstream or downstream of the flame. This acoustic pressure wave can for example influence the fuel mass flow: a high amplitude acoustic pressure wave travelling towards the mixing chamber in the burner, will very shortly hinder the fuel flow outlet, which changes the fuel mixture that is convected towards the flame. This change in mixture will result in a change in heat release. If this occurs in a feedback loop, the fluctuations might be increasing in time and will grow to infinity in a linear acoustic system. The amplitude will be limited by non-linear effects. The high amplitudes can result in severe damage to the combustion system. This is the feedbackloop that was introduced in chapter 1, figure 1.8. The interactions and requirements that lead to combustion instabilities are further explained in chapter 2.4.

The passive source of sound will be used in the acoustic example in Appendix D, for the examples in chapter 3 the flame as an active source, and thus amplifier, of sound will be used.

## 2.2. Acoustic wave solution

### 2.2.1. Homogeneous wave equation

To provide solutions for the acoustic wave equations, a look will be taken at the homogeneous wave equation in a fluid at rest. No source term is present in this wave equation. The derivation of this wave equation follows the Lighthill analogy again and results in the following wave equation in terms of  $p'$ . The homogeneous wave equation is equal to the left-hand side of (2.10).

$$\frac{\partial^2 p'}{\partial t^2} - \nabla^2 p' = 0 \quad (2.11)$$

$$\frac{1}{c_0^2} \frac{\partial^2 p'}{\partial t^2} - \nabla^2 p' = 0 \quad (2.12)$$

Substituting the constitutive equation (2.7) into equation (2.11) results in the homogeneous wave equation (2.12) as a function of acoustic pressure in a fluid at rest [38].

### 2.2.2. Convective homogeneous wave equation

The wave equation mentioned in the previous paragraph does not take into account mean flow, which should be taken into account in the combustion system. At the flame, due to high temperatures, the Mach number will be small and thus mean flow will have little effect on the acoustics. At lower temperature regions, for example in the burner system, the mean flow can have an effect on the acoustics. The wave equation is changed to take into account that the medium is flowing at a constant speed, this will be called the convective homogeneous wave equation. This will take the convection effects into account for the sound propagation. This leads to the following wave equation (2.14) [38], where  $\frac{D}{Dt}$  (2.13) is also called the material derivative which describes the time rate of change of a parameter of interest,  $p'$  in this case, as it flows along a pathline with a velocity field  $\underline{u}$ .

$$\frac{Dp'}{Dt} = \frac{\partial p'}{\partial t} + \underline{u} \nabla p' \quad (2.13)$$

$$\frac{1}{c_0^2} \frac{D^2 p'}{Dt^2} - \nabla^2 p' = 0 \quad (2.14)$$

### 2.2.3. One dimensional wave solutions

These wave equations can be solved in terms of an acoustic pressure wave or an acoustic velocity wave. First the solutions for the homogeneous wave equation (2.15) will be given [38], second will be the solutions for the convective homogeneous wave equation (2.16) [21].

$$p' = f(x - c_0 t) + g(x + c_0 t) \quad (2.15a)$$

$$u' = \frac{1}{\rho_0 c_0} [f(x - c_0 t) - g(x + c_0 t)] \quad (2.15b)$$

$$p' = f(x - (c_0 + \bar{u}) t) + g(x + (c_0 - \bar{u}) t) \quad (2.16a)$$

$$u' = \frac{1}{\rho_0 c_0} [f(x - (c_0 + \bar{u}) t) - g(x + (c_0 - \bar{u}) t)] \quad (2.16b)$$

In these equations  $f$  is defined as a right or downstream travelling plane wave, where as  $g$  is defined as a left or upstream travelling plane wave, see figure (2.1). In the case of the convective homogeneous wave equation, the travelling wave is influenced by the time-averaged mean flow velocity  $\bar{u}$ . As the mean flow will be taken into account throughout this thesis, the convective form of the wave equation will be used and referred through from this point forward.

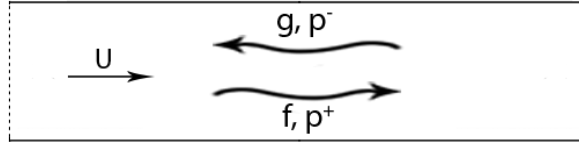


Figure 2.1: Wave propagation in simple cylindrical duct

### 2.2.4. Harmonic wave solutions

The acoustic system description will be linear, so the solutions to the wave equation can be written as harmonic waves [21].

$$p'_i = p_i^+ e^{(i\omega t - ik^+ x)} + p_i^- e^{(i\omega t + ik^- x)} \quad (2.17a)$$

$$u'_i = \frac{1}{\rho_0 c_0} (p_i^+ e^{(i\omega t - ik^+ x)} - p_i^- e^{(i\omega t + ik^- x)}) \quad (2.17b)$$

$p^+$  and  $p^-$  are the complex wave amplitudes travelling in respectively the downstream and upstream direction, see figure (2.1).  $\omega$  is the angular frequency which is equal to  $2\pi f$  with  $f$  in this case being the frequency in Hz.  $k^+$  and  $k^-$  are the wave numbers:

$$k^\pm = \frac{\omega}{c_0 \pm \bar{u}} \quad (2.18)$$

These solutions can also be made time independent, which results in the following expression:

$$p' = p^+ e^{-ik^+ x} + p^- e^{ik^- x} \quad (2.19)$$

The equations (2.17) will be used in the acoustic transfer matrix model to linearise the conservation equations. They can be used to write the mass, momentum and energy equations over geometries and relate the acoustic fluctuations from input to output.

## 2.3. Combustion

### 2.3.1. Introduction

The combustion in the gas turbine happens in the combustion chamber, which is located between the compressor and the turbine. In this combustion chamber the chemical energy which is present in the fuel will be converted into thermal energy.

Below a side-view of the Siemens SGT5-4000F gas turbine is presented. Different components of the gas turbine are denoted. The ambient air flows through the air intake (1), where it is supplied to the compressor (2). The fuel and air will be combusted in the combustion chamber denoted by 3, where the air is supplied through the plenum denoted by 4. The turbine section (5) will extract work from the hot combustion gases, which will flow out through the exhaust section (6) towards the heat recovery steam generator.

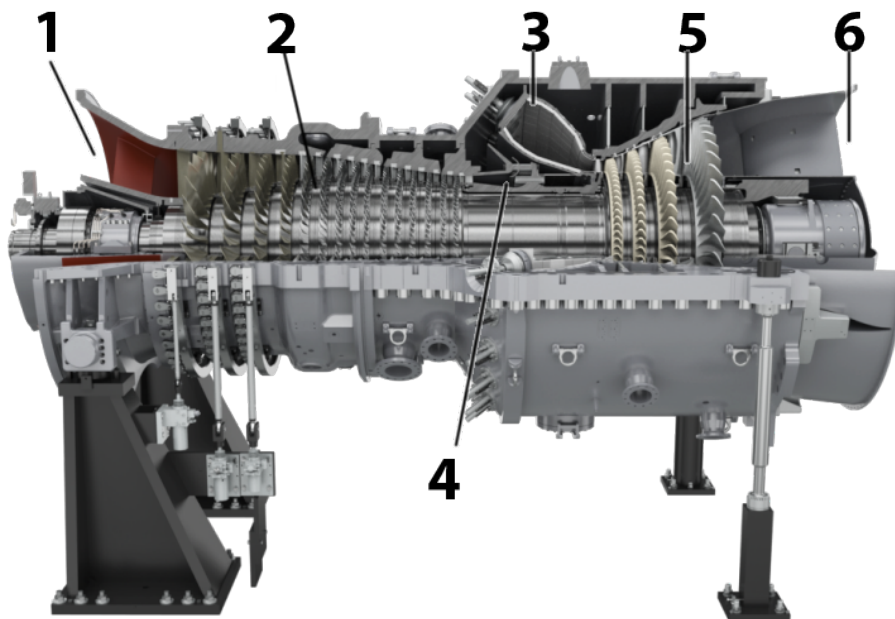


Figure 2.2: Siemens SGT5-4000F Gas turbine; retrieved from:  
<https://new.siemens.com/cn/en/products/energy/power-generation/gas-turbines/sgt5-4000f.html>

### 2.3.2. Combustion process

In figure 2.3 a schematic overview of the Brayton cycle is shown. Air flows into the compressor and flows out of the compressor at higher pressure, this is step 1-2. This compressed air is mixed with fuel, after which it is combusted in the combustion chamber which adds heat to the gases and increases the volume of the gases, this is step 2-3. The combustion gases flow into the turbine at high pressure, where the gasses are expanded. The turbine extracts work from the gases which drive the generator axis, which generates the electricity. The expanded but still hot exhaust gases are not re-used in the depicted cycle. In the combined cycle process however, the hot air will be used to drive the steam generation of the steam cycle, increasing efficiency of the total cycle.

The cycle depicted in figure 2.3 is a so called ideal Brayton cycle. It assumes that compression and expansion happens at isentropic conditions, while heat addition and rejection happen at isobaric conditions. In an actual combustion cycle there will be entropy losses and pressure losses over those steps, which reduces efficiency.

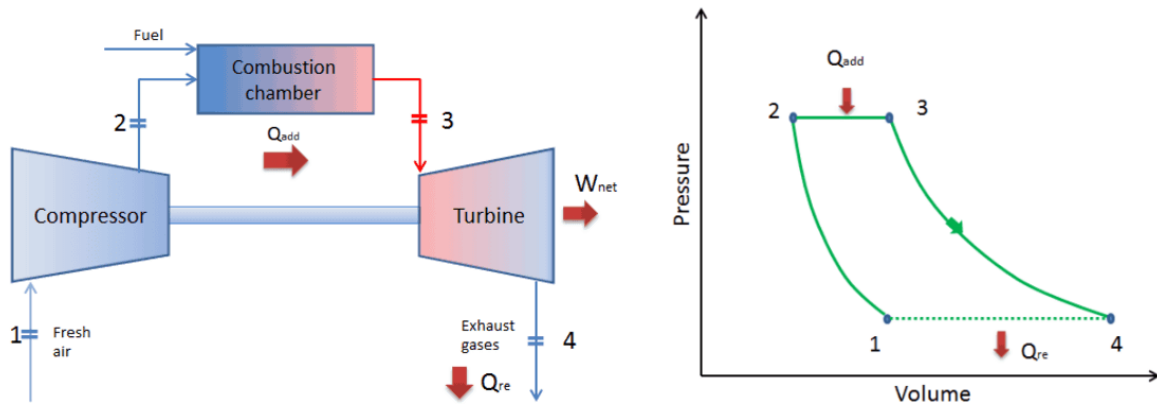
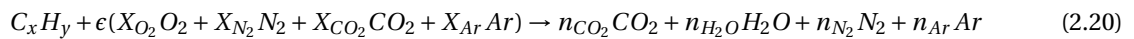


Figure 2.3: Ideal Brayton cycle; retrieved from:  
<https://www.nuclear-power.net/nuclear-engineering/thermodynamics/thermodynamic-cycles/>

### 2.3.3. Equivalence ratio

For complete combustion of the fuel, a certain amount of oxygen is required to convert the (hydrocarbon) fuel to carbon dioxide and water vapor [44]. If the supplied air is the exact amount that is required for complete combustion, this is called the stoichiometric ratio. This ratio can be calculated by solving the equation for a complete ideal combustion [44] for a hydrocarbon fuel of  $x$  atoms of C and  $y$  atoms of H:



With  $X_i$  mole fraction of species  $i$ ,  $n_i$  number of moles of species  $i$  per mole of fuel and  $\epsilon = \frac{x+y/4}{X_{O_2}}$ . If one fills in the hydrocarbon fuel composition and an estimate for the composition of air equation (2.20) can be solved [44]. This results in a value for  $\epsilon$ , which is the moles of air required per mole of fuel. From that the stoichiometric fuel-to-air ratio follows:

$$FAR_{st} = \frac{1}{\epsilon} \frac{M_{C_xH_y}}{M_a} = \frac{X_{O_2}}{x+y/4} \frac{M_{C_xH_y}}{M_a} \quad (2.21)$$

$$\phi = \frac{\dot{m}_f}{\dot{m}_a} \frac{1}{FAR_{st}} \quad (2.22)$$

With  $\dot{m}_f$  the supplied amount of fuel,  $\dot{m}_a$  the supplied amount of air and  $FAR_{st}$  the stoichiometric fuel-to-air ratio [44]. The equivalence ratio will be equal to 1 in case the fuel-air mixture is supplied in the stoichiometric ratio. When an excess amount of air is present the equivalence ratio becomes smaller than 1, which is the lean mixture. When an excess amount of fuel is present the equivalence ratio becomes greater than 1, which is a rich mixture. In the latter case, combustion will not be complete as not all fuel will be able to be combusted.

### 2.3.4. Combustor types

There are two standard types of combustor systems for land based gas turbines, which will be briefly introduced and described [44].

#### Can-type combustor

The can-type combustor is also called the tubular combustor, this is the most standard type of combustor. The air which leaves the compressor is split into separate streams, which are all directed to a different combustion chamber. All these chambers are fed fuel independently from a common fuel supply system. After combustion the gases were collected again to be fed into a single flow towards the turbine. The separate combustion can or combustion chambers are interconnected, this allows operation at equal pressure and for the combustion to propagate through at engine start-up.

#### Annular combustor

The annular combustor consists of a single combustion chamber fitted with multiple burners. This allows combustion to propagate in the circumferential direction through the combustion chamber during start-up.

The amount of required cooling air required is reduced due to a decrease in liner area as opposed to the can-type system. Another advantage is a low-pressure loss over the combustion chamber. It is however difficult to match fuel and air flows throughout the system, as it is hard to achieve a uniform distribution of fuel. The Vattenfall operated gas turbines are of the annular type, developed by Siemens type SGT5-4000E.

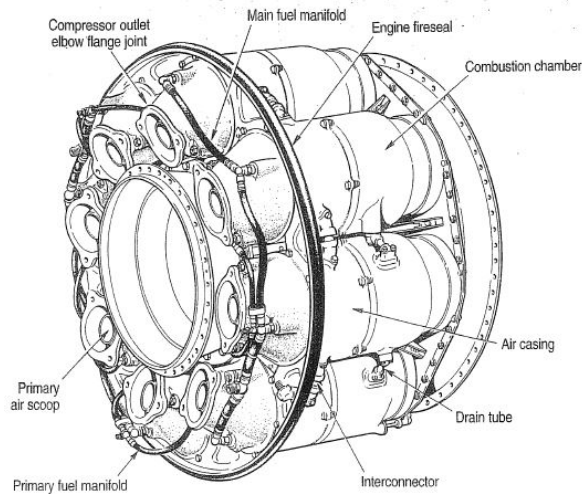


Figure 2.4: Rolls-Royce can-type combustor [7]

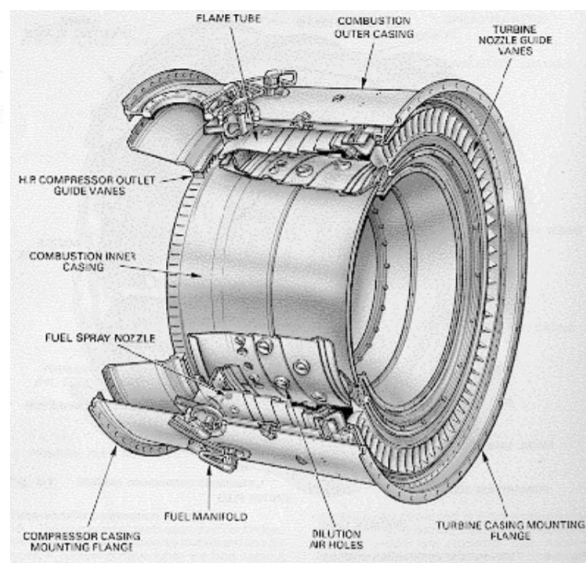


Figure 2.5: Annular combustor [2]

### 2.3.5. Lean premixed combustion

To limit  $\text{NO}_x$  emission, gas turbines now-a-days are fitted with a lean premixed combustion system.  $\text{NO}_x$  emission is greatly reduced by keeping the flame temperature low, this is mostly done by supplying an excess of air to the fuel mixture. This excess of air, and thus lean combustion, makes the combustion system more susceptible to combustion instabilities[11]. In the case of lean premixed combustion, a small perturbation of air velocity supplied to the flame can lead to large variations in the instantaneous rate of heat release. This was shown in figure 1.7, where at low equivalence ratio a small perturbation in equivalence ratio would result in a large increase in flame speed. As has been shown with the analogy of Lighthill (2.8), the instantaneous rate of heat release is the driving force for acoustic pressure disturbances. This heat release can also be influenced by for example vortex shedding, this can result in large scale irregular vibrations of the flame [25]. The conditions that are required for lean premixed combustion to turn into unstable combustion will be discussed in the next chapter.

### 2.3.6. Gas composition

The composition of the gas that is supplied to the gas turbine has a big influence on the combustion behaviour of the mixture. The range of natural gas that is supplied to the gas turbine has become increasingly more broad. The quality of a gas fuel can be indicated with the so called Wobbe Index (WI). The Wobbe Index is a measure of the energy input into the combustion system, see equation 2.23. It is calculated using the higher heating value (HHV) or the lower heating value (LHV), divided by the relative density of the natural gas. Two fuels with different gas compositions, but equal WI at given combustor conditions and control valve positions will still have the same energy input into the combustion system [1]. The SGT5-4000F gas turbine can operate successfully in a range of  $\pm 5\%$  WI, if the variation of WI is outside this range, the gas turbine control system needs to be re-tuned to allow for proper operation.

$$WI = \frac{HHV}{\sqrt{RD_{gas}}} \quad (2.23)$$

### Flame speed

Eventhough fuels with different compositions can have an equal Wobbe Index, there are other aspects that change with fuel composition. An important factor for combustion stability is flame speed, where the flame speed as a function of equivalence ratio is also very important. An increase in flame speed results in a decrease of flame length [27]. This indicates that a change in fuel composition can result in a changed flame length, which influences the convective time-delay in the combustion system. In the following chapter more information will be provided on the influence of time-delays on system stability, but a changed time-delay can take a stable combustion system towards instability. The influence of fuel composition on flame speed can be very large, in figures 2.6 and 2.7 the flame speeds of two different methane and hydrogen fuel blends are shown [30]. This is an extreme case, as hydrogen is known to have a high flame speed, but the change in laminar flame speed is very significant. Siemens has said that without physical changes to the gas turbine, it is possible to operate on a natural gas mixture with 30% volumetric hydrogen addition [31]. In the case of hydrogen addition, the slope of the flame speed as a function of equivalence ratio also significantly increases at low equivalence ratio. This results in a more severe response to equivalence ratio fluctuations, as the subsequent flame speed fluctuation will be larger.

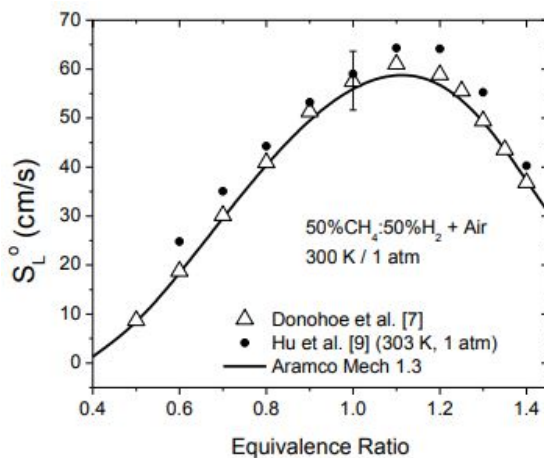


Figure 2.6: Laminar flame speed versus equivalence ratio; 50%  $\text{CH}_4$ :50% $\text{H}_2$  fuel mixture [30]

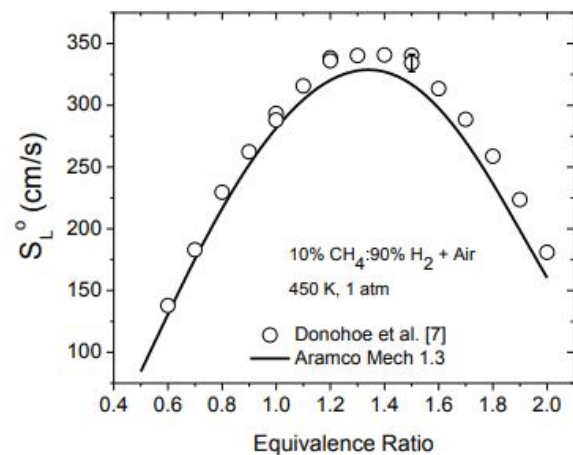


Figure 2.7: Laminar flame speed versus equivalence ratio; 10%  $\text{CH}_4$ :90% $\text{H}_2$  fuel mixture [30]



a combustion chamber, the sound may be reflected from the boundaries of the combustion chamber. These reflected waves can then interact with the combustion process, which may be sensitive to flow field variations. If the phase between the acoustic pressure wave and the heat release fluctuation is right, a self-excited and self-amplified combustion instability will occur. Something that can start of as a very small heat release fluctuation can quickly be amplified to severe pressure fluctuations.

### 2.4.3. Rayleigh's Instability Criterion

The coupling of the fluctuating heat release and pressure waves has been observed a long time ago by Rayleigh. His stability criterion (2.25) states that, if, the fluctuating heat release and pressure act in phase with one another and they amplify each other they can create instabilities. It is very important to note that while it is true that this can cause instabilities, it does not necessarily mean that if they act in phase, there in fact will be instabilities [33]. As it is still possible that in other places in the combustion system energy is lost, if this damping exceeds the amplification by the feedback process, instabilities will still not occur.

$$\int p' \dot{Q}' dt > \zeta \quad (2.25)$$

In this criterion  $p'$  are the fluctuations of pressure,  $\dot{Q}'$  are the fluctuations in heat release rate and  $\zeta$  is the damping of the combustion system. In essence this criterion means that for an instability to occur, heat needs to be released at the moment of greatest pressure fluctuation and this needs to overcome the damping of the combustion system.

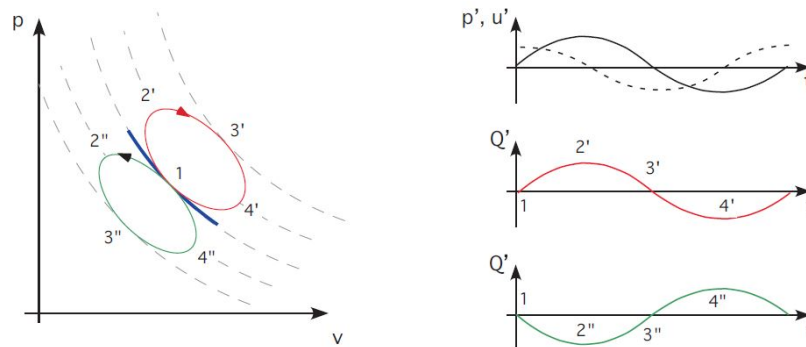


Figure 2.9: Thermodynamic interpretation of Rayleigh's stability criterion [33]

In figure 2.9 a thermodynamic interpretation of Rayleigh's stability criterion can be seen. Denoted by 1-2'-3'-4' in the  $p-v$  diagram is when heat addition occurs in phase with pressure fluctuations, while 1-2''-3''-4'' is the out of phase case, the dashed lines in this diagram are lines of constant entropy. While in the top right figure the fluctuations of pressure are denoted by the black line and the fluctuations of velocity are denoted by the dashed line [33]. Considering that sound waves are isentropic, the volume will move back and forth on an isentrope in the  $p-v$  diagram. If heat is added to the gas, this will lead to an increase of the specific volume  $v$  of the gas, and when this is in phase with the pressure fluctuations, the state of the gas volume moves clockwise around a thermodynamic cycle. This means that you are dealing with a thermo-acoustic heat engine, which feeds energy to the sound wave, which provides a basis for a self-excited stability to occur. However, acoustic energy might be lost elsewhere in the system, and if this loss increases the energy input from the fluctuating flame, a self-excited instability cannot occur. This means that the instability criterion is necessary, but not by itself a sufficient criterion for instability to occur [33].

### 2.4.4. Energy loss in the combustion system

For the combustion system to become unstable, the amplification has to overcome the damping in the system. The damping in the system is a result of acoustic losses. Under most conditions visco-thermal effects can dissipate a lot of the acoustic energy in ducts. In most combustion system these can however be neglected, as they are generally much smaller than the characteristic lengths of the system. Effects that can influence the acoustic energy dissipation are for example energy radiation at the boundaries or non-ideal reflection. Ideal reflection indicates that no energy is lost when an acoustic wave is reflected at a boundary,

with non-ideal reflection an amount of this energy will be lost at the boundary. Another effect can be vortex shedding, which can occur at edges between large area jumps. The acoustic energy will be converted into vortical energy which will be dissipated [3]. Another effect that can occur are acoustic losses due to turbulence generation. This can happen when mean flow is included or when large acoustic amplitudes are present. The turbulent flow, if at low mach number, does not have much effect on the acoustic field of the system, besides additional convective and damping effects [19] [43]. Determining the amount of damping in the annular combustion chamber is difficult. So for this thesis it will be assumed that the system becomes unstable when the reflection factor amplifies the acoustic pressure wave.

### 2.4.5. Characteristic time-delay and phasing analysis

The most important aspect for the occurrence of combustion instabilities are the in-phase fluctuations of process variables. If these do not happen in-phase, as mentioned above, the system will always remain stable. To further explain what is meant by this, figure 2.10 will be explained in short. More detailed explanations can be found in [25].

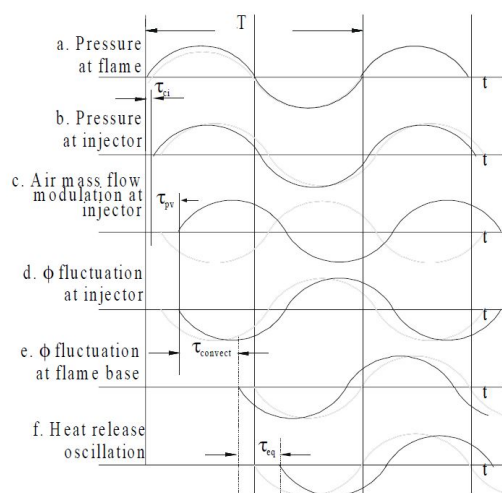


Figure 2.10: Evolution of pressure disturbances in an LNGT combustor [25]

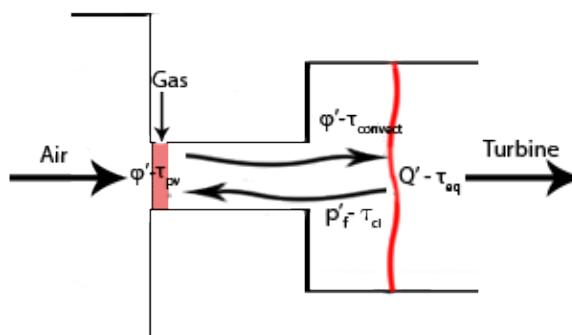


Figure 2.11: Representation of pressure disturbances through combustor system

In figure 2.10.a the pressure disturbance at the flame is shown, fluctuating along time. If this disturbance travels back towards the burner and influences the fuel injector pressure, there will be a small time delay before it reaches the fuel injector, which is called  $\tau_{ci}$  in figure 2.10.b. With these pressure disturbances a velocity fluctuation will occur, which influences the air flow rate in the fuel injector, figure 2.10.c. If the assumption is made that the gas injector is choked, the equivalence ratio fluctuations will be out of phase with the air flow fluctuations, figure 2.10.d, since an increase in air flow (if gas flow remains equal) will result in a lower equivalence ratio. The equivalence ratio fluctuation occurs in the burner and will travel towards the flame and reach the flame after a time  $\tau_{convect}$ , figure 2.10.e. This  $\tau_{convect}$  is the most dominant time delay in the system, so with that also the most important one to take into account [5]. The heat release will happen when all of the fuel is burned, which is after a time  $\tau_{eq}$ , figure 2.10.f. In this case the light grey line would be traveling perfectly in phase, as heat is released at the moment of highest pressure, see figure 2.10.a and 2.10.f. The black line does not travel in the exact same phase, but would be in the range that might provide combustion instabilities [25]. The most important thing to take from this is that; if the pressure and heat release travel in phase, this means that acoustic energy is fed to the system. This is a mandatory criterion for combustion instabilities to occur, but if more acoustic energy is lost somewhere else in the system than that is fed to the system by the coupling, instabilities will not occur. The pressure and heat release can be taken out of phase by changing the time-delays in the system. With the convective time-delay being the most dominant one, this is the one that influence the system stability the most.

## 2.5. Transfer matrix method

### 2.5.1. Introduction

The transfer matrix method can be used in acoustics to describe the propagation of an acoustic wave, in this case an acoustic pressure wave. Relations can be derived for all kinds of system components, e.g. ducts, area changes, nozzles, junctions, flames, walls etc. The acoustics will be assumed to have a harmonic time dependency, as explained in the chapter about wave solutions, and will also be assumed to have linear relations. This results in a system of components which can be described as a low order network model [33]. This describes the system of components in a linear system of equations, where the unknowns can be either the travelling acoustic pressure waves,  $p^+$  and  $p^-$ , or the acoustic pressure fluctuation and acoustic velocity fluctuation,  $p'$  and  $u'$ . In this thesis, the downstream and upstream travelling acoustic pressure waves,  $p^+$  and  $p^-$ , will be used. In this section different transfer matrix elements for geometric elements will be derived, in the next section transfer matrix boundary elements will be discussed and in the last section the transfer matrix element of the flame will be derived.

### 2.5.2. Transfer matrix element structure

In figure 2.12 an arbitrary element is shown in the transfer matrix notation. The upstream part of the element is denoted by 1 and the downstream part of the element is denoted as 2. The characteristics of the element are described in the matrix  $\underline{A}$ , this matrix is called the transfer matrix. In most cases the transfer matrix elements are described as 2x2 matrices. For ease of notation and usage throughout this thesis and the eventual model, the transfer matrices are rewritten in terms of a 2x4 matrix relating the pressure waves to a source term  $\mathbf{s}$ . This will result in a formulation which looks as follows:

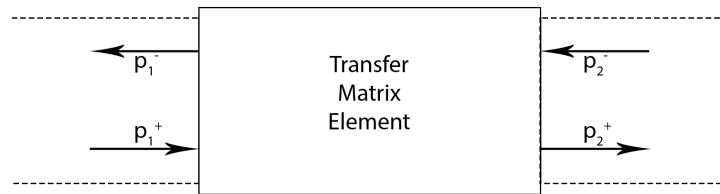


Figure 2.12: Transfer matrix element

$$[A] \mathbf{p} = \mathbf{s} \quad (2.26)$$

$$\begin{bmatrix} T_1 & T_2 & T_3 & T_4 \\ T_5 & T_6 & T_7 & T_8 \end{bmatrix} \cdot \begin{bmatrix} p_1^+ \\ p_1^- \\ p_2^+ \\ p_2^- \end{bmatrix} = \mathbf{s} \quad (2.27)$$

### 2.5.3. Element for an acoustic duct

The first element to be derived is that of a cylindrical duct with length  $L_{duct}$  with constant cross sectional area and mean flow  $U$ . As the only thing that happens in this duct is the propagation of the acoustic wave by the mean flow velocity  $U$ , the element can be described in terms of the harmonic wave solution (2.17.a) The acoustic pressure wave at node 2 is equal to the acoustic pressure wave at node 1 that has travelled a distance  $L_{duct}$ . The time dependency of the harmonic wave is not taken into account. So to couple  $p_1'$  to  $p_2'$  equation (2.19) has to be evaluated at  $x_1 = L$  for  $p_1'$  and at  $x_2 = 0$  for  $p_2'$

$$p_2^+ e^{-ik^+0} + p_2^- e^{ik^-0} = p_1^+ e^{-ik^+L_{duct}} + p_1^- e^{ik^-L_{duct}} \quad (2.28)$$

The transfer matrix will relate the positive travelling waves on node 1 and 2 to each other and separately from that the negative travelling waves on node 1 and 2.

$$p_1^+ e^{-ik^+L_{duct}} - p_2^+ = 0 \quad (2.29a)$$

$$p_1^- e^{ik^-L_{duct}} - p_2^- = 0 \quad (2.29b)$$

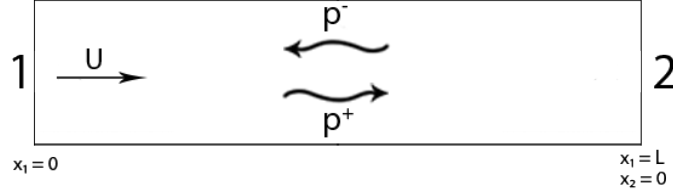


Figure 2.13: Cylindrical duct with nodes 1 and 2, at these nodes to duct can be coupled to other elements

These equations can be combined in the following matrix with a source term that is equal to the zero vector:

$$\begin{bmatrix} e^{-ik^+L_{duct}} & 0 & -1 & 0 \\ 0 & e^{ik^-L_{duct}} & 0 & -1 \end{bmatrix} \cdot \begin{bmatrix} p_1^+ \\ p_1^- \\ p_2^+ \\ p_2^- \end{bmatrix} = \mathbf{0} \quad (2.30)$$

#### 2.5.4. Element for an area change

When multiple ducts are connected, but an area change happens between the ducts an element of area change can be implemented. For the element of area change the linearized one-dimensional mass conservation equation will be used to. Both fluctuations in density  $\rho'$  and velocity  $u'$  will be taken into account.

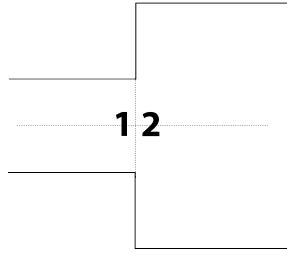


Figure 2.14: Area change element

$$S_1 \rho_1 u_1 = S_2 \rho_2 u_2 \quad (2.31)$$

$$S_1 \rho_1 u_1' + S_1 u_1 \rho_1' - S_2 \rho_2 u_2' - S_2 u_2' r h o_2' = 0 \quad (2.32)$$

Both  $u'$  and  $\rho'$  can be written in terms of  $p^+$  and  $p^-$ . The relation between  $u_i'$  and  $p_i'$  is a simplified version of the solutions for harmonic waves (2.17), where as the relation between density and pressure fluctuations is derived from the constitutive equation (2.7).

$$u_i' = \frac{p_i^+ - p_i^-}{\rho c} \quad (2.33a)$$

$$\rho_i' = \frac{p_i'}{c_i^2} \quad (2.33b)$$

$$\frac{S_1}{c_1} (p_1^+ - p_1^-) + \frac{S_1}{c_1} Ma_1 (p_1^+ + p_1^-) - \frac{S_2}{c_2} (p_2^+ - p_2^-) - \frac{S_2}{c_2} Ma_2 (p_2^+ + p_2^-) = 0 \quad (2.34)$$

With  $Ma_i = \frac{u_i}{c_i}$ , this equation can be rearranged and rewritten into the transfer matrix element. The second relation for this transfer matrix element comes from the linearized one-dimensional form of Bernoulli's equation, which is a statement of momentum conservation. In this case acoustic fluctuations in velocity, density and pressure will be taken into account.

$$\rho_1 u_1^2 + p_1 = \rho_2 u_2^2 + p_2 \quad (2.35)$$

$$\rho_1 u_1 u'_1 + u_1^2 \rho'_2 + p'_1 - \rho_2 u_2 u'_2 - u_2^2 \rho'_2 - p'_2 = 0 \quad (2.36)$$

Once again the acoustic velocity and density fluctuations (2.33) will be rewritten in terms of travelling pressure waves. After which the equation can be rearranged and added into the transfer matrix element (2.38).

$$Ma_1(p_1^+ - p_1^-) + Ma_1^2(p_1^+ + p_1^-) + (p_1^+ + p_1^-) - Ma_2(p_2^+ - p_2^-) - Ma_2^2(p_2^+ + p_2^-) - (p_2^+ + p_2^-) = 0 \quad (2.37)$$

$$\begin{bmatrix} \frac{S_1}{c_1}(1 + Ma_1) & \frac{S_1}{c_1}(Ma_1 - 1) & \frac{S_2}{c_2}(-1 - Ma_2) & \frac{S_2}{c_2}(1 - Ma_2) \\ 1 + Ma_1 + Ma_1^2 & 1 - Ma_1 + Ma_1^2 & -1 - Ma_2 - Ma_2^2 & -1 + Ma_2 - Ma_2^2 \end{bmatrix} \cdot \begin{bmatrix} p_1^+ \\ p_1^- \\ p_2^+ \\ p_2^- \end{bmatrix} = \mathbf{0} \quad (2.38)$$

### 2.5.5. Element for a junction

An element is required to describe the acoustics of a T-junction in pipe segments, see figure 2.15. This will be required for the junction where the fuel is added to the mixing chamber. In this junction the pressure will be assumed to be equal at all 3 points (2.39), while mass will have to be conserved. Again the linearized mass conservation equation (2.40) will be used to determine this relation, taking into account both velocity and density fluctuations (2.41).

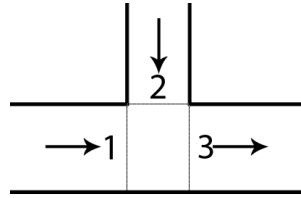


Figure 2.15: T-junction element

$$p'_1 = p'_2 = p'_3 \quad (2.39)$$

$$S_1 \rho_1 u_1 + S_2 \rho_2 u_2 = S_3 \rho_3 u_3 \quad (2.40)$$

$$S_1 \rho_1 u'_1 + S_1 u_1 \rho'_1 + S_2 \rho_2 u'_2 + S_2 u_2 \rho'_2 - S_3 \rho_3 u'_3 - S_3 u_3 \rho'_3 = 0 \quad (2.41)$$

In this case the flow direction suggests that the mass flowing from 1 and 2 has to be equal to the mass at 3, for problems with different flow directions this is subject to change. Again the velocity and density fluctuations will be written in terms of the travelling pressure waves (2.33), after which rearrangement of the equation (2.41) allows it to be implemented in the transfer matrix element (2.43)

$$\frac{S_1}{c_1}(p_1^+ - p_1^-) + \frac{S_1}{c_1} Ma_1(p_1^+ + p_1^-) + \frac{S_2}{c_2}(p_2^+ - p_2^-) + \frac{S_2}{c_2} Ma_2(p_2^+ + p_2^-) - \frac{S_3}{c_3}(p_3^+ - p_3^-) - \frac{S_3}{c_3} Ma_3(p_3^+ + p_3^-) = 0 \quad (2.42)$$

$$\begin{bmatrix} 1 & 1 & -1 & -1 & 0 & 0 \\ 1 & 1 & 0 & 0 & -1 & -1 \\ \frac{S_1}{c_1}(1 + Ma_1) & \frac{S_1}{c_1}(-1 + Ma_1) & \frac{S_2}{c_2}(1 + Ma_2) & \frac{S_2}{c_2}(-1 + Ma_2) & \frac{S_3}{c_3}(-1 - Ma_3) & \frac{S_3}{c_3}(1 - Ma_3) \end{bmatrix} \cdot \begin{bmatrix} p_1^+ \\ p_1^- \\ p_2^+ \\ p_2^- \\ p_3^+ \\ p_3^- \end{bmatrix} = \mathbf{0} \quad (2.43)$$

### 2.5.6. Element for a Helmholtz resonator

The workings of a Helmholtz resonator with mean flow outward will be used to describe the compressor plenum and gas supply, see figure 2.16. A Helmholtz resonator can be described as a volume, the cavity, which is connected with a small duct, called the neck. An unsteady mass flow which goes in/out of the neck will result in a volume increase/decrease in the cavity, which results in pressure fluctuations. The mass flow pushing into the volume can be seen as a mass-spring system. The mass entering/leaving the volume can be described using equation (2.44), using that equation the density fluctuation inside the cavity can be described using equation (2.45)

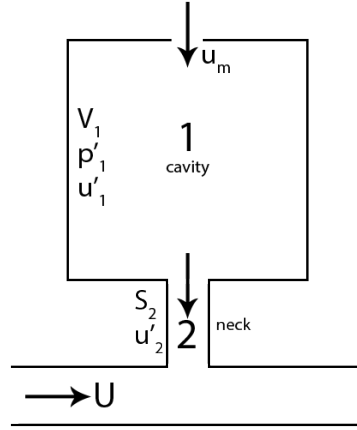


Figure 2.16: Helmholtz Resonator with mean flow

$$\dot{m} = \bar{\rho} S u \quad (2.44)$$

$$\frac{d\rho'_1}{dt} = \frac{\dot{m}}{V_1} \quad (2.45)$$

The mass flow is assumed to be a fluctuating parameter, so the acoustic velocity fluctuation in the neck has to be used in equation (2.44), which results in equation (2.46). Equation (2.47) results from combining equation (2.46) and (2.7). The acoustic pressure fluctuation in the cavity is a sinusoidal disturbance, so  $\frac{d}{dt}$  can be substituted by  $i\omega$ . Using the relationship between acoustic velocity and pressure fluctuations, equation (2.49) can be rewritten in terms of the downstream and upstream travelling pressure waves.

$$\frac{d\rho'_1}{dt} = \frac{\bar{\rho} S_2 u'_2}{V} \quad (2.46)$$

$$\bar{c}^2 \frac{d\rho'_1}{dt} = \frac{\bar{\rho} S_2 u'_2}{V} \quad (2.47)$$

$$i\bar{c}^2 \omega p'_1 = \frac{\bar{\rho} S_2 u'_2}{V_1} \quad (2.48)$$

$$p'_1 = \frac{\bar{c}^2 \bar{\rho} S_2 u'_2}{i\omega V_1} \quad (2.49)$$

$$p_1^+ + p_1^- = \frac{\bar{c}^2 \bar{\rho} S_2}{i\omega V_1} \frac{p_2^+ - p_2^-}{\bar{\rho} c_2} \quad (2.50)$$

The second term for the transfer matrix element of the Helmholtz Resonator will be determined from the momentum conservation equation.

$$\frac{\partial \rho u}{\partial t} + \frac{\partial \rho u u}{\partial x} = -\frac{\partial p}{\partial x} \quad (2.51)$$

For  $\rho$  the mean value ( $\bar{\rho}$ ) without a fluctuating term is taken, while for  $u$  the mean value plus a fluctuating velocity will be used,  $\bar{u} + u'$ . The mean flow velocity is constant, so that will not depend on time. This will change equation (2.51) into the following equation:

$$\frac{\partial \rho u'}{\partial t} + \frac{\partial \rho(\bar{u} + u')(\bar{u} + u')}{\partial x} = -\frac{\partial p}{\partial x} \quad (2.52)$$

$$\frac{\partial \rho u'}{\partial t} + \frac{\partial(\bar{\rho} \bar{u}^2 + 2\bar{\rho} \bar{u} u' + \bar{\rho} u'^2)}{\partial x} = -\frac{\partial p}{\partial x} \quad (2.53)$$

The term containing the quadratic term of the mean flow velocity is crossed out as well as the quadratic term for the fluctuating flow velocity.

$$\bar{\rho} \frac{\partial u'}{\partial t} + 2\bar{\rho} \frac{\partial \bar{u} u'}{\partial x} = -\frac{\partial p}{\partial x} \quad (2.54)$$

$$L_2 S_2 \bar{\rho} \frac{\partial u'_2}{\partial t} + 2S_2 \bar{\rho} \cdot (\bar{u} u'_2 - \bar{u} u'_1) = -S_2 \cdot (p'_2 - p'_1) \quad (2.55)$$

Assuming that the mean flow velocity in the cavity of the resonator is negligible in comparison to the flow velocity through the neck, that term can be canceled.

$$i\omega L_2 S_2 \bar{\rho} u'_2 + 2S_2 \bar{\rho} \cdot \bar{u} u'_2 = -S_2 \cdot (p'_2 - p'_1) \quad (2.56)$$

Using the relation between the acoustic velocity and acoustic pressure fluctuations, equation (2.56) can be written in terms of  $p^+$  and  $p^-$ .

$$\left( \frac{i\omega L S_2}{c_2} + \frac{2S_2 \bar{u}_2}{c_2} \right) \cdot (p_2^+ - p_2^-) + S_2 \cdot (p_2^+ + p_2^-) + S_2 \cdot (-p_1^+ - p_1^-) = 0 \quad (2.57)$$

Which leaves us with the following representation of the transfer matrix element for the Helmholtz Resonator.

$$\begin{bmatrix} 1 & 1 & -\frac{c^2 S_2}{i\omega V_1 c_2} & \frac{c^2 S_2}{i\omega V_1 c_2} \\ -S_2 & -S_2 & \frac{i\omega L S_2}{c^2} + \frac{2S_2 u_2}{c_2} + S_2 & -\frac{i\omega L S_2}{c^2} - \frac{2S_2 u_2}{c_2} + S_2 \end{bmatrix} \cdot \begin{bmatrix} p_1^+ \\ p_1^- \\ p_2^+ \\ p_2^- \end{bmatrix} = \mathbf{0} \quad (2.58)$$

### 2.5.7. Acoustic boundary conditions

The acoustic boundary elements have a different structure as opposed to the other transfer matrix elements. Acoustic boundary elements are only dependent of two pressure terms, one upstream travelling pressure waves and one downstream travelling pressure wave, so just one set of  $p^+$  and  $p^-$  (2.59). They are mostly used as beginning or end conditions of an acoustic network model.

$$[T1 \quad T2] \cdot \begin{bmatrix} p^+ \\ p^- \end{bmatrix} = 0 \quad (2.59)$$

#### Closed end boundary element

Consider the closed end to be, for example, a rigid wall. Acoustic velocity fluctuations normal to the wall will disappear [21]. This acoustic velocity fluctuation can be written in terms of  $p^+$  and  $p^-$ , which results in our boundary element, equation (2.61).

$$u' = \frac{p^+ - p^-}{\rho c} = 0 \quad (2.60)$$

$$[1 \quad -1] \cdot \begin{bmatrix} p^+ \\ p^- \end{bmatrix} = 0 \quad (2.61)$$

#### Open end boundary element

At an open end, the acoustic pressure fluctuation will disappear. Writing the acoustic pressure fluctuation in terms of  $p^+$  and  $p^-$ , will result in our boundary element, equation (2.62)

$$p' = p^+ + p^- = 0 \quad (2.62)$$

$$[1 \quad 1] \cdot \begin{bmatrix} p^+ \\ p^- \end{bmatrix} = 0 \quad (2.63)$$

#### Choked nozzle outlet boundary element

In case an outlet is neither open or closed, there are also choked outlet nozzle outlets, see figure 2.17. The outlet from the combustion chamber into the turbine is an example of a choked nozzle. This choked nozzle outlet condition is derived from a condition provided by Dowling & Stow [12]. Note that this condition will be derived just in front of the nozzle outlet, at a single plane as shown in figure 2.17.

$$2 \frac{u'}{u} + \frac{\rho'}{\rho} - \frac{p'}{p} = 0 \quad (2.64)$$

Rewriting everything in terms of travelling pressure waves using equation (2.33) results in the following outlet condition, which will be rearranged into a matrix element:

$$\frac{2}{u\rho c}(p^+ - p^-) + \frac{1}{\rho c^2}(p^+ + p^-) - \frac{1}{p}(p^+ + p^-) = 0 \quad (2.65)$$

$$\left[ \frac{2}{u\rho c} + \frac{1}{\rho c^2} - \frac{1}{p} \quad -\frac{2}{u\rho c} + \frac{1}{\rho c^2} - \frac{1}{p} \right] \cdot \begin{bmatrix} p^+ \\ p^- \end{bmatrix} = 0 \quad (2.66)$$

### Choked nozzle inlet boundary element

The other case might be that the inlet of a system will be choked, see figure 2.69. The air flow into a combustion chamber will come from the compressor plenum, which is a large area, and flows into the burner with significantly smaller area's. For this derivation another condition provided by Dowling & Stow [12] will be used, this condition has to be evaluated just downstream of the choking plane as can be seen in figure 2.18.

$$\frac{\rho'}{\rho} + \frac{u'}{u} = 0 \quad (2.67)$$

The same procedure as for the choked outlet element will be followed, rewriting and rearranging the equation into a matrix element.

$$\frac{1}{\rho c^2}(p^+ + p^-) + \frac{1}{u\rho c}(p^+ - p^-) = 0 \quad (2.68)$$

$$\begin{bmatrix} \frac{1}{\rho c^2} + \frac{1}{u\rho c} & \frac{1}{\rho c^2} - \frac{1}{u\rho c} \end{bmatrix} \cdot \begin{bmatrix} p^+ \\ p^- \end{bmatrix} = 0 \quad (2.69)$$

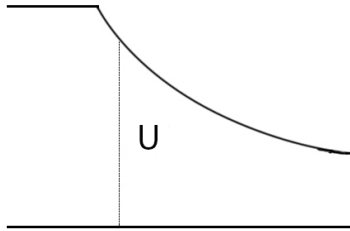


Figure 2.17: Choked nozzle outlet

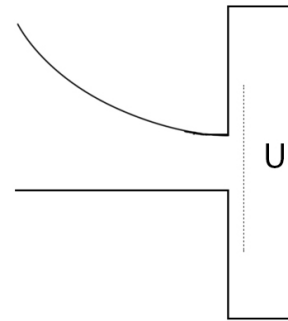


Figure 2.18: Choked nozzle inlet

## 2.6. Flame transfer function

### 2.6.1. Introduction

The flame transfer function is the element that will describe the response of the flame to perturbations in flow parameters happening upstream of the flame. This function describes the fluctuating or unsteady heat release that occurs at the flame front during combustion. This unsteady heat release will be the main reason for the occurrence of combustion instabilities. As mentioned in the previous chapters, the unsteady heat release is related to the acoustic pressure fluctuations that travel through the combustion system. When the heat release fluctuations occur in phase with the acoustic waves they can amplify each other, which can result in ever increasing pressure amplitudes. The flame transfer function will provide a relation between these fluctuations. First the conditions across a flame front will be analyzed with the conservation equations. After that a general formulation of a simple flame transfer function will be explained, after which a more complex function will be used. This last function will take into account both direct and indirect effects of equivalence ratio fluctuations and velocity fluctuations being convected to the flame front and subsequently being burnt.

### 2.6.2. Conservation equations

To determine the transfer function of the flame, the Navier Stokes equations across the flame will be used. In these equations, subscript 1 denotes the conditions upstream of the flame, while subscript 2 denotes the conditions downstream of the flame, figure 2.19. The conditions, so called jump conditions, across the flame will be derived for an acoustically compact flame [32]. This assumption is made as this thesis will look into oscillation frequencies no higher than 300 Hz. For this frequency the acoustic wave length will be  $\lambda_{ac} = \frac{c_{cc}}{f} \approx 2.7m$ , which is assumed to be significantly larger than the flame zone. This means the flame can be assumed compact.

One condition will be derived from the Navier Stokes momentum equation (2.70a). Simplifying this equation by assuming that viscous stresses are negligible, as well as neglecting convective derivatives results in (2.70b) [32]. Integrating this between 1 and 2, going to the limit of  $x_f - x_1 \rightarrow 0$  and  $x_2 - x_f \rightarrow 0$  results in the first relation (2.70c).

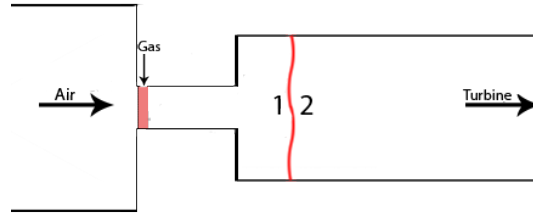


Figure 2.19: Thin premixed, compact flame; 1 denotes pre-combustion conditions; 2 denotes post-combustion conditions

$$\rho \frac{Du}{Dt} = -\nabla p + \nabla \cdot \tau \quad (2.70a)$$

$$\frac{\partial u}{\partial t} = -\frac{1}{\rho_0} \frac{\partial p}{\partial x} \quad (2.70b)$$

$$p'_1 = p'_2 \quad (2.70c)$$

The second condition will be derived from the statements of mass, momentum and energy conservation (2.71) [12]. Duct areas in regions 1 and 2 are not taken into account in the statement of mass conservation. The conservation equations are evaluated very close to the thin flame, where the assumption will be that  $S_1 = S_2$ .

$$\rho_1 u_1 = \rho_2 u_2 \quad (2.71a)$$

$$p_1 + \rho_1 u_1^2 = p_2 + \rho_2 u_2^2 \quad (2.71b)$$

$$\rho_1 u_1 h_1 + Q_f = \rho_2 u_2 h_2 \quad (2.71c)$$

With  $h = c_p T + \frac{1}{2} u^2$  being the stagnation enthalpy. The mean flow in the combustor will be at low Mach number, which results in large entropy fluctuations downstream of the flame [12]. Equation (2.71a) can be used to rewrite equation (2.71c) into a form where linear fluctuations are taken into account.

$$\bar{\rho}_1 \bar{u}_1 (c_p T_1' + \bar{u}_1 u_1') - (\bar{h}_2 - \bar{h}_1) (\bar{\rho}_1 u_1' + \rho_1' \bar{u}_1) + Q' = \bar{\rho}_2 \bar{u}_2 (c_p T_2' + \bar{u}_2 u_2') \quad (2.72)$$

As the equations are rewritten to get back to the jump conditions for zero mean flow, as is also the case in (2.70), equation (2.72) will be evaluated for  $u_1 \rightarrow 0$  and  $u_2 \rightarrow 0$ . This reduces that equation (2.72) to:

$$H_1 \rho_1 u_1' - H_2 \rho_1 u_1' + Q' = \rho_2 u_2 c_p T_2' \quad (2.73)$$

$$c_p T' = \frac{p'}{\rho_2} + \frac{s c_2^2}{(\gamma - 1) c_p} e^{i\omega(t - \frac{d_f}{u_2})} \quad (2.74)$$

In this case  $s$  is the strength of the entropy wave,  $d_f$  is the length of the flame zone,  $c_p$  is the specific heat at constant pressure and  $\gamma = \frac{c_p}{c_v}$  is the ratio of specific heats. This seems to be inconsistent, as the term  $u_2$  is kept on the right hand side of the equation. This is done by Dowling [12] as the right hand side of the equation will evaluate into a term containing  $u_2 s$ , by using equation (2.74). If in this case  $u_2$  will be taken to zero, the strength of the entropy wave  $s$  will be taken to infinity. This allows the term  $u_2 s$  to remain finite even for very small  $u_2$ . Further evaluation and combining of equations (2.73) and (2.74) results in:

$$Q' - c_p (T_2 - T_1) \rho_1 u_1' = \frac{\rho_2 u_2 c_2^2}{c_p (\gamma - 1)} s e^{i\omega(t - \frac{d_f}{u_2})} \quad (2.75)$$

This equation shows that there is unsteady entropy generation when  $Q' \neq c_p (T_2 - T_1) \rho_1 u_1'$  [12]. The RHS of equation (2.75) can be rearranged as can be seen in equation (2.76). Using another relation provided by Dowling [12] for the density fluctuation, equation (2.77), and the constitutive equation (2.7) this RHS can then be rewritten and implemented in equation (2.75) which results in (2.78).

$$\frac{\rho_2 u_2 c_2^2}{c_p (\gamma - 1)} s e^{i\omega(t - \frac{d_f}{u_2})} = \frac{s \rho_2}{c_p} e^{i\omega(t - \frac{d_f}{u_2})} \frac{u_2 c_2^2}{(\gamma - 1)} \quad (2.76)$$

$$\rho' = \frac{p'}{c_2^2} - \frac{s \rho_2}{c_p} e^{i\omega(t - \frac{d_f}{u_2})} \quad (2.77)$$

$$Q' - c_p (T_2 - T_1) \rho_1 u_1' = -\frac{u_2 c_2^2}{\gamma - 1} \rho_2' \quad (2.78)$$

The last step is to rewrite equation (2.78) in terms of  $u_2 \rho_2'$  as that can be used in the linearized conservation of mass equation. So divide equation (2.78) by the term  $-\frac{c_2^2}{\gamma - 1}$ . Relationships derived by Dowling [12] for perfect gas rewrites the first term on the right hand side of (2.79) as  $(\rho_1 - \rho_2) u_1'$ . Using that relation and substituting this into the conservation of mass equation, results in the jump condition across the flame (2.80).

$$u_2 \rho_2' = \frac{c_p (T_2 - T_1) (\gamma - 1) \rho_1}{c_2^2} u_1' - \frac{\gamma - 1}{c_2^2} Q' \quad (2.79)$$

$$u_1' = u_2' - \frac{\gamma - 1}{\rho_2 c_2^2} Q' \quad (2.80)$$

These jump conditions are also derived by Poinot [32] and by Ducruix et al. [13]. Equations (2.70c) and (2.80) will be transformed into a transfer matrix element (2.81), which can be implemented in the model.

$$\begin{bmatrix} 1 & 1 & -1 & -1 \\ \frac{1}{\rho_1 c_1} & -\frac{1}{\rho_1 c_1} & -\frac{1}{\rho_2 c_2} & \frac{1}{\rho_2 c_2} \end{bmatrix} \cdot \begin{bmatrix} p_1^+ \\ p_1^- \\ p_2^+ \\ p_2^- \end{bmatrix} = \begin{bmatrix} 0 \\ -\frac{\gamma - 1}{\rho_2 c_2^2} Q' \end{bmatrix} \quad (2.81)$$

The positive and negative travelling waves can be transformed into wave form,  $p'$ , using (2.17a). This incorporates the time-dependency and location dependency on the pressure wave as is seen in the original wave equation and have been shown to be solutions to the convective homogeneous wave equation (2.16). The source term on the right hand side of the matrix is equal to the unsteady heat release term that is found in the right hand side of the original wave equation (2.10). The next step is to derive conditions for the unsteady heat release  $Q'$  in terms of acoustic pressure perturbations throughout the combustion system. This will eventually remove the  $Q'$  from the source term in the transfer matrix (2.81) and allows it to be rewritten as a function of the travelling pressure waves.

### 2.6.3. $n - \tau$ method for flame transfer function

The basics of the flame transfer function are based on the so called  $n - \tau$  method [12] for flame transfer function.  $n$  is called the interaction index, where-as  $\tau$  is a time-delay in seconds. They are usually represented in a form as follows:

$$H_f = \frac{Q'_i}{u'_i} = n e^{-i\omega\tau} \quad (2.82a)$$

$$Q'_i = H_f u'_i = u'_i n e^{-i\omega\tau} \quad (2.82b)$$

Here  $H_f$  is the transfer function of the flame, as a function of the fluctuating heat release and a fluctuating velocity at location  $i$ ,  $u'_i$ . The fluctuating velocity at location  $i$  will result in a change of convected mass flow towards the flame front. If a different amount of the fuel mixture is combusted, this results in a different and thus unsteady heat release. The  $n - \tau$  method allows the fluctuating heat release to be rewritten in terms of the flame transfer function and a fluctuating parameter, in this case  $u'_i$ , as can be seen in (2.82). A basic relation between the fluctuating heat release  $Q'$  and the oscillating  $m'_i$ , an air mass flow fluctuation at the burner mouth, is used by Dowling [12].

$$\frac{Q'}{\bar{Q}} = -k \frac{m'_i}{m_i} e^{-i\omega\tau} \quad (2.83)$$

The time-delay  $\tau$  will be the time it takes for this mass flow fluctuation to convect towards the flame front.  $\bar{Q}$  denotes the mean heat release. The mass flow fluctuation can be written in terms of an acoustic velocity perturbation using the conservation of mass equation (keeping density constant). Which allows (2.83) to be described as a flame transfer function.

$$\frac{Q'}{\bar{Q}} = -\frac{k}{m_i} S_i \rho_i u'_i e^{-i\omega\tau} \quad (2.84a)$$

$$\frac{Q'}{u'_i} = -\frac{k}{m_i} S_i \rho_i \bar{Q} e^{-i\omega\tau} = H_f \quad (2.84b)$$

In this case the amplification factor is  $n = -\frac{k}{m_i} S_i \rho_i \bar{Q}$ . Equation (2.84b) shows that if a flame transfer function is known, it can be used to describe the fluctuating heat release, which can be used in the flame transfer matrix (2.81) to describe flame behaviour. For this the mass flow fluctuation has to be written in terms of positive and negative direction travelling pressure waves, using (2.17). That term can be incorporated into the flame transfer matrix (2.81), which means  $Q'$  can now be taken out of the source term and be written in terms of fluctuating parameters.

$$Q' = -k \frac{S_i}{m_i c_i} e^{-i\omega\tau} (p_i^+ - p_i^-) \quad (2.85)$$

Cho & Lieuwen [6][26] have derived flame transfer functions of the sort (2.82), which incorporate both direct and indirect effects of equivalence ratio fluctuations in the mixing chamber and velocity fluctuations at the burner mouth.

### 2.6.4. Flame transfer function

The flame transfer function (FTF) used in the simple combustor model, equation (2.83), just relates the unsteady heat release to a fluctuation of mass at the burner outlet. As mentioned before, this will not be the only factor that influences the unsteady heat release at the flame. For the eventual gas turbine model, the more elaborate and complicated FTF, a function derived by Cho & Lieuwen[6][26] for a laminar, premixed flame will be used. This model couples unsteady heat release to both velocity fluctuations and equivalence ratio fluctuations. A flame model that incorporates these effects is a more realistic form of a flame transfer function as opposed to the simple model. Due to the lean combustion the flame is especially sensitive to perturbations in equivalence ratio, due to a large effect on flame speed. In this case the fluctuating heat release will be linearized and have the form of equation (2.86). Where  $F_u$  and  $F_\phi$  will be introduced later in this section.

$$\frac{Q'}{\bar{Q}} = \frac{Q'}{\bar{Q}_u} + \frac{Q'}{\bar{Q}_\phi} = F_u \frac{u'_b}{\bar{S}_u} + F_\phi \frac{\phi'_m}{\bar{\phi}} \quad (2.86)$$

$\phi'$  and  $u'$  will be the fluctuating parameters that drive the heat release. The global heat release will be written as in (2.87). Where the density  $\rho$ , flame speed  $S_u$  and heat of reaction  $\Delta H_r$  are integrated over the instantaneous flame area  $A_f$ . If any of these parameters are changed due to acoustic fluctuations, the heat release changes which means it becomes unsteady. However the assumption will be made that the density of the mixture will remain constant [26]. This is done by Lieuwen as an unreported analysis shows that this is a valid assumption as long as the square of the mean flow Mach number in the premixer remains small with respect to unity [26]. Figure 2.20 shows a simplified combustor geometry that also incorporates the convection of the equivalence ratio fluctuations in the mixing section and the velocity fluctuations at burner outlet. In this geometry the flame is shown as a thin flame sheet in the combustor, where-as the derivation of the flame function will make use of a geometric factor  $\beta$  for a conical flame. The flame length  $L_f$  will be known as the length from burner outlet towards the flame front.

$$Q(t) = \int_{A_f} \rho S_u \Delta H_r dA_f \quad (2.87)$$

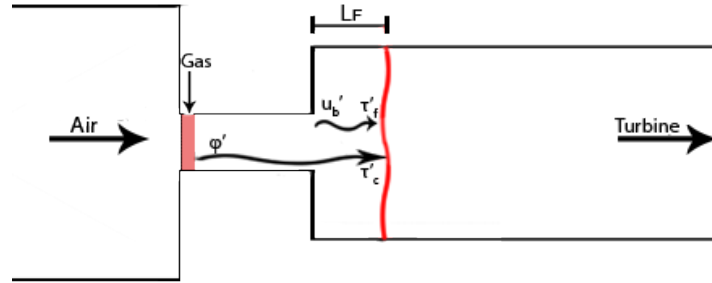


Figure 2.20: Simple combustor interpretation showing the perturbations convecting through the system

### Flame speed and heat of reaction

In the flame transfer function the (laminar) flame speed [6] and the heat of reaction [6] will be determined as a function of the equivalence ratio .

$$S_u(\phi) = K_c A \phi^B e^{-C(\phi-D)^2} \quad (2.88)$$

With  $A = 0.6079$ ,  $B = -2.554$ ,  $C = 7.31$  and  $D = 1.230$  [6].

$$\Delta H_R(\phi) = K_h \frac{2.9125 \times 10^6 \min(1, \phi)}{1 + 0.05825 \phi} \quad (2.89)$$

These are values that are valid for methane at 300K and 1 atm. The most important result of both these relations is the response of  $\frac{dS_u}{d\phi}$  and  $\frac{d\Delta H_R}{d\phi}$ . Especially the flame speed will have a very steep gradient at low equivalence ratio, which makes the lean flame very sensitive to perturbations in process parameters. The value for  $K_c$  can be adjusted to increase/decrease the response of  $S_u$  to perturbations in  $\phi$ . There is little data to be found about the exact relations between these parameters and the pressure and temperature. It is however shown by Wu et al. [45] that the steepness of  $\frac{dS_u}{d\phi}$  increases by increasing the mixture temperature, see figure (2.21). To oppose that effect, at higher pressures the gradient of the response seems to flatten out [10] as can be seen in figure (2.22). The exact value of  $K_c$  that will be used will be determined in the eventual model by sensitivity analysis. The same analysis will be done for different values of  $K_h$  which will influence the heat of reaction model.

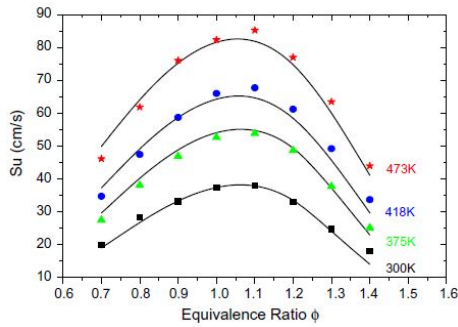


Figure 2.21: Laminar flame speed of a methane/air mixture as a function of the equivalence ratio at various temperatures and atmospheric pressure; symbols - experimental data; lines - modelled data; from Wu et al. [45]

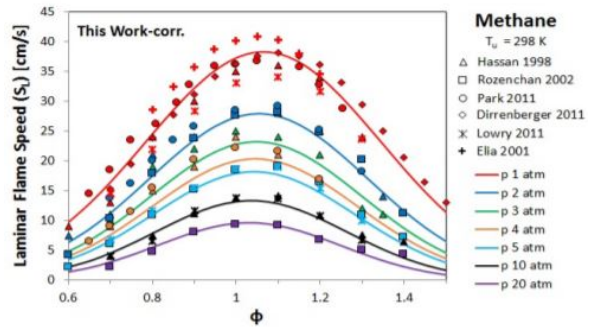


Figure 2.22: Laminar flame speed of a methane/air mixture as a function of the equivalence ratio at various pressure and room temperature; symbols - experimental data; lines - empirical correlation; from Distaso [10]

### Equivalence ratio perturbations

The derivation and analysis of the influence of the equivalence ratio perturbation on unsteady heat release also follows that of Cho and Lieuwen [6]. A perturbation in equivalence ratio can have a large effect on the unsteady heat release. This perturbation happens by a perturbation in air mass flow and/or fuel mass flow at the injection point of the fuel. With a perturbation in one or both of these flow parameters, the fuel mixture that is convected towards the flame front will have a changed composition. A different fuel mixture will have a different heat release at the flame, as the chemical kinetics of the fuel are changed [21].

There are three distinct relations that influence the heat release due to a perturbation in equivalence ratio [26], which can also be related to (2.87). There is a relation with the heat of reaction ( $F_H$ ), which depends on the heat content and composition of the fuel mixture. This changes due to differences in amount of gas that is present in the fuel mixture as a result of fluctuations of gas mass flow. There also is a direct relation between the flame speed and the equivalence ratio perturbation ( $F_{S,dir}$ ), which adds to the unsteady heat release. The last term is the indirect relation between the flame area and equivalence ratio perturbation ( $F_A$ ), which is due to the change in flame area as a function of the flame speed. This flame transfer function relates to the unsteady heat release as shown in equation (2.90) [26]. An illustration of the direct and indirect influences of the equivalence ratio fluctuations are shown in figure 2.23, which graphically shows what the terms in equation (2.91) represent.

$$F_\phi = \frac{Q' / \bar{Q}\phi'}{\phi'_m / \bar{\phi}} = F_H + F_S = F_H + (F_{S,dir} + F_A) \tag{2.90}$$

$$F_H = \frac{d(\Delta h_R / \Delta \bar{h}_R)}{d(\phi / \bar{\phi})} \Big|_{\bar{\phi}} \frac{\beta^4}{St^2} \left[ 1 + \frac{iSt}{\beta^2} - e^{\frac{iSt}{\beta^2}} \right] \tag{2.91a}$$

$$F_{S,dir} = \frac{d(S_u / \bar{S}_u)}{d(\phi / \bar{\phi})} \Big|_{\bar{\phi}} \frac{\beta^4}{St^2} \left[ 1 + \frac{iSt}{\beta^2} - e^{\frac{iSt}{\beta^2}} \right] \tag{2.91b}$$

$$F_A = \frac{d(S_u / \bar{S}_u)}{d(\phi / \bar{\phi})} \Big|_{\bar{\phi}} \frac{2\beta^4}{St^2(\beta^2 - 1)} \left[ 1 - \frac{1}{\beta^2} + \frac{e^{iSt}}{\beta^2} - e^{\frac{iSt}{\beta^2}} \right] \tag{2.91c}$$

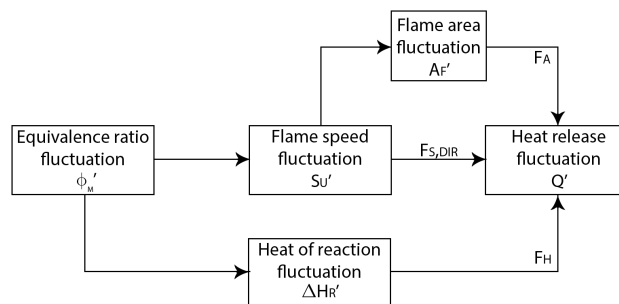


Figure 2.23: Direct and indirect influence of equivalence ratio fluctuations on heat release

Where  $\phi'_f$  is the equivalence ratio fluctuation at the flame as a function of the equivalence ratio fluctuation at the mixing location and the time-delay  $\tau_c$  for convection to the flame front.  $\beta$  is a geometric factor derived by Cho & Lieuwen [6] which is a function of the flame length  $L_f$ , the burner outlet radius  $R$  and the flame position. In this case the flame position is taken as the mean flame position.  $St$  is the Strouhal number which depends upon  $\beta$ ,  $\omega$ ,  $R$  and the flame speed  $S_u$ . This is also called the reduced frequency by Ducruix et al. [14] and is used to describe the response of the burner to acoustic perturbations, as a function of the burner geometry and flame properties.

$$\phi'_f = \phi'_m e^{-i\omega\tau_c} \quad (2.92a)$$

$$\beta = \sqrt{\frac{R^2}{L_f^2} + 1} \quad (2.92b)$$

$$St = \frac{\beta\omega R}{S_u} = \frac{\beta^2\omega L_f}{\bar{u}} \quad (2.92c)$$

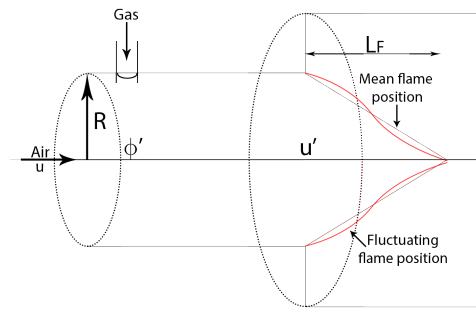


Figure 2.24: Conical flame on burner outlet, fluctuating flame position

### Velocity perturbation

The derivation and analysis of the influence of the velocity perturbation on the unsteady heat release follows that of Fleifil et al. [15] and Ducruix et al. [14]. This is also the relation that is used by Lieuwen [26].

In the case of velocity fluctuations, the acoustic waves in the combustion chamber allow for a velocity perturbation in the burner mouth. This velocity perturbation changes the mass flow that is transported towards the flame front. A change in mass flow from the burner mouth results in a different amount of combusted premix gases. This will have an effect on the total chemical enthalpy burnt at the flame [21] due to either an increase/decrease of combustion fuel flow. But since the fuel flow is a small fraction of the mass at burner outlet, the biggest influence will be on the flame area due to an increase in air flow. This flame area effect is modelled by Cho & Lieuwen [6] by integrating the unsteady heat release over the fluctuating flame front and thus fluctuating flame area. The effect of this flame area fluctuation is captured in equation (2.93) as a function of the Strouhal number. A graphical representation of this response is shown in figure 2.25.

$$F_u = \frac{Q'/\bar{Q}_u'}{u'_b/\bar{S}_u} \quad (2.93a)$$

$$F_u = \frac{2}{St^2} [1 + iSt - e^{iSt}] \quad (2.93b)$$

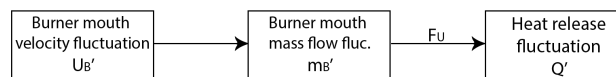


Figure 2.25: Direct influence of velocity fluctuations at burner outlet on heat release

### 2.6.5. Flame transfer function response

Below the reponse of the flame transfer function derived by Cho & Lieuwen [6], which also followed Fleifil et al. [15] and Ducruix et al. [14], is plotted. Figures 2.26 and 2.27 plot the magnitude and phase of the flame transfer function versus Strouhal number. In figure 2.28 and 2.29 the magnitude and phase of the flame transfer function is plotted versus frequency. The phase response is expected to decrease with frequency in the flame transfer function. This will be corrected when the final transfer function is derived, when the unsteady heat release is rewritten in terms of  $F$  and velocity or pressure perturbations.

These plots are exactly the same as the plots provided in Cho & Lieuwen [6]. This shows that the flame transfer function is correctly implemented and allows it to be rewritten in terms of unsteady heat release.

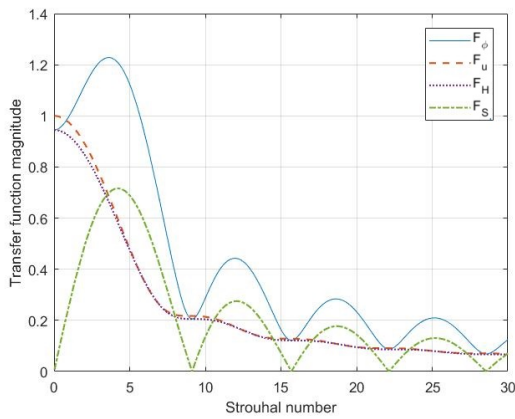


Figure 2.26: Flame transfer function magnitude for  $\phi = 0.5$  versus Strouhal number

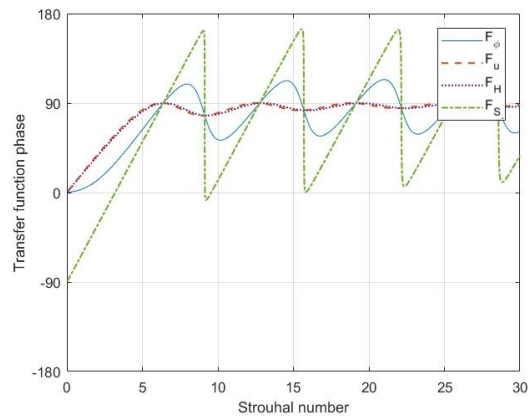


Figure 2.27: Flame transfer function phase for  $\phi = 0.5$  versus Strouhal number

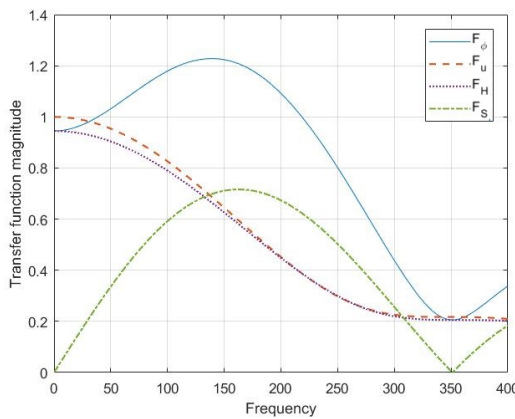


Figure 2.28: Flame transfer function magnitude for  $\phi = 0.5$  versus frequency

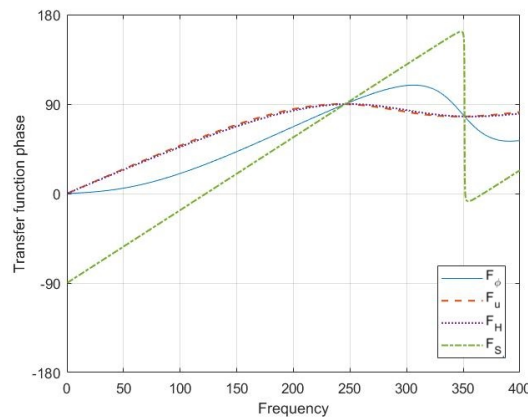


Figure 2.29: Flame transfer function phase  $\phi = 0.5$  versus frequency

### 2.6.6. Unsteady heat release

Equations (2.90), (2.91) and (2.93) can now be rewritten in terms of the unsteady heat release  $Q'$ . This function can be implemented into our transfer matrix element for the flame (2.81), if everything is described in terms of travelling acoustic pressure waves in the combustion system.

First (2.93.a) will be rewritten, for ease of notation  $F_u$  will be kept and assumed to be equal to (2.93.b):

$$Q'_u = \frac{F_u \bar{Q}}{\bar{S}_u} u'_f \quad (2.94a)$$

$$Q'_u = \frac{F_u \bar{Q}}{\bar{S}_u} u'_b e^{-i\omega\tau_f} \quad (2.94b)$$

$$Q'_u = \frac{F_u \bar{Q}}{\bar{S}_u \rho_b c_b} e^{-i\omega\tau_f} [p_b^+ - p_b^-] \quad (2.94c)$$

$u'_f$  is the velocity fluctuation from the burner mouth ( $u'_b$ ) arriving at the flame front after a time-delay  $\tau_f$ , which is the convection time from burner outlet to flame front.  $\rho_b$  and  $c_b$  are respectively the density and speed of sound in the burner mouth. Equation (2.94c) can now be used in the flame transfer matrix (2.81). Incorporating this function does change the dimensions of (2.81) as it also has to span the pressure nodes at other locations in the combustion system.

Next the equation (2.90) will be rewritten in terms of  $Q'$ . Again notations of  $F_\phi$  will remain for ease of notation. In the eventual result  $F_\phi$  can be substituted with the results of equation (2.91). First the term for  $\phi'$  has to be rewritten in terms of fluctuating air and fuel mass flows, which can then be rewritten in terms of fluctuating acoustic velocities.

$$\frac{\phi'}{\bar{\phi}} \approx \frac{\dot{m}'_g}{\bar{m}_g} - \frac{\dot{m}'_a}{\bar{m}_a} \quad (2.95a)$$

$$\phi' = \frac{\bar{\phi}}{\bar{m}_g} \rho_g S_g u'_g - \frac{\bar{\phi}}{\bar{m}_a} \rho_a S_a u'_a \quad (2.95b)$$

Now (2.95) can be substituted into the equation for unsteady heat release, which allows everything to be described in terms of acoustic waves.

$$Q'_\phi = \frac{F_\phi \bar{Q}}{\bar{\phi}} \phi'_f \quad (2.96a)$$

$$Q'_\phi = \frac{F_\phi \bar{Q}}{\bar{\phi}} \phi'_i e^{-i\omega\tau_c} \quad (2.96b)$$

$$Q'_\phi = \frac{F_\phi \bar{Q}}{\bar{\phi}} e^{-i\omega\tau_c} \left[ \frac{\bar{\phi}}{\bar{m}_g} \rho_g S_g u'_g - \frac{\bar{\phi}}{\bar{m}_a} \rho_a S_a u'_a \right] \quad (2.96c)$$

$$Q'_\phi = \frac{F_\phi \bar{Q}}{\bar{\phi}} e^{-i\omega\tau_c} \left[ \frac{\bar{\phi}}{\bar{m}_g} S_g c_g (p_g^+ - p_g^-) - \frac{\bar{\phi}}{\bar{m}_a} S_a c_a (p_a^+ - p_a^-) \right] \quad (2.96d)$$

The unsteady heat release due to velocity perturbations (2.94.c) can be combined with the unsteady heat release due to equivalence ratio perturbations (2.96.d). This results in the final equation for the unsteady heat release in the combustion chamber:

$$Q' = Q'_u + Q'_\phi = \frac{F_u \bar{Q}}{\bar{S}_u \rho_b c_b} e^{-i\omega\tau_f} [p_b^+ - p_b^-] + \frac{F_\phi \bar{Q}}{\bar{\phi}} e^{-i\omega\tau_c} \left[ \frac{\bar{\phi}}{\bar{m}_g} S_g c_g (p_g^+ - p_g^-) - \frac{\bar{\phi}}{\bar{m}_a} S_a c_a (p_a^+ - p_a^-) \right] \quad (2.97)$$

### 2.6.7. Flame transfer matrix

Everything is now derived to incorporate the unsteady heat release (2.97) into the flame transfer matrix. With everything written in terms of pressure fluctuations throughout the combustion system, the feedback is now integrated into the matrix term. This allows instabilities to occur as acoustic waves will directly be able to influence to unsteady heat release. For ease of notation a few parameters will be rewritten into a single parameter, see equations (2.98a-c). These terms will show a decrease in phase with increasing frequency, as is expected.

$$H_u = \bar{Q} \frac{F_u}{\bar{S}_u \rho_b c_b} \frac{\gamma - 1}{c_b^2} e^{-i\omega\tau_f} \quad (2.98a)$$

$$H_g = \bar{Q} \frac{F_\phi S_g}{\bar{m}_g c_g} \frac{\gamma - 1}{c_b^2} e^{-i\omega\tau_c} \quad (2.98b)$$

$$H_a = \bar{Q} \frac{F_\phi S_a}{\bar{m}_a c_a} \frac{\gamma - 1}{c_b^2} e^{-i\omega\tau_c} \quad (2.98c)$$

These terms will now be used to rewrite (2.81) by taking the unsteady heat release from the source term towards the left hand side of the matrix equation.

$$\begin{bmatrix} 0 & 0 & 0 & 0 & 1 & 1 & -1 & -1 \\ -H_a & H_a & H_g & -H_g & H_u + \frac{1}{\rho_b c_b} & -H_u - \frac{1}{\rho_b c_b} & -\frac{1}{\rho_f c_f} & \frac{1}{\rho_f c_f} \end{bmatrix} \cdot \begin{bmatrix} p_a^+ \\ p_a^- \\ p_g^+ \\ p_g^- \\ p_b^+ \\ p_b^- \\ p_f^+ \\ p_f^- \end{bmatrix} = \begin{bmatrix} 0 \\ 0 \end{bmatrix} \quad (2.99)$$

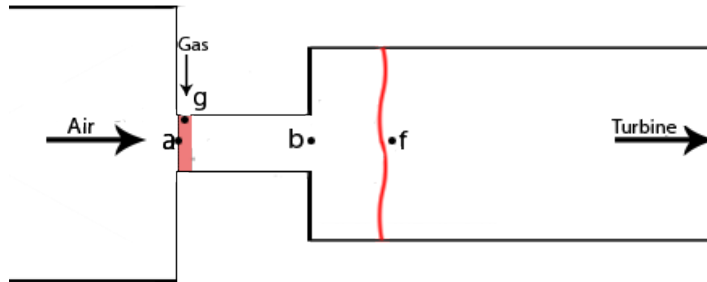


Figure 2.30: Simple combustor interpretation with nodes of perturbation; a - air; g - gas; b - burner outlet; f - downstream of flame

Assumed will be that the area between b and f, the burner outlet and the flame, will be small. In the eventual model the flame will be assumed to be conical and 'fitted' on the burner outlet. In that interpretation of the combustor system, the nodes will not be in successive order. In that case the matrix element (2.99) can just be elongated by adding zeros in between for elements that do not contribute in the flame function. This section has shown that the response of this flame transfer function is correctly reproduced if compared with the paper from Cho & Lieuwen [6]. This allows the flame transfer matrix to be combined with a simple combustor geometry to investigate the acoustic response of the system.



# 3

## Transfer matrix method validation

### 3.1. Introduction

In this chapter the transfer matrices, jump conditions and flame functions derived in the previous chapter will be validated for thermo-acoustic systems, an acoustic case of a clarinet is validated in Appendix D. First a Rijke tube will be analysed, this is a duct of constant cross-sectional area fitted with a heating gauze. The Rijke tube is a classical example of the instability of a system due to heat addition. The final model will be that of a simple combustor from Dowling & Stow [12], this will be used to validate the implementation of a flame transfer matrix. The final section will talk about the reflection factor of the burner and flame system, this reflection factor will be calculated and used as input into the combustion chamber and can be analyzed to determine the amplification or damping at all frequencies.

### 3.2. Thermo-acoustics of a Rijke Tube

#### 3.2.1. Introduction

In this section the thermo-acoustics of a Rijke tube will be discussed. The theory of the Rijke tube is described by Heckl [16]. The Rijke tube is a straight and open-ended tube, where a heat source is present, in this case the heat will be delivered by a heating gauze. The heat release from the gauze to the air is unsteady, which allows a coupling between the heat release and the pressure and thus acoustic oscillations can build up and drive the system to instability [16].

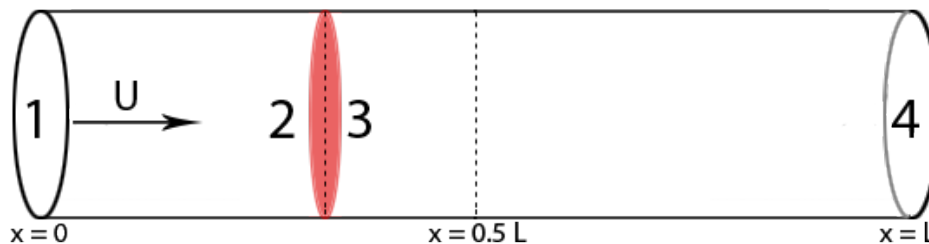


Figure 3.1: Rijke tube geometry; heat release zone in upstream half of the cylindrical duct

#### 3.2.2. Model set-up

For the Rijke tube to be unstable, there are 2 requirements that need to be fulfilled [16].

1. The heating gauze must be present in the upstream half of the tube. Otherwise the phase relation between heat release and pressure will not drive the system to instability.
2. Enough heat must be supplied to overcome the damping that will be present in the system.

In this case the Rijke tube will be modelled horizontally, with a flow of air coming in from the upstream side of the system. The unsteady heat release,  $Q'$ , at the gauze will be written in terms of a transfer function that relates it to the velocity fluctuation,  $u'$ , at the gauze.

$$Q' = \beta u'(t - \tau) \quad (3.1)$$

Where  $\beta$  is given as a function by Heckl [16]:

$$\beta = L_w(T_w - T) \sqrt{(\pi \kappa c_v \bar{\rho} / \bar{u})(d/2)} \quad (3.2)$$

This function for  $\beta$  is based on King's Law [20], which is a function that is derived for the heat transfer from a cylindrical hot wire to a perpendicular flow. It is assumed that this relation holds in the case of the heating gauze present in the Rijke tube [16]. So this function  $\beta$  is just a function for the heat transfer from the heating gauze to the air in the tube and will result in a change in heat release when the velocity fluctuation at the heating gauze fluctuates. Where  $L_w$  is the total length of the wires in the heating gauze,  $T_w$  is the temperature of the heating gauze,  $T$  is the temperature of the incoming air,  $\kappa$  is the heat conductivity of air,  $c_v$  is the specific heat of air per unit mass at constant volume,  $\bar{\rho}$  is the mean density of the air and  $d$  is the diameter of the wire. This can be rewritten as a transfer function that can be incorporated into the transfer matrix model [21]:

$$H_{gauze}(\omega) = \frac{\gamma - 1}{c^2 \rho S} \beta e^{-i\omega\tau} \quad (3.3)$$

With this transfer function that Rijke tube can be easily described in a matrix. It will consist of an upstream and downstream boundary condition, both open ends (2.63). There will be a duct upstream of the heating gauze and downstream of the heating gauze (2.30), these are elements I and III in figure 3.2. The matrix for the heating gauze (3.4), element II, will be similar to the flame transfer matrices derived in Chapter 2. In this case assumed will be that the density does not change over the heating gauze and that pressure remains constant. This assumption is valid as the heating gauze is very thin and the static pressure drop across the gauze is small [21].

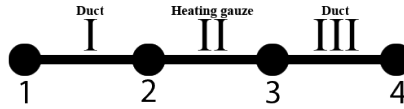


Figure 3.2: Rijke tube network model

Parameter	Notation	Value
Speed of sound	$c$	358 [m s <sup>-1</sup> ]
Upstream duct length	$L_I$	0.3 [m]
Downstream duct length	$L_{II}$	0.7 [m]
Duct cross sectional area	$S$	0.00156 [m <sup>2</sup> ]
Specific heat ratio	$\gamma$	1.4 [-]
Time-delay	$\tau$	0.15 [ms]
Rijke tube function	$\beta$	187 [kg m s <sup>-2</sup> ]

Table 3.1: Rijke tube parameters from Heckl [16]

$$\begin{bmatrix} 1 & 1 & 0 & 0 & 0 & 0 & 0 & 0 \\ e^{-ik^+L_I} & 0 & -1 & 0 & 0 & 0 & 0 & 0 \\ 0 & e^{ik^-L_I} & 0 & -1 & 0 & 0 & 0 & 0 \\ 0 & 0 & 1 & 1 & -1 & -1 & 0 & 0 \\ 0 & 0 & -1 - H_{gauze} & 1 + H_{gauze} & 1 & -1 & 0 & 0 \\ 0 & 0 & 0 & 0 & e^{-ik^+L_{II}} & 0 & -1 & 0 \\ 0 & 0 & 0 & 0 & 0 & e^{ik^-L_{II}} & 0 & -1 \\ 0 & 0 & 0 & 0 & 0 & 0 & 1 & 1 \end{bmatrix} \cdot \begin{bmatrix} p_1^+ \\ p_1^- \\ p_2^+ \\ p_2^- \\ p_3^+ \\ p_3^- \\ p_4^+ \\ p_4^- \end{bmatrix} = [\mathbf{s}] \quad (3.4)$$

### 3.2.3. Rijke tube stability

By solving the matrix system (3.4) for the determinant to equal zero, complex eigenfrequencies will be found. For the case without unsteady heat release, the eigenfrequencies of the duct are found. These are 179, 358, 537, 716 and 895 Hz, and are as expected. These frequencies do not have an imaginary part, as there is no unsteady heat release present. The eigenfrequency at 179 Hz is the fundamental frequency, which has a wave-length of twice the duct size. This frequency can also be calculated by hand using  $f = c/\lambda = c/2L = 358/2 = 179\text{ Hz}$ . When  $\beta$  is changed, the unsteady heat release becomes active. For this a value for  $\beta$  of  $187[\text{kg m s}^{-2}]$  is used, which is the value mentioned in the paper by Heckl [16].

The results of the modelled Rijke tube will be compared with the result of Heckl [16], where the focus will be on the fundamental frequency. Expected is that the fundamental frequency of 179 Hz will shift slightly due to the unsteady heat release. With the heating gauze in the first half of the duct the phase relation between heat release and pressure should drive the system to show instability, which means its growth rate should be negative. A multitude of frequencies and growth rates are mentioned by Heckl [16] for different sorts of models, either including or excluding damping coefficients. To get the results from Heckl [16], the matrix system that was provided in the paper by Heckl [16] was implemented with the provided parameters, which allows the systems to be compared.

Results from	Frequency	Growth rate
Model	186.4 [Hz]	-1.15
Heckl [16]	186.4 [Hz]	-1.15
Bijlsma [4]	186.4 [Hz]	-1.15
Klein [21]	186.4 [Hz]	-7.2

Table 3.2: Fundamental frequency and growth rate of the Rijke tube from different papers

Results of 4 different sources are tabulated in table 3.2. The results are all for systems where no damping is included, so the duct ends are modelled as open ends with no change in reflection factor. The results of the model, Heckl's model [16] and Bijlsma's [4] are all equal to one another. The results from Klein [21] have a far more unstable frequency for the case without damping. When he includes damping due to wall friction, the growth rate goes to -1.3, which is closer to the other results. In the paper by Klein [21] it is mentioned that  $\beta = 286.7\text{ kg} \cdot \text{m} \cdot \text{s}^{-2}$ , which is larger than used in the other results, which could explain the increased instability. When Klein's [21] transfer matrix model is implemented with the parameters presented in table 3.1 the results are equal to the modelled results.

This validates the behaviour of the Rijke tube and shows that, if the phase relation between unsteady heat release and acoustics are correct, some frequencies will turn unstable. This system of two ducts with a heating gauze can now be expanded to a more complex geometry with an active source of sound due to unsteady heat release by a flame.

### 3.3. Simple combustor model

#### 3.3.1. Introduction

To show the influence of the flame transfer function an example for a simple combustor geometry and a basic flame function will be described, following the method used by Dowling & Stow [12]. The modelled results will be compared with the results from Dowling & Stow [12]. This chapter will focus on the flame behaviour and is used to validate the implementation of a basic flame transfer function.

#### 3.3.2. Combustor geometry

This example will follow the method used by A.P. Dowling and S.R. Stow (2003) [12]. A simple combustor model is used, as shown in figure 3.3. It consists of a plenum, denoted by 1, a premix duct, denoted by 2, and a combustion chamber, denoted by 3.

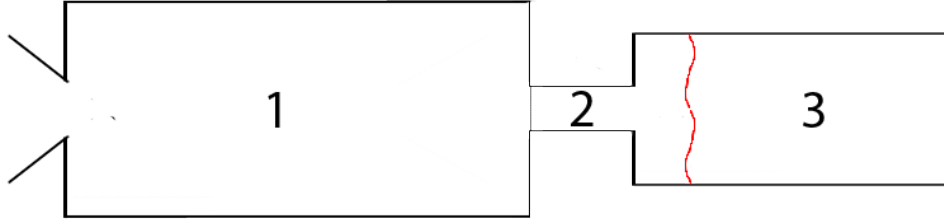


Figure 3.3: Simple combustor model [12]

$$\frac{Q'}{\bar{Q}} = -k \frac{m'_i}{\bar{m}_i} e^{-i\omega\tau} \quad (3.5)$$

A simple flame transfer function, equation (3.5), will be used.  $Q'$  denotes the unsteady heat release that occurs at the flame front during combustion. This unsteady heat release is a result of fluctuating conditions upstream of the flame, which arrive after a time delay ( $\tau$ ) at the flame. This transfer function relates the fluctuating heat release at the flame front to a fluctuation of mass,  $m'_i$ . The term  $m'_i$  denotes a fluctuation of mass flow occurring at the end of the premix duct, which is the burner outlet. This fluctuation of mass flow is convected by the mean flow velocity to the flame front. It will arrive after a time delay ( $\tau$ ) at the flame front, after which it will result in a fluctuation of the heat release. To use this condition in the transfer matrix element, the mass flow fluctuation needs to be rewritten in terms of pressure fluctuations at the burner outlet.

$$m'_i = \rho_1 S_1 u'_i \quad (3.6a)$$

$$m'_i = \frac{S_1}{c_1} (p_i^+ - p_i^-) \quad (3.6b)$$

$u'_i$  denotes the velocity fluctuations at the burner outlet, which can be rewritten in terms of the pressure fluctuations, which allows the flame function to be used in the transfer matrix model.

#### 3.3.3. Acoustic combustor model stability

For  $k = 0$  in equation (3.5), all eigenfrequencies that are found should be stable as there is no unsteady heat release [12], this is a purely acoustic system. In table 3.3 the eigenfrequencies from Dowling [12] are compared with the eigenfrequencies that are calculated using the constructed model. The real part of the eigenfrequencies are slightly different, which can be the result of assumed process parameters. Not all important parameters are mentioned in the paper by Dowling [12]. Assumptions have been made for the speed of sound, the density of the flow and the flow velocities. These assumptions have a direct effect on the jump conditions at the area discontinuities and also on the wave propagation through the cylindrical duct elements. These unknown parameters will also have an influence on the choked inlet condition, which is a very important parameter for the stability of the system. Besides the unknown process parameters, it is also unknown at what point and Mach number Dowling has evaluated the choked nozzle inlet. Dowling's [12] results have far more stable frequencies as in the modelled system. This indicates that there is more damping present in the acoustic system modelled by Dowling. Note that the growth rates by Dowling are plotted as their negative value, so

in this case a positive growth rate indicates an unstable system while a negative growth rate indicates a stable system.

Dowling & Stow: $k = 0$ [12]	Modelled: $k = 0$
30 - 105i	32 - 14.61i
110 - 25i	115 - 4.03i
203 - 10i	206 - 0.37i
289 - 52i	285 - 5.88i
337 - 120i	337 - 11.79i
416 - 30i	421 - 3.99i
511 - 10i	518 - 1.72i

Table 3.3: Resonant modes from Dowling & Stow [12] compared with modelled resonant modes, for  $k = 0$

Dowling mentions the used choked inlet condition in her paper [12], which is the same equation that is used in this model, equation (2.67). When the equation is evaluated in terms of up- and downstream travelling pressure waves, one can determine the damping as this can be rewritten in terms of an equation  $Xp_i^+ = Yp_i^-$ , where  $X$  and  $Y$  are constants that are determined from flow parameters in the choked inlet condition. In this case  $Y/X$  can be interpreted as a reflection factor at the choked inlet. A value below 1 will result in damping, while a value above 1 will result in amplification. With the choked inlet condition from Dowling [12] and the assumed conditions the reflection factor is 0.985. This means that there is not much damping at the choked inlet, which partly explains the disparity in growth rates. The reflection factor at the choked inlet is decreased, which results in figure (3.4). The reflection factor is severely decreased to only reflect 10% of the wave strength travelling upstream towards the choked inlet nozzle. All growth rates have decreased, which means that stability of the system has increased which is as expected with an increase in damping. There is still a difference in the growth rates, even with increased damping. This suggests that another aspect of the acoustic system used in the paper by Dowling [12] results in more damping, which is most likely to be found in the area changes. The fact that the system by Dowling [12] is still much more stable, even though just 10% of the pressure wave is reflected back into the system, suggests that the growth rates in the paper by Dowling [12] might not be correct. Since the focus of this chapter is on the flame response, the acoustic system is not the main focus. As long as the flame responds in the way that is expected and in agreement with the flame response from the paper by Dowling [12] the flame transfer matrix is assumed to be validated. The initial system will be the one that remains to be used for the model, this is the system without an increase in damping.

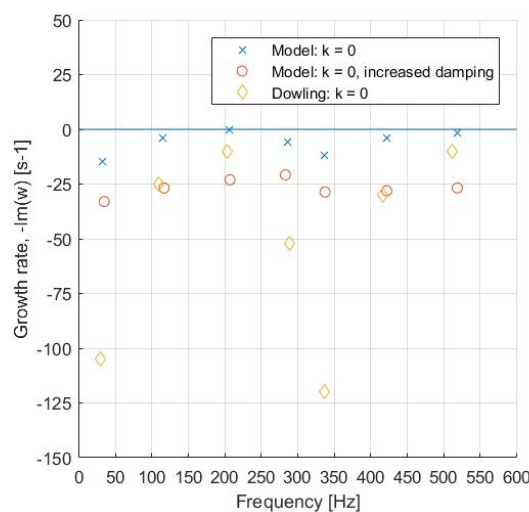


Figure 3.4: Stability plot from [12] compared with modelled stability

### 3.3.4. Thermo-acoustic combustor model stability

If  $k$  is changed to 1, unsteady heat release will be present in the combustion chamber. This will drive some of the resonant modes from table 3.3 to become unstable, as well as slightly shift their resonance frequency. The unsteady heat release will also add new resonant modes, which are associated with the flame transfer function [12]. These resonance frequencies corresponding to the flame function are related to the time delay,  $\tau$ , which is the convection time for the fluctuation at the burner outlet to reach the flame front. The resonance frequencies will approximately be  $\frac{1}{\tau}$ ,  $\frac{2}{\tau}$ ,  $\frac{3}{\tau}$  etc. [12]. This means that the expectation is that there will be unstable frequencies around 167 Hz, 333 Hz and 500 Hz.

In figure 3.5, the stability plot is shown. On the y-axis the growth rate is plotted, which is (in this case) the negative value of the imaginary part of the resonance frequency. A positive value on this axis means that the frequency is unstable, while a negative value indicates a stable frequency. On the x-axis the real part of the resonance frequency is plotted.

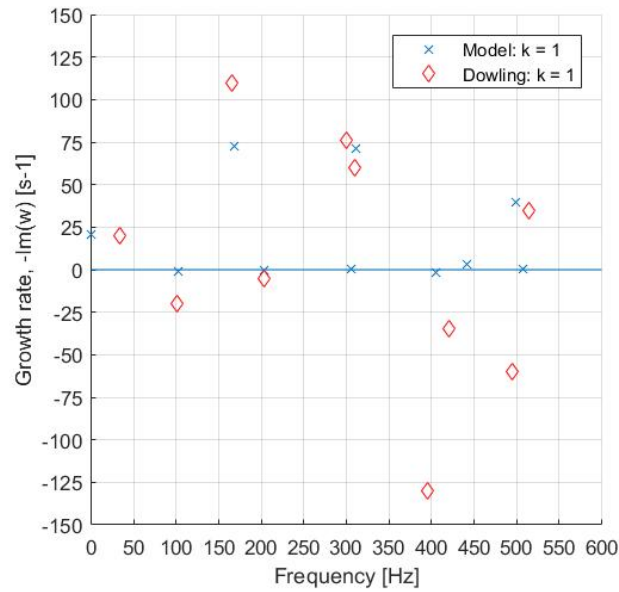


Figure 3.5: Stability plot from [12] compared with modelled stability

Dowling & Stow: $k = 1$ [12]	Modelled: $k = 1$
$165 + 110i$	$168 + 72i$
$300 + 76i$	$306 - 0.10i$
$310 + 60i$	$310 + 71i$
$515 + 35i$	$498 + 40i$

Table 3.4: Flame resonant modes from Dowling & Stow [12] compared with modelled flame resonant resonant modes

A deeper look will be taken into the resonance frequencies associated with the flame behaviour, as the acoustic system frequencies have been shown to differ in the previous section. The frequencies found from the acoustic system might shift a bit and their growth rates are expected to also slightly change, but the flame resonance frequencies will be most important. Comparing the results from Dowling & Stow with the modelled results for the case with unsteady heat release, some differences can be seen, see table 3.4. For both system there are unstable frequencies around 167 Hz, 333 Hz and 500 Hz. One of the frequencies in the modelled results around 300 Hz does not turn unstable, this is a wave mode that is associated with the plenum of the combustion system. Assumed here is that due to the different acoustic system response, this term remains stable instead of turning unstable in the case for the paper by Dowling [12].

The other frequencies do show up when unsteady heat release is included and are not present for the cold flow case, albeit that their growth rates do not match. This can also be due to the disparity in the acoustic cold flow results, but can also be due to the magnitude of the flame transfer function. The mean heat released

rate used in the flame transfer function is not clear from the paper by Dowling [12], this is the only assumption that has to be made for the unsteady heat release case. It is however an important parameter as it directly relates to the fluctuation of the heat release rate. If this mean heat release rate is lowered as opposed to the assumption, the growth rates of the frequencies decrease. While if the mean heat release rate is increased, the growth rates of the frequencies also increase, meaning the system gets more unstable. This is also something to be expected, as an increase in mean heat release means an increase in unsteady heat release, which should provide higher pressure waves and thus more instability.

The most important thing to show from this example is the fact that the system does respond to an unsteady heat release as expected. Albeit that the acoustic response is not the exact response as from Dowling & Stow [12], the flame behaviour, and thus thermo-acoustic response, is correct. The disparity in results can be appointed to the acoustic model, without unsteady heat release, having different growth rates due to a difference in acoustic system damping. As stated before, that is most likely due to different inlet conditions and/or flow conditions. Taking unsteady heat release into account, it does not show the exact quantitative behaviour compared with the results from Dowling [12], but it does show qualitative behaviour that is comparable to that from Dowling [12]. New resonance frequencies show up due to the flame behaviour, which follow a relation with the convective time-delay ( $\frac{1}{\tau}$  etc.) that was found by Dowling [12]. With these results, the conclusion can be made that the implementation of this basic flame transfer function is correct, which allows more complicated and elaborate flame transfer functions to be used.

### 3.4. Reflection factor validation

#### 3.4.1. Introduction

To reduce computational effort, a reflection factor will be used as input into the combustion chamber. This reflection factor will be calculated from the burner system up to and including the flame. This reflection factor can be used as a boundary just downstream of the flame and will incorporate the (thermo-)acoustic behaviour of the upstream combustion system. This reduces the matrix model to a system of 6x6 for a single burner fitted into a combustion chamber. From here on out the flame transfer function by Cho & Lieuwen [6] will be used.

#### 3.4.2. Methodology

To calculate this reflection factor the combustion system will be solved in terms of a single pressure wave amplitude, in this case the upstream travelling wave after the flame. The pressure waves after the flame can then be used as boundary condition in the eventual system. To validate the method of the reflection factor calculation, the simple combustor model from Dowling & Stow [12] with the Cho & Lieuwen [6] FTF will be used, see figure 3.6. After the reflection factor is calculated, this will be used as input boundary condition in the one-dimensional combustion chamber, see figure 3.7.

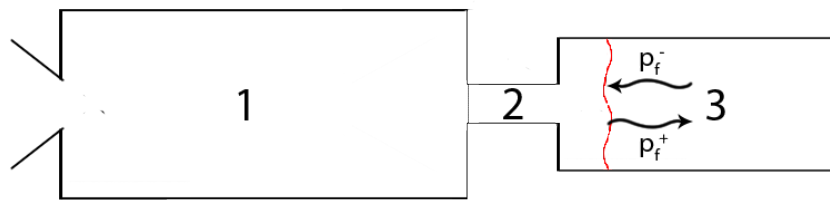


Figure 3.6: Simple combustor model from Dowling & Stow [12] with acoustic waves at flame front

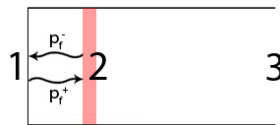


Figure 3.7: Reflection factor used as input in combustion chamber; 1 left boundary; 2 passive sound source; 3 right boundary

All coefficients in the system that are related to the upstream travelling wave after the flame,  $p_f^-$ , are transferred to the RHS of the system of equations. This will leave a system of 13 equations and 13 unknowns, written in terms of  $p_f^-$ , which allows the system to be solved, see equations (3.7a-3.7d). This way of solving does not take into account the influence of the combustion system downstream of the flame, that way the reflection factor can be used as input in any type of combustion system.

$$[A] \cdot \begin{bmatrix} p_1^+ \\ p_1^- \\ \vdots \\ p_6^+ \\ p_6^- \\ p_f^+ \\ p_f^- \end{bmatrix} = \mathbf{0} \quad (3.7a)$$

$$[A] \cdot \begin{bmatrix} p_1^+ \\ p_1^- \\ \vdots \\ p_6^+ \\ p_6^- \\ p_f^+ \end{bmatrix} = \begin{bmatrix} A_{1,n} \\ A_{2,n} \\ \vdots \\ A_{n-2,n} \\ A_{n-1,n} \\ A_{n,n} \end{bmatrix} \cdot p_f^- \quad (3.7b)$$

$$\begin{bmatrix} p_1^+ \\ p_1^- \\ \vdots \\ p_6^+ \\ p_6^- \\ p_f^+ \end{bmatrix} = [A]^{-1} \begin{bmatrix} A_{1,n} \\ A_{2,n} \\ \vdots \\ A_{n-2,n} \\ A_{n-1,n} \\ A_{n,n} \end{bmatrix} \cdot p_f^- \quad (3.7c)$$

$$\begin{bmatrix} p_1^+ \\ p_1^- \\ \vdots \\ p_6^+ \\ p_6^- \\ p_f^+ \end{bmatrix} = \begin{bmatrix} R_1^+ \\ R_1^- \\ \vdots \\ R_6^+ \\ R_6^- \\ R_f^+ \end{bmatrix} \cdot p_f^- \quad (3.7d)$$

### 3.4.3. Magnitude reflection factor

The behaviour of the flame and the system upstream of the flame can be plotted by calculating the magnitude of the reflection factor. The magnitude of this factor will indicate if an upstream travelling pressure wave gets either amplified or damped by the burner system. A reflection factor above 1 will mean that a upstream travelling pressure wave will get amplified and in the case it's amplified more then it is damped while travelling downstream this frequency will turn unstable. The reflection factor will be calculated for a geometry as presented in the previous section and a fuel mixture with an equivalence ratio of 0.5.

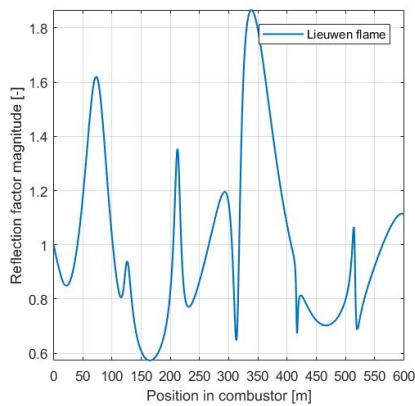


Figure 3.8: Flame and burner system reflection factor; Lieuwen [6] flame model

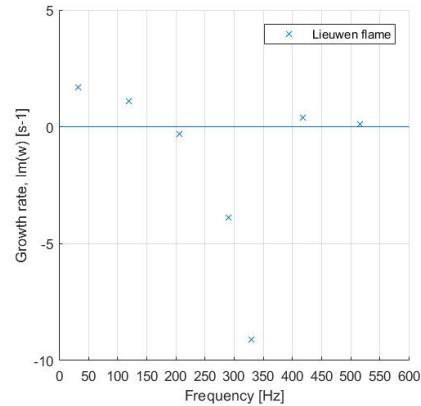


Figure 3.9: Stability plot; Lieuwen [6] flame model; Dowling [12] combustor model

Figure 3.8 shows that the Lieuwen flame model has a high reflection factor around 75 Hz, while there is no unstable frequency found in that range with the stability plot, figure 3.9. The frequencies in the stability plot are eigenfrequencies of the combustion system, if no eigenfrequency is found this means that there are no pressure waves in the frequency range and no instability can occur. Unstable resonance frequencies around 200 Hz, 290 Hz and 325 Hz were found in the stability diagram. These are all frequencies which correspond to a reflection factor higher than 1, which means the pressure wave at this frequency is amplified. A higher reflection factor magnitude results in a lower, and thus more unstable, growth rate. Note that from here on out, a negative growth rate once again means that the frequency is unstable.

#### 3.4.4. Time delay influence

Dowling & Stow [12] stated that the time delay closely influenced the resonance frequencies of the flame. Since the FTF used by Lieuwen is frequency dependent and two different time delays are present, it does not seem to follow the relation  $\frac{1}{\tau}$  etc. that was mentioned in [12]. To check the influence of the time delay, the convective time-delay of the mass fluctuation at the burner outlet is changed.

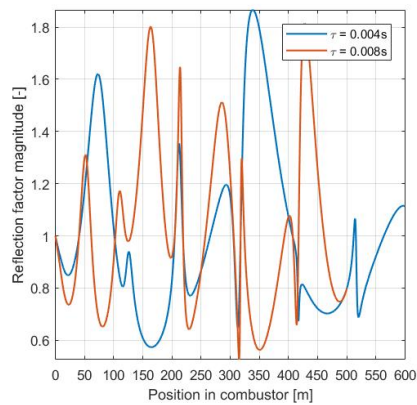


Figure 3.10: Influence of convective time-delay from burner outlet on reflection factor magnitude

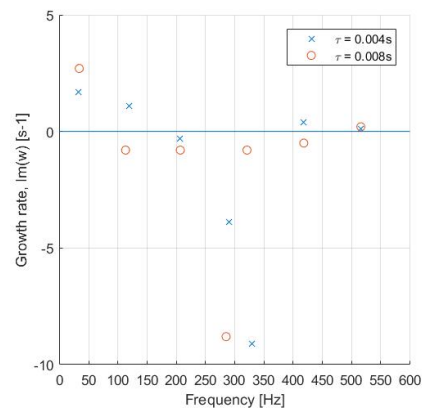


Figure 3.11: Influence of convective time-delay from burner outlet on stability plot

One can see that the response of the system changes for when the time-delay is changed, see figure 3.10. The frequencies of peak reflection factor magnitudes are changed, which seems to turn some frequencies unstable as shown in the stability plot 3.11. It was shown previously that the combustion system had an eigenfrequency in the purely acoustic system at around 110 Hz. It was also shown that these frequencies do not shift all too much when the unsteady heat release is taken into account. For the initial time-delay case with  $\tau = 0.004\text{ s}$  the frequency at around 110 Hz is stable, as it can also be seen that the reflection magnitude in that case is below 1. For a shift in time-delay towards  $\tau = 0.008\text{ s}$ , a peak in reflection magnitude is shown around 110 Hz, which in turn also shows an unstable frequency in the stability plot. This means that if the eigenfrequencies of a system are known, the reflection factor can also be used to determine the combustion system stability. It also means that if there is large amplification around a frequency that is not a eigenfrequency of the combustion system, it will not result in instabilities.

### 3.4.5. Reflection factor as input

The reflection factor will be used as input in to the combustion chamber, as this will reduce the computational requirements for the final burner combustion model. The reflection factor system will be modelled as seen in figure 3.7 and compared with the pressure response of the full simple combustor model, figure 3.6. The reflection factor system will only consist of an inlet boundary condition, which is a function of the reflection factor, a passive source of sound, an acoustic duct and an outlet boundary condition, which is an open outlet. The passive source of sound will have an arbitrarily chosen source term  $s$ , which will influence only the absolute value of the pressure response.

$$\begin{bmatrix} 1 & -R_f^+ & 0 & 0 & 0 & 0 \\ 1 & 1 & -1 & -1 & 0 & 0 \\ \frac{1}{\rho_1 c_1} & -\frac{1}{\rho_1 c_1} & -\frac{1}{\rho_2 c_2} & \frac{1}{\rho_2 c_2} & 0 & 0 \\ 0 & 0 & e^{-ik^+ L_{cc}} & 0 & -1 & 0 \\ 0 & 0 & 0 & e^{ik^- L_{cc}} & 0 & 1 \\ 0 & 0 & 0 & 0 & 1 & -1 \end{bmatrix} \cdot \begin{bmatrix} p_1^+ \\ p_1^- \\ p_2^+ \\ p_2^- \\ p_3^+ \\ p_3^- \end{bmatrix} = \begin{bmatrix} 0 \\ 0 \\ s \\ 0 \\ 0 \\ 0 \end{bmatrix} \quad (3.8)$$

Below the results of the full combustor model and the model using the reflection factor as input are shown. Figures 3.12 and 3.13 show the pressure spectrum of both models at a distance of 0.2m in the combustion chamber, which has a total length of 1m. Both systems show the exact same response. One can thus conclude that the combustor system can also be modelled by calculating a reflection factor just downstream of the flame and using this as input for the combustion chamber with a passive source of sound.

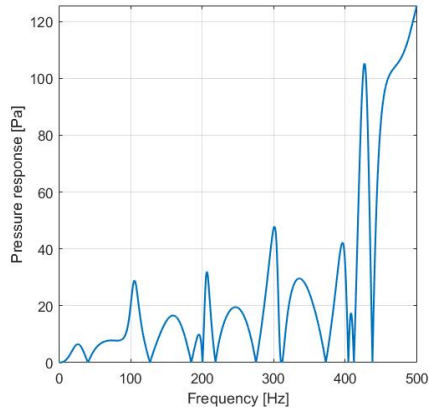


Figure 3.12: Full system model pressure spectrum at 0.2 m in combustion chamber

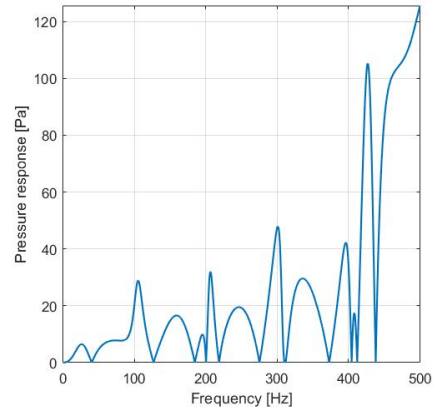


Figure 3.13: Reflection factor model pressure spectrum at 0.2m in combustion chamber



# 4

## Vattenfall operated SGT5-4000F plants

This chapter will discuss the SGT5-4000F gas turbine. A general description of the gas turbine and its operation will be provided. Further information about the combustion stability system will be discussed as well as measures taken to prevent or limit combustion instabilities.

### 4.1. SGT5-4000F combined cycle power plant

Vattenfall operates two SGT5-4000F combined cycle power plants in the district of Amsterdam. They are called Hemweg 9, which is referred to as HW09, and Diemen 34, which is referred to as DM34. Both of these plants are able to provide around 300 MW in single cycle gas turbine mode. They are however equipped with a steam turbine which allows them to provide a total power output around 420 MW each, with an efficiency around 57 %. The gas turbine cycle consists of a 15 stage axial flow compressor and a 4 stage air-cooled turbine. The compressor and turbine are connected to a 24 hybrid burner annular combustion chamber, fully fitted with ceramic tiles acting as a heat shield.

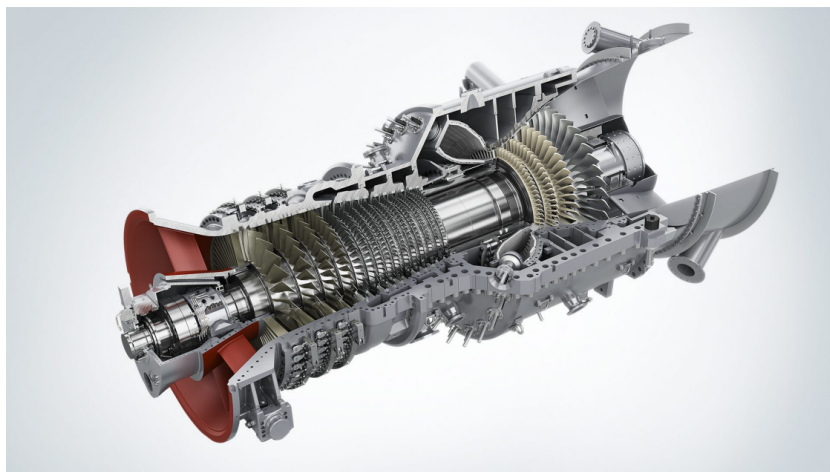


Figure 4.1: SGT5-4000F Gas turbine

<https://new.siemens.com/global/en/products/energy/power-generation/gas-turbines/sgt5-4000f.html>

#### 4.1.1. Annular hybrid burner ring

The SGT5-4000F combustion chamber has an annular combustion chamber, see figure 4.2. This combustion chamber is equipped with a hybrid burner ring (HBR), consisting of 24 hybrid burners. This hybrid burner, figure 4.3, has been developed for premix combustion in gas turbines. Lean premixed combustion is used to limit  $\text{NO}_x$  emissions, but it also has a few drawbacks. It has a limited load range, possibilities of autoignition or flame flashback and, the purpose of this thesis, it is susceptible to dynamic combustion instabilities [42].

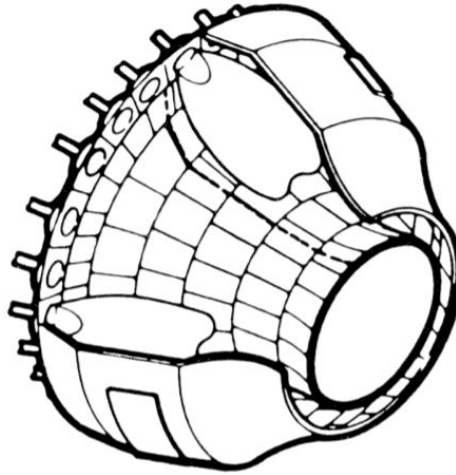


Figure 4.2: Sketch of the SGT5-4000F annular combustion chamber [17]

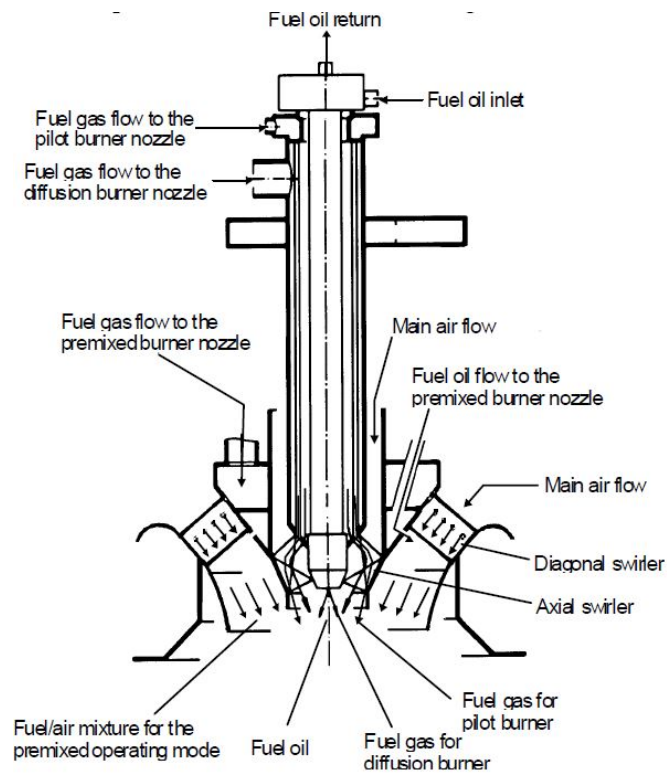


Figure 4.3: Hybrid burner layout - without CBO [42]

There have been quite some design changes to get to the final burner design, most of these changes were focused on the premix part, which can be seen in figure 4.4. The premix gas is now distributed through the swirler vanes, which minimizes the chance of auto-ignition as well as eliminating the re-circulation in the wake of the previous gas distribution pipes [35]. The geometry of hub and tip are selected so that no flow separation happens at the hub, this results in a premix flow that is as stable as possible and reduces the possibility or severity of acoustic pulsations [35]. The flow path of the premix gas passage is designed such that the residence time is as low as possible, which minimizes the risk of auto-ignition [35].

#### 4.1.2. Cylindrical burner outlet

Not all hybrid burners in the annular combustion chamber are exactly the same. 4 of the 24 burners are fitted with a cylindrical burner outlet (CBO), as can be seen in figure 4.4. Equipping some burners with an extension changes the behaviour of that burner to upstream travelling acoustics. It also changes the flowfield from burner outlet to flame, and increases the convective time-delay from mixing zone to flame front. It will also change the convective time-delay from burner outlet to flame zone, as the flame shape will also change. The influence of the CBO on the flowfield out of the burner can be seen in figure 4.6. The flowfield out of the burner without a CBO is much wider, while with a CBO the flowfield seems more fixed and smaller. Further influence of the CBO will be discussed later in this chapter and analysed in chapter 7.

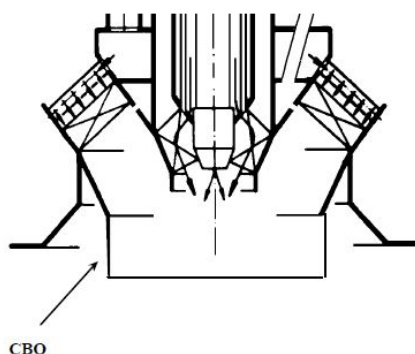


Figure 4.4: CBO fitted to the final hybrid burner [42]

## 4.2. Combustion monitoring at Vattenfalls gas turbines

Pressure sensors and acceleration sensors are fitted in the annular combustion chamber at certain burner outlets. These sensors will monitor the pressure amplitudes and accelerations in certain frequency bands, when these values get too high the stability margin controller can step in, which will be explained in the next section. The harmonic frequencies of the annular combustion chamber are known from internal documents. They have also been approximated by using equation (D.1) and making an assumption about the speed of sound in the combustion chamber and the circumferential length of the annular combustion chamber. These frequencies are also mentioned further as respectively FB2, FB5 and FB7. The expectation will be that these frequencies will show the largest pressure amplitudes when the pressure spectra are calculated, as these will resonate inside the combustion chamber. Figure 4.5 shows how the harmonic wave modes fit inside the annular combustion chamber.

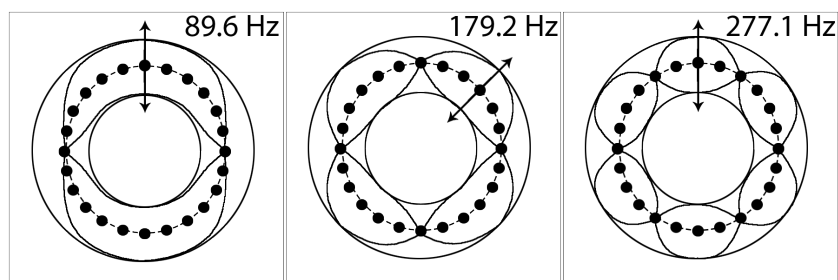


Figure 4.5: Harmonic frequencies of annular combustion chamber

At base load operation, the most critical frequency is mentioned to be at 120 Hz and is called FB3. It is not expected that this frequency will show resonance in the combustion chamber, as a wave at this frequency does not fit in the combustion chamber. It is assumed that this wave resonates in another part of the combustion system, but as not the entire combustion system is taken into account this will most likely not be visible. The amplification of this frequency can be analysed, as the reflection factor of the flame does not take the combustion chamber into account. An increase or decrease in reflection factor magnitude due to a change in operational conditions will give insight to the increase or decrease of the stability of this frequency band. The other monitored frequency bands are tabulated in table 4.1 and are not the main focus of this thesis.

Frequency band	Frequency range	Remarks
FB1	5 - 30 Hz	-
FB2	80 - 100 Hz	First harmonic frequency
FB3	105 - 125 Hz	Critical at base load
FB4	130 - 145 Hz	-
FB5	150 - 180 Hz	Second harmonic frequency
FB6	210 - 235 Hz	Critical at low part load
FB7	250 - 280 Hz	Third harmonic frequency; critical at low part load
FB8	315 - 355 Hz	-

Table 4.1: Monitored frequency bands by stability margin controller

#### 4.2.1. Stability margin controller

The gas turbines at Vattenfall are equipped with a combustion dynamics intervention system, which is also called the Stability Margin Controller (SMC). Pressure sensors and acceleration sensors are fitted in the annular combustion chamber at certain burner outlets. These sensors will monitor the pressure amplitudes and accelerations in certain frequency bands. When these values get too high, the intervention system steps in. There are three types of signals the intervention system makes use of:

$$|p'_{FB\#}| > LIMIT\# \quad (4.1a)$$

$$g_{FB\#} > LIMIT\# \quad (4.1b)$$

$$LN2\# = \ln \frac{avg(p'_{FB2})}{avg(p'_{FB\#})} > LIMIT\# \quad (4.1c)$$

For each signal there are 6 types of limit values. 3 limit values for base load operation and 3 limit values for part load operation. Equation (4.1a) is used when the maximum pressure amplitude crosses the limit value. Pressure amplitudes are measured in 8 different frequency bands (FB), for example FB2 ranges between 80-100 Hz. If the amplitude in FB2 crosses a certain limit value, the intervention system steps in.

Measurement (4.1b) is used when accelerations in a certain frequency band are getting too high. If this measurement reaches its maximum limit value, a couple of g acceleration, a combustion chamber inspection is required. However, before it reaches that value, intervention should happen.

The last measurement (4.1c) makes use of a ratio between pressure amplitudes in two frequency bands. It always compares FB2 with the pressure amplitudes FB3, FB4 or FB5. For stable combustion FB2 needs to remain the dominant amplitude. This means that it sometimes is better to increase the pressure amplitude in this frequency band to reduce the risk of humming intervention. If this value becomes too low the stability margin controller steps in. The reasoning for dominant 90 Hz humming providing stability can be explained from the acoustic equations. The acoustic equations are solved in terms of complex pressure amplitudes for up- and downstream travelling pressure waves. These amplitudes are calculated from the energy added to the combustion system, which is the unsteady heat release. If the unsteady heat release remains equal, an equal amount of energy is added towards the combustion system. If more of this energy is concentrated in the 90 Hz area, this means less energy is available to drive acoustic pressure waves at other frequency areas. The intervention can happen in a couple of ways. For one, it can insert more pilot gas. This pilot gas is a rich gas mixture and will help stabilize the combustion in the system. It usually is combined with a reduction in premix gas and thus also a gas turbine load reduction. A reduction of turbine outlet temperature (OTC) can also be an intervention measure. This is usually done by reducing the amount of premix gas that flows towards the combustion chamber, and is thus also a reduction in gas turbine load.

### 4.3. Combustion instabilities prevention

It is very difficult to fully prevent combustion dynamics in these current types of gas turbines. Due to the lean operation to reduce  $\text{NO}_x$  emissions, the combustion is inherently not ideal. It is however, with good understanding of the dynamics of this phenomenon, possible to limit the occurrence of these instabilities. Siemens has used a couple of ways to limit the occurrence of combustion dynamics, these relations will be used to test the validity of the model in the chapter about case studies. The influence of fuel temperature, amount of premix gas nozzles and cylindrical burner outlet are of interest.

#### 4.3.1. Influence of fuel preheating temperature

By analyzing process data from the Hemweg 09 (HW09), it was found that the fuel preheating temperature has a big influence on the humming in FB2. A lower preheating temperature will have a higher pressure amplitude in FB2. As said before, this may seem counter-intuitively, but it was acknowledged by Siemens that they like to keep FB2 as the dominant frequency. A lot of interventions in the HW09 happen when (4.1c) crosses its limit value. Increasing the pressure amplitude in FB2 by lowering the fuel temperature is thus an effective way to keep (4.1c) away from its limit value.

A change in the fuel temperature will most likely influence just the dynamics of the fuel flow into the mixing chamber. The air is supplied in a vastly larger amount and at a higher temperature, so it should not result in a significant increase in combustion chamber temperatures. The fuel temperature will have a direct effect on the fuel density, and thus fuel velocity, that flows out of the premix gas nozzles. Most problems happen when the gas turbine operates at maximum load and at high fuel temperature. In these operating conditions, the fuel velocity will be the highest. The fuel velocity will be of influence on the pressure drop over the gas nozzles as well as on the mixing dynamics with the air flow.

A (too) high fuel velocity can result in imperfect mixing conditions. Combustion of an imperfect mixture at the flame front can result in an uneven temperature distribution downstream of the flame. This will result in fluctuations of the hot gas temperature, which are called entropy waves [34]. These temperature uniformities will travel towards the choked inlet of the turbine where they can result in pressure waves that will travel upstream from turbine inlet towards the flame. This effect can couple with the combustion acoustics and can also drive combustion instabilities. The thermo-acoustic model will assume homogeneous mixing, so this effect will not be taken into account.

The pressure drop over the nozzles can make the fuel flow more or less susceptible to travelling pressure waves. If the pressure drop over the fuel nozzles is lower, the fuel flow will be more susceptible to upstream travelling pressure waves [18]. This effect is taken into account in the thermo-acoustic model.

#### 4.3.2. Influence of premix gas nozzles

While the change in fuel preheating temperature is one that can be done in the software, there has also been a physical change to the burner. Each burner consists of a certain amount of swirler vanes. These swirler vanes have nozzles in them, through which the premix gas is supplied to the mixing chamber. The swirling and the distribution of these premix nozzles allow for a homogeneous mixing with the air that is supplied to the combustion chamber. To limit the occurrence of combustion instabilities, Siemens suggested to reduce the amount of premix nozzles. The dynamic pressure amplitude (4.1a) was very high in FB2 while operating at part load, and this solution reduces the amplitude in this frequency band. It also has a damping effect on the FB2 amplitudes at base load, but it has more effect while operation happens at part load.

The gas nozzles will have the same influence on the fuel flow velocity as a change in fuel temperature will have. A hypothesis is that, due to problems with FB2 humming at part load, the pressure drop over the nozzle was too low. By reducing the amount of gas nozzles, the flow velocity is increased and thus the pressure drop is increased, making the nozzles less susceptible to upstream travelling waves.

However this reduction in amount of gas nozzles came with problems at maximum load. The hypothesis in this case is that due to the relatively high flow velocity at maximum load and the reduction in gas nozzles, the mixing happens less homogeneously. This will result in the aforementioned pressure waves travelling upstream from turbine inlet and is not analysed in this thesis.

### 4.3.3. Influence of cylindrical burner outlet

Fitting some of the burners of the SGT5-4000F with a cylindrical burner outlet (CBO), has allowed the units fitted with these type of burners to increase their max load. It will be interesting to analyse what a different flow field does to the response of the flame in the combustion system.

In figure 4.6 [22] the reacting flow field of three types of burners are shown. The arrows indicate the velocity vectors of the flow field, while the colors indicate the temperature at that point in the flow field, with blue being cold and red being hot. Encircled by the blackline is the re-circulation zone inside the flame. This flowfield provides a good basis to determine the flame length in the combustion system, as the burner dimensions are known. It is expected that the re-circulation zone is shorter then the flame length, so an initial assumption for the flame length can be based on the length of the re-circulation zone. This can be done for both the no burner outlet (NBO) and CBO configurations, which allows a good comparison of both models.

The increased flame length with the CBO configuration will result in increased convective time-delays, which will change the frequency response of the flame. As this flowfield is beneficial for an increase in power output, it is expected to see increased stability for the critical frequencies in FB2 and FB3 at base load. This influence will be further analysed in chapter 7.

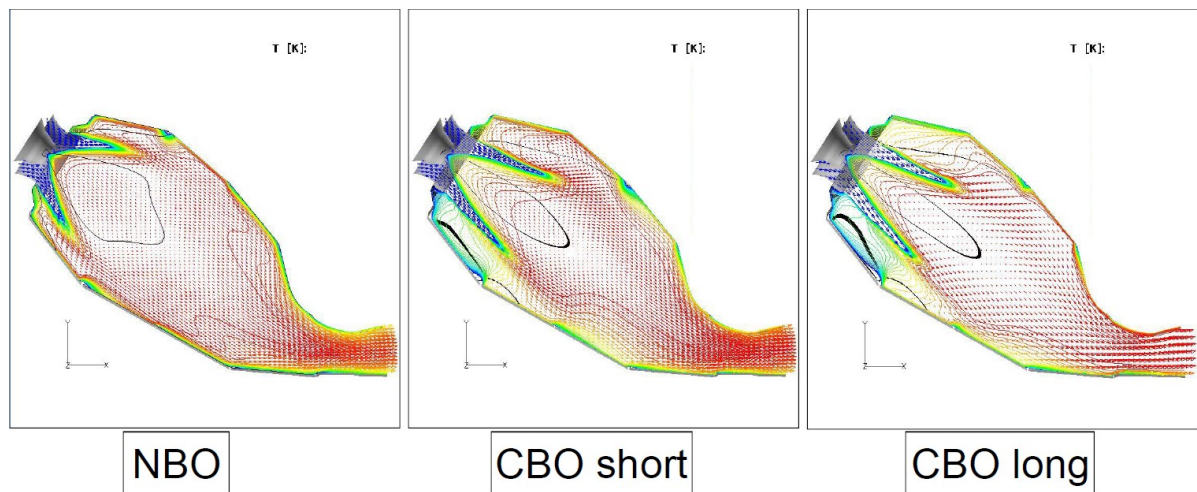


Figure 4.6: Reacting flowfield for burner configurations with no CBO, a short CBO or a long CBO [22]

# 5

## Cold flow model hybrid burner

In this chapter the cold flow model of the Siemens hybrid burner will be constructed, this is the model excluding the flame behaviour. The geometry will be discussed and each geometric element of the burner will be modelled as a transfer matrix. The constructed transfer matrix model of the hybrid burner will be validated afterwards using a paper by Kruger et al. [23], which was co-authored by Siemens employees.

### 5.1. Network model hybrid burner

The hybrid burner consists of a premix burner and a pilot burner part. For this thesis, the pilot burner part will be excluded. The occurrence of combustion instabilities will be due to fluctuations in the premix part, where the pilot part will only provide a stable base of combustion. When combustion instabilities occur, the pilot burner mass flow will increase to provide extra stability. By modelling and analyzing just the premix burner, the instability of the combustion system might thus be exaggerated. This means that the geometry of the pilot burner will not be taken into account in the upstream acoustics of the combustion system. This will result in differences between the burner impedance of the model compared with the real scenario.

The swirler vanes will not be taken into account either. In the model the assumption will be that the flow is one-dimensional and has no tangential velocity component. This assumption will be valid, as the non-axial dimensions of the burner are much smaller than the wave lengths. The flow will be a homogeneous mixture of air and gas, which is perfectly mixed. The swirler vanes will very slightly reduce the cross-sectional area at the mixing location, so a small area decrease will be taken into account here, this should approximate the influence of the swirler vanes on the acoustics.

The nodes of the premix hybrid burner are represented in the network model below, see figure 5.1 with all elements explained in table 5.1. The geometrical representation in figure 5.2, is established by analyzing the hybrid burner from Siemens and discarding the pilot burner, which results in the following adaption of the Siemens burner, figure 5.3. It will consist of 8 transfer matrix elements. At node 1 and node 5 a closed boundary condition will be used. At node 10, the end of the burner, no boundary condition will be used. The transfer matrix model will be rewritten in terms of  $p_{10}^-$  fluctuations. This will be done so the model can be validated by calculating the burner impedance. Imposing a boundary condition at the end of the burner will influence the upstream characteristics of the burner and will misrepresent the behaviour the burner will have when it is attached to the combustion chamber.

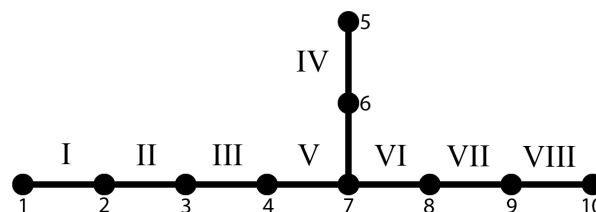


Figure 5.1: Acoustic network model of the hybrid burner

Element	Geometric Element	Transfer Matrix (eq.)
I	Compressor plenum and perforated plate	Helmholtz resonator (2.58)
II	Perforated plate and mixing chamber connection	Area change (2.38)
III	First part mixing chamber	Acoustic duct (2.30)
IV	Gas plenum and premix supply	Helmholtz resonator (2.58)
V	Air and gas supply junction	Junction (2.43)
VI	Second part mixing chamber	Acoustic duct (2.30)
VII	Connection mixing chamber burner outlet	Area change (2.38)
VIII	Burner outlet	Acoustic duct (2.30)

Table 5.1: Transfer matrix element representation

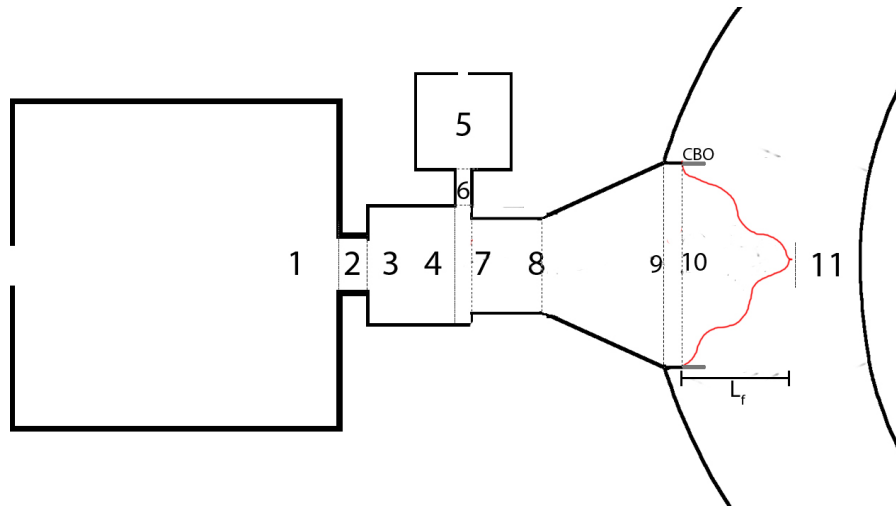


Figure 5.2: Geometric model of single burner with connection to annular combustion chamber

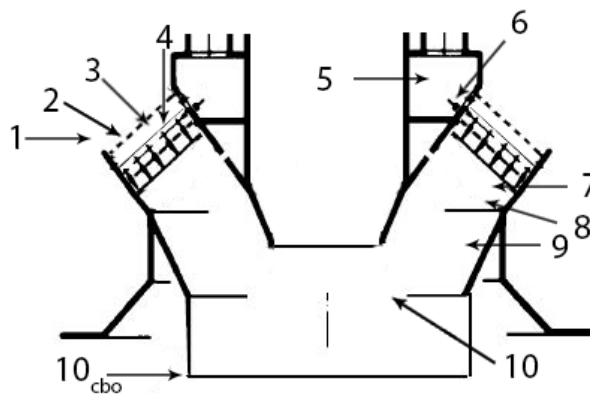


Figure 5.3: Interpretation of Siemens hybrid burner model with numbers indicating nodes

## 5.2. Burner impedance

The burner impedance will be used as the measure to validate the burner model. The burner impedance can be described as the ratio of the acoustic pressure fluctuations over the acoustic velocity fluctuations (5.1). If the impedance is high, the acoustic velocity fluctuation due to a pressure wave upstream of the burner will be low, which means that the acoustic velocity fluctuation of the mixture that gets supplied to the flame is low [23]. The heat release fluctuations will be lower if the acoustic velocity fluctuation is lower, as can be seen from equations (2.94b) and (2.96c), so a high impedance is preferred.

$$z = \frac{p'}{u'} \quad (5.1)$$

To calculate the burner impedance, the transfer matrix system has to be solved. This will be solved as a function of the upstream travelling pressure wave after the burner,  $p_{10}^-$ . This will follow the same derivation as was used to derive the reflection factor, only now the flame is excluded from the system equation (5.2a). This will result in the pressure components of the matrix system as a function of  $p_{10}^-$ .

$$[A] \cdot \begin{bmatrix} p_1^+ \\ p_1^- \\ \vdots \\ p_9^+ \\ p_9^- \\ p_{10}^+ \end{bmatrix} = \begin{bmatrix} A_{1,20} \\ A_{2,20} \\ \vdots \\ A_{17,20} \\ A_{18,20} \\ A_{19,20} \end{bmatrix} \cdot p_{10}^- \quad (5.2a)$$

$$\begin{bmatrix} p_1^+ \\ p_1^- \\ \vdots \\ p_9^+ \\ p_9^- \\ p_{10}^+ \end{bmatrix} = [A]^{-1} \begin{bmatrix} A_{1,20} \\ A_{2,20} \\ \vdots \\ A_{17,20} \\ A_{18,20} \\ A_{19,20} \end{bmatrix} \cdot p_{10}^- \quad (5.2b)$$

$$\begin{bmatrix} p_1^+ \\ p_1^- \\ \vdots \\ p_9^+ \\ p_9^- \\ p_{10}^+ \end{bmatrix} = \begin{bmatrix} H_1^+ \\ H_1^- \\ \vdots \\ H_9^+ \\ H_9^- \\ H_{10}^+ \end{bmatrix} \cdot p_{10}^- \quad (5.2c)$$

Now the burner impedance can be calculated at node 10. For this the relation between the positive and negative acoustic pressure amplitudes and acoustic velocity has to be used again, which results in the following result for the burner impedance.

$$z = \frac{p'_{10}}{u'_{10}} = \frac{p_{10}^+ + p_{10}^-}{\frac{p_{10}^+ - p_{10}^-}{\rho_{10} c_{10}}} = \frac{H_{10}^+ \cdot p_{10}^- + p_{10}^-}{\frac{H_{10}^+ \cdot p_{10}^- - p_{10}^-}{\rho_{10} c_{10}}} = \frac{H_{10}^+ + 1}{\frac{H_{10}^+ - 1}{\rho_{10} c_{10}}} \cdot p_{10}^- \quad (5.3)$$

The term  $p_{10}^-$  will drop from this equation, as this will be assumed to be just 1.

### 5.3. Burner validation

The burner will be validated using a paper written by Kruger et al. [23]. This paper uses an experimental validation and provides characteristics of the hybrid burner impedance in a combustion system. The provided characteristics are of the model they constructed and which does include the pilot burner. This burner does not include a CBO and the model was also constructed using the transfer matrix method.

The burner can be validated by calculating the magnitude, equation (5.4), and phase, equation (5.5), of the burner impedance. The comparison will be made between the model constructed by Kruger et al. [23] and the model that is constructed for this thesis.

$$|z| = \sqrt{\Re(z)^2 + \Im(z)^2} \quad (5.4)$$

$$\phi = \tan^{-1} \frac{\Im(z)}{\Re(z)} \quad (5.5)$$

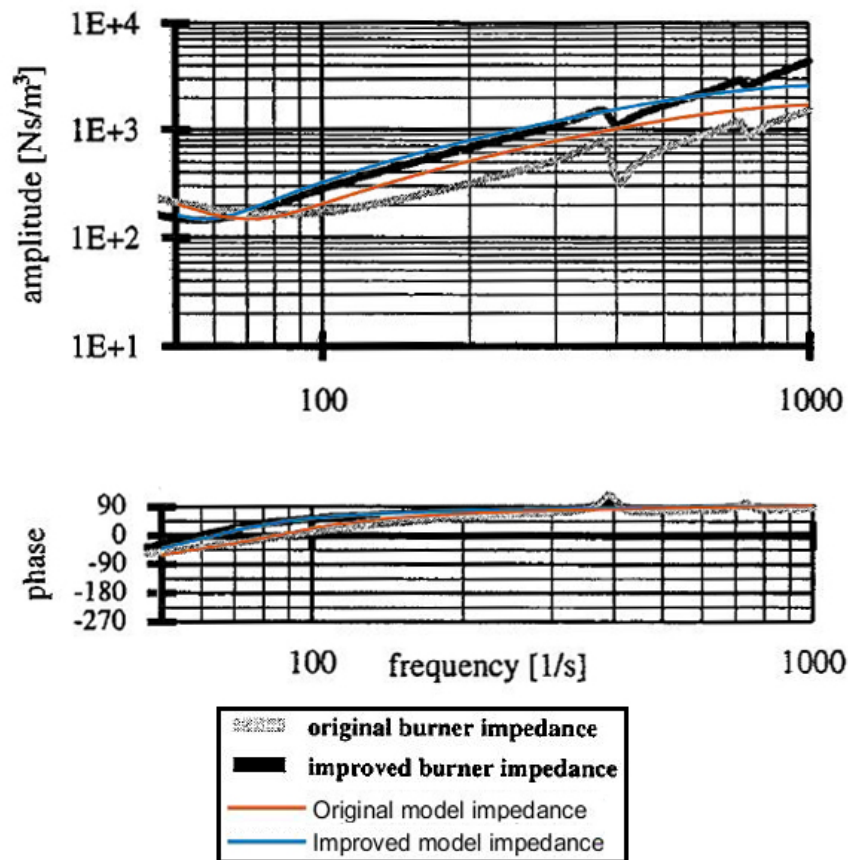


Figure 5.4: Comparison of magnitude and phase of burner impedance in the gas turbine combustion system from Kruger et al. [23] and modelled results

The magnitude/amplitude and phase of the burner impedance from Kruger et al. [23] and the constructed burner model are compared in figure 5.4. It is obvious that the impedance magnitude is higher for the original model as opposed to that of Kruger's results. This would mean that for a pressure wave in the combustion chamber travelling upstream to the burner, the acoustic velocity response would be lower. This would also result in less unsteady heat release at the flame front.

The improved burner impedance is the impedance for a small geometric change, which is lengthening the duct upstream of the mixing location [23]. In both the modelled results and Kruger's results, this increases the impedance. The model responds in an equal matter as the results from Kruger, the improved burner

impedance remains an equal slope up to 500 Hz after which it starts decreasing a bit. The phase results of the burner impedance also have a similar response as the results by Kruger [23].

Obvious are the drops in magnitude of the transfer function around 400 Hz and 800 Hz in Krugers results. These do not show up in the modelled system. This is most likely due to a resonance frequency in the pilot gas burner system. If an eigenfrequency can be established in the burner system, it becomes more sensitive to pressure waves in that frequency range, which would explain the drop in magnitude and the jump in phase. The second drop happens at about double the first frequency, which would indicate a higher wave mode of the eigenfrequency. The fact that the model does not show this behaviour is thus explainable. Besides that the analysis will only be done for frequencies up to 300Hz, as they are known to be most problematic in HW09 and DM34.

Both the magnitude and phase behaviour of the improved burner impedance show equal behaviour as the validation case from Kruger [23], at least up to 400 Hz. Seeing as the results are comparable, this validates the modelled burner geometry with experimental data. This provides a solid basis for the construction of the thermo-acoustic model, which will incorporate the flame behaviour. Further throughout this thesis the geometry indicated as the 'improved model impedance' will be used.



# 6

## Thermo-acoustic model SGT5-4000F

In this chapter the burner and combustion chamber of the Siemens SGT5-4000F gas turbine will be represented as a thermo-acoustic network model. This approach allows us to describe all elements, by connecting the network nodes, as a transfer matrix. The flame transfer function that will be implemented follows the one described by Lieuwen [26] and also in Cho & Lieuwen [6], it will take the influence of equivalence ratio fluctuations and velocity fluctuations at the burner outlet into account. A sensitivity analysis will be performed on the reflection factor of the flame. The system will be analysed for frequencies up-to 300Hz, as the frequencies below this are providing most issues in HW09.

### 6.1. Thermo-acoustic network model

The thermo-acoustic network model is an expansion on the acoustic network model presented in the previous chapter. Only one extra element is added, which describes the flame behaviour. This flame element also takes into account the feedback loops which are present due to the transportation of equivalence ratio fluctuations and mass fluctuations.

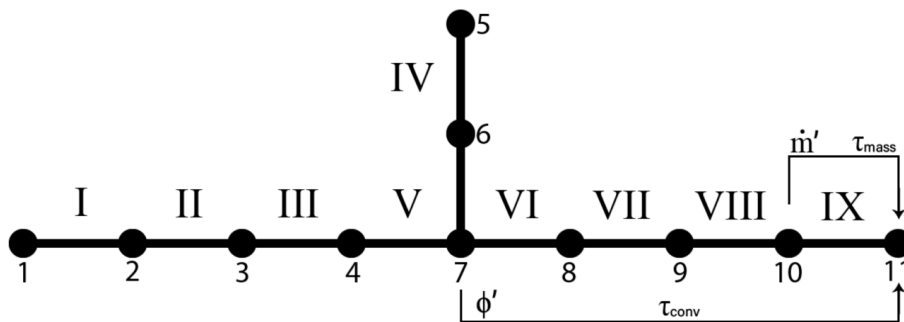


Figure 6.1: Acoustic network model of the hybrid burner with feedback

### 6.2. Flame transfer matrix element

The flame transfer matrix that will be used is the function that was derived in chapter 2, following the procedure of Cho & Lieuwen [6], Fleifil et al. [15] and Ducruix et al. [14]. The only thing that needs to be done is to rewrite matrix (2.99) to connect the different elements to the correct nodes, which results in matrix (6.2). The fluctuation in mass flow at the burner outlet will originate from node 10. The fluctuation in air mass flow, incorporated into the equivalence ratio fluctuation, will originate from node 4. Lastly the fluctuation in gas mass flow, also incorporated into the equivalence ratio fluctuation, will originate from node 6. All pressure waves from nodes in between will not directly affect the flame transfer matrix system, and will thus be equal to zero.



### 6.3. Expected (un)stable frequencies

From talks with Siemens, internal documentation [40] and data analysis, the frequency areas of interest are determined and are tabulated in table 6.1. The 80-100Hz and 170-190Hz areas belong to respectively the first and second harmonic wave modes of the combustion chamber. Siemens requires the 80-100Hz to be the dominant humming frequency in the combustion system, to allow for stable combustion. The 170-190Hz will balance on instability. The most critical area, at base load, will be 110-130Hz. This area can lead to large pressure amplitudes and can thus also result in large accelerations. When the gas turbine operates at low part load, the most critical frequency changes towards 220Hz area and 260Hz area. These frequencies are tabulated below and will serve as a guideline to tune the operational parameters to make sure the modelled combustion system responds in the expected ways.

Frequency band	Frequency range	Definition
FB2	80 - 100 Hz	Must be dominant for stable combustion
FB3	105 - 125 Hz	Critical frequency, amplification expected
FB5	150 - 180 Hz	Barely (un)stable
FB6	210 - 235 Hz	Critical at low part load
FB7	250 - 280 Hz	Critical at low part load

Table 6.1: Frequency areas of interest of SGT5 combustion system

The expected response for the pressure spectra will be that the largest pressure amplitudes will be in FB2, FB5 and FB7. These 3 frequency areas are the harmonic frequencies inherent to the combustion chamber dynamics and geometry. As the thermo-acoustic model does not take the entire combustion system into account, it will be no surprise if hardly any pressure amplitudes are present for FB3 and FB6. It is not expected that resonance is possible for these frequencies in the modelled combustion system, so large pressure amplitudes can not exist. The influence of the process parameters on these frequency areas can be investigated using the reflection factor response.

## 6.4. Model set-up

### 6.4.1. Burner and flame reflection factor

The flame transfer matrix element can be implemented in the total burner matrix system, so the entire burner and flame system can be modelled. From this system the burner and flame response can be calculated, which can be used as input for our entire combustion system. The system will be rewritten to calculate the reflection factor upstream of the flame in terms of  $p_{11}^-$ . Following the same steps as mentioned in chapter 3. This will result in the flame reflection factor, which will be called  $R_f$ .

$$p_{11}^+ = R_f \cdot p_{11}^- \quad (6.3)$$

### 6.4.2. Reflection factor response

The reflection factor response will be calculated using operating parameters from HW09 at base load, around 280MW gas turbine load. As the reflection factor is calculated for a single burner, all flows will be divided by the amount of burners in HW09, which is 24. An initial flame length  $L_f$  of 0.35m will be chosen, which corresponds to a length which is shorter than the re-circulation zone in figure 4.6, this to be on the safe side for flame length determination. The magnitude and phase of the reflection factor are shown in figures 6.3 and 6.4. The reflection factor shows amplification for frequencies between 10-75 Hz and for frequencies between 175-300+ Hz. Severe amplification is seen around 200Hz, which is unexpected. The 110-130 Hz is labeled as the most unstable and high risk frequency for these operating conditions, so amplification is expected in this area. From this reflection factor response it seems the convective time delay does not correspond with reality, as has been shown throughout this thesis it has a high influence on the flame response. This can also be seen by the phase jump, coupled effects seem to take amplification very high. Furthermore frequencies in the 90Hz and 180Hz range are of interest, but those should show up as eigenfrequencies of the combustion chamber. As the combustion chamber geometry is not taken into account in the reflection factor, it is not unexpected that there are no peaks/drops in this frequency range. It is known that the 180 Hz frequency balances between stability and instability, so small amplification or damping can be expected.

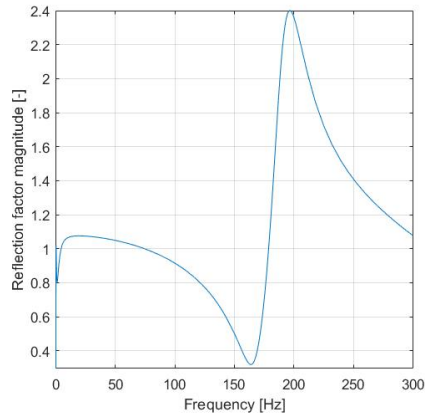


Figure 6.3: Initial reflection factor magnitude response for HW09 combustion system

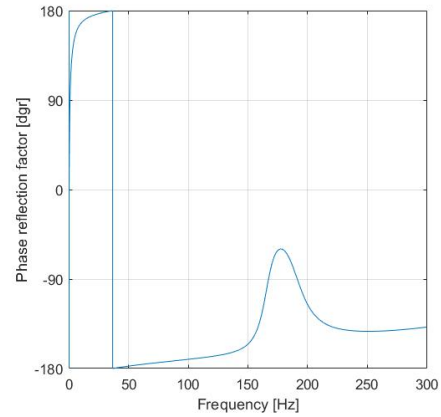


Figure 6.4: Initial reflection factor phase response for HW09 combustion system

### 6.4.3. Thermo-acoustic model

In chapter 3 it was shown that the reflection factor can function as input into a combustion system. To determine the response of the flame into a combustion chamber, the burner will be 'fitted' onto a cylinder with equal length  $L_{cc}$  as the circumference of the annular combustion chamber in HW09, see figure 6.5. Where 1 denotes the reflection factor input, 2 is a passive, infinitesimally small zone and arbitrary source of sound and 3 is a closed boundary. The assumption will be that the burner is fitted at a pressure node in the cylinder, see figure 6.6. This will show the maximum response the burner system will have to changes in operational parameters, as the acoustic pressure wave travelling upstream to the flame is assumed to be at it's maximum.

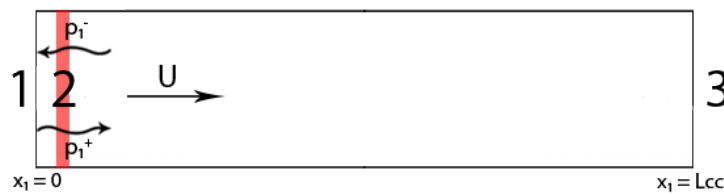


Figure 6.5: Graphical representation of burner fitted into combustion chamber

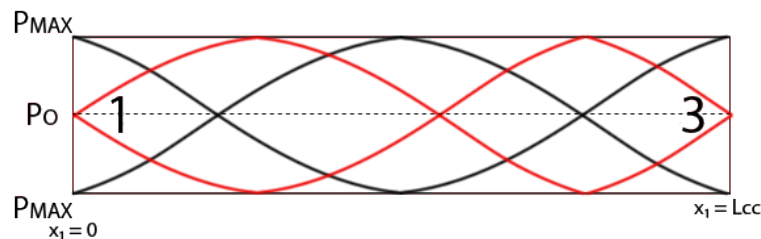


Figure 6.6: Pressure node (black) and pressure anti-node (red); system will be modelled at pressure node with input modelled at 1

Using this method, frequencies in the 90Hz and 180Hz and 270 Hz frequency range are expected to show up as resonance frequencies in the stability plot, as they are harmonic frequencies of the combustion chamber and are a function of the combustion chamber length and speed of sound. The reflection factor will function as the boundary condition on the left side of the cylinder. The passive source of sound has a strength  $s$ . Expected is that the source term decays with increasing frequency by a factor  $f^{-5/3}$ , which was shown by De Jager [8]. The value for  $s$  will be determined later, to match pressure levels that are expected from combustion data. The matrix system will be as follows:

$$\begin{bmatrix} 1 & -R & 0 & 0 & 0 & 0 \\ 1 & 1 & -1 & -1 & 0 & 0 \\ \frac{1}{\rho_1 c_1} & -\frac{1}{\rho_1 c_1} & -\frac{1}{\rho_2 c_2} & \frac{1}{\rho_2 c_2} & 0 & 0 \\ 0 & 0 & e^{-ik^+ L_{cc}} & 0 & -1 & 0 \\ 0 & 0 & 0 & e^{ik^- L_{cc}} & 0 & -1 \\ 0 & 0 & 0 & 0 & 1 & -1 \end{bmatrix} \cdot \begin{bmatrix} p_1^+ \\ p_1^- \\ p_2^+ \\ p_2^- \\ p_3^+ \\ p_3^- \end{bmatrix} = \begin{bmatrix} 0 \\ 0 \\ s \cdot f^{-5/3} \\ 0 \\ 0 \\ 0 \end{bmatrix} \quad (6.4)$$

#### 6.4.4. Stability plot

From this system (6.4) the determinant will be calculated and using Matlab solutions will be found for which the determinant equals zero. This results in a complex frequency of the form  $f + i \cdot \alpha$  where the real part will be the resonance frequency and the imaginary part will be its growth rate. A negative growth rate will result in an unstable frequency, while a positive growth rate indicates the system remains stable. To determine if the eigenfrequencies of the system are correctly modelled, an extra system will be analyzed. In system (6.4),  $R$  will be changed to 1. This should provide a stability plot where all resonance frequencies have a growth rate equal to 0. The feedback that is talked about throughout this thesis is all incorporated into the reflection factor. If this reflection factor is changed to 1, the left boundary of the combustion system will function as a closed end. This analysis should provide us with the eigenfrequencies of the combustion chamber, when no unsteady heat release is present.

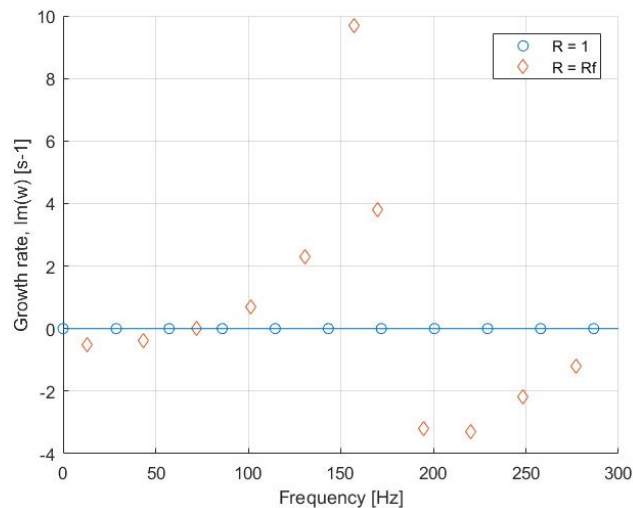


Figure 6.7: Stability plot HW09 burner; negative growth rate is unstable

The stability plot clearly shows an array of resonance frequencies with a growth rate equal to zero, for the system with reflection factor 1. Eigenfrequencies are found at 86Hz, 172Hz and 260 Hz, which is where the eigenfrequencies of the combustion chamber are expected to be found. Other eigenfrequencies are found as well, but these will not be used as they are not the harmonic frequencies of the combustion chamber but different wave modes. Since the combustion chamber is annular, the pressure should be equal on the left and right side of the system, this is not the case for those wave modes but only true for the harmonic frequencies. This is why for the stability of the combustion system the only focus will be on the harmonic frequencies. 'Activating' the flame, by changing the reflection factor to  $R_f$ , changes the real part of the eigenfrequencies, but also adds instability. Comparing these results with the magnitude of the reflection factor in figure 6.3, they are in accordance with one-another. For eigenfrequencies that have a reflection factor magnitude above 1, the growth-rate is negative, which means those are unstable frequencies. This makes sense, as a reflection factor magnitude higher than 1 means that the upstream travelling pressure wave is amplified when it is reflected back into the combustion chamber. This adds energy to the system and will increase the acoustic pressure wave as time progresses.

## 6.5. Reflection factor sensitivity

### 6.5.1. Introduction

In this section the sensitivity of the reflection factor will be analysed. It has been shown that for a system with reflection factor equal to 1, the expected harmonic frequencies are found. To determine the parameters that will be used throughout the case studies, a sensitivity analysis on the reflection factor will be done. The response of the reflection factor will be analysed at base gas turbine load, around 280 MW, and changed parameters will include flame length, convective time-delay and flame speed. The parameters that will be chosen are those that will closely resemble the expected behaviour of the combustion system. Those will be the base-case parameters that will be used for the case-studies in the following chapter.

### 6.5.2. Flame length influence

A change to the flame length will also lead to a change in convective time-delay and flame area. The change in convective time-delay should lead to shifts in frequencies. The flame area change will lead to a change in the unsteady heat release, as it is directly related to the flame area.

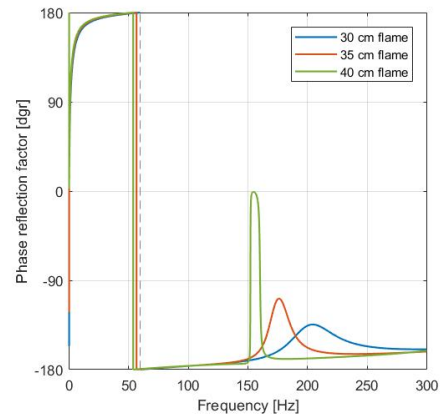
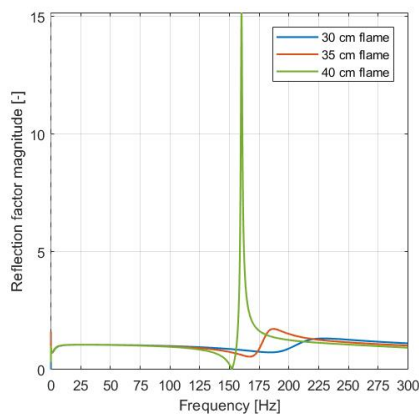


Figure 6.8: Reflection factor magnitude for different flame lengths      Figure 6.9: Reflection factor phase for different flame length

Figure 6.8 shows the magnitude of the reflection factor for different flame lengths. For all used flame lengths, the reflection factor has a significant amplification in a single frequency area. For increasing flame length, the peak shifts towards lower frequencies. From the expected behaviour of the system, this peak should lie around the 110 - 130 Hz area, as that is expected to be the critical frequency area which should respond be visible in the flame reflection factor. This implies that the time delay should be increased to shift the peak response towards lower frequencies.

The influence of the time-delay is also visible in the phase plot of figure 6.9. The phase plot of the reflection factor slowly increases, but all three the flames have a distinct increase in magnitude which corresponds to a jump in phase, with the 40 cm flame being the most extreme case. Analysis of the unsteady heat release response shows that for this case both effects that result in heat release coincide, which results in a sudden increase in unsteady heat release. This suggests that the convective time delay should be changed to shift these responses away from one-another.

### 6.5.3. Time delay influence

The time delay change will have a direct influence on the resonance frequencies of the flame reflection factor. For this analysis a flame length of 40 cm will be used, while the convective time delay for both velocity and equivalence ratio perturbation will be increased by a factor 1.5x and 2.0x. Without an increase in time delay, the convective time delays are 0.0054s for the equivalence ratio perturbations and 0.0047s for the velocity fluctuations at the burner mouth. The increase in time delay results in the same increase as if the flame length would be increased with this factor. The choice to alter the time delay is to take the influence of the flame length on the flame transfer function out of account and to find a correct time delay for amplification to occur at 110 - 130 Hz.

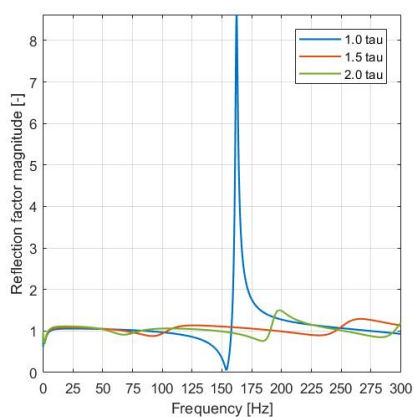


Figure 6.10: Reflection factor magnitude for different time-delay correction factors

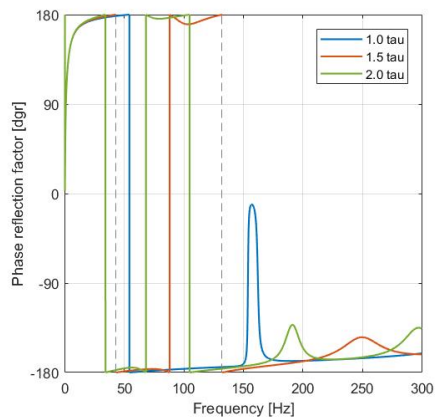


Figure 6.11: Reflection factor phase for different time-delay correction factors

As expected the time-delay changes the phase of the reflection factor, this shifts the coinciding combustion effects away from each other. A multiplication of the time-delay with a factor of 1.5x and a flame length of 40 cm shows a shift of resonance frequencies towards the 110-130 Hz area. This time-delay corresponds to a system with a flame length around 60 cm. A further sensitivity analysis of the flame length will be done for lengths of 55 cm, 60 cm and 65 cm. First the influence of a flame speed correction factor will be analysed.

### 6.5.4. Flame speed influence

As mentioned in this thesis, the flame speed response as a function of the equivalence ratio is a very important factor. In figures 2.21 and 2.22 it was shown that this response heavily changes with increased temperature and pressures. The equation for the flame speed, (2.88), that is used in this model is based on 300K and 1 atm. This is why a correction factor  $K_c$  was introduced, which changes the response as can be seen in figure 6.12. The heat of reaction follows a linear response versus the equivalence ratio, but this will also be increased with a factor  $K_h$  to determine its influence. The influence of both correction factors will be analysed with a flame length of 40 cm and a time-delay correction factor of 1.5x. The initial flame speed is increased by a factor of 50, as the flame speed model uses a laminar flame speed instead of turbulent flame speed. Turbulent flame speed is about 10 - 100 times as high as laminar flame speed.

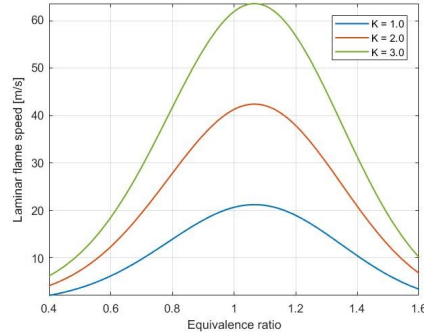


Figure 6.12: Influence of  $K_c$  on flame speed versus equivalence ratio

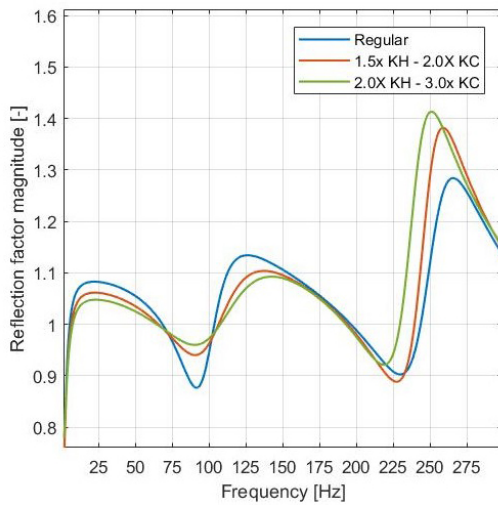


Figure 6.13: Reflection factor magnitude for different correction factors

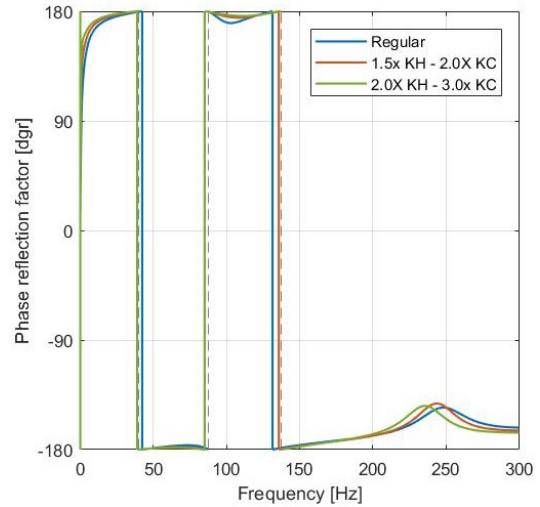


Figure 6.14: Reflection factor phase for different correction factors

Without a correction factor for the flame speed or heat of reaction, there is large damping around the 90 Hz area. This area is an eigenfrequency of the combustion chamber and an important one. It is expected that this frequency is stable, but it has shown to turn unstable in some case. The reflection factor magnitude gets closer towards 1 for the two other cases, so they seem more realistic. The most extreme case shows very high amplification around the 250 Hz area, which is not necessarily expected behaviour at base load. A value for  $K_h$  of 1.0 and a value for  $K_c$  of 2.0 will be chosen.

### 6.5.5. Flame length influence

Again the flame length influence will be taken into consideration. From the first sensitivity analysis for flame length and for time-delay, the reflection factor magnitude showed behaviour that was expected for a flame length of 40 cm and a time delay increase of 1.5x. It is chosen to further investigate the flame length for lengths of 55 cm, 60 cm and 65 cm, without a time-delay correction factor. These flame lengths all still fall into the range that is considered based on figure 4.6. These flame lengths result in a time delay for the equivalence ratio perturbations of respectively 0.0071s, 0.0077s and 0.0083s. For the velocity fluctuations at the burner mouth these are respectively equal to 0.0064s, 0.0070s and 0.0076s.

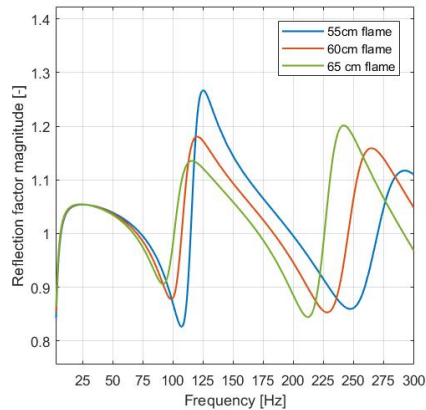


Figure 6.15: Reflection factor magnitude for different flame lengths

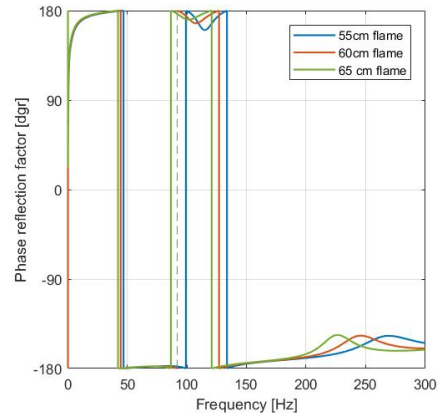


Figure 6.16: Reflection factor phase for different flame lengths

From figure 6.15 the 55 cm flame shows relatively high amplification around the 110-130 Hz area. The 60 cm and 65 cm flame both show similar behaviour, although the peaks and troughs of the reflection factor magnitude are shifted due to a different time delay. All three flame lengths will be fitted into a combustion chamber with an equal length as the circumferential direction of the annular combustion chamber, to determine which pressure spectrum seems most realistic. This is equal to a one-dimensional cylindrical combustion chamber.

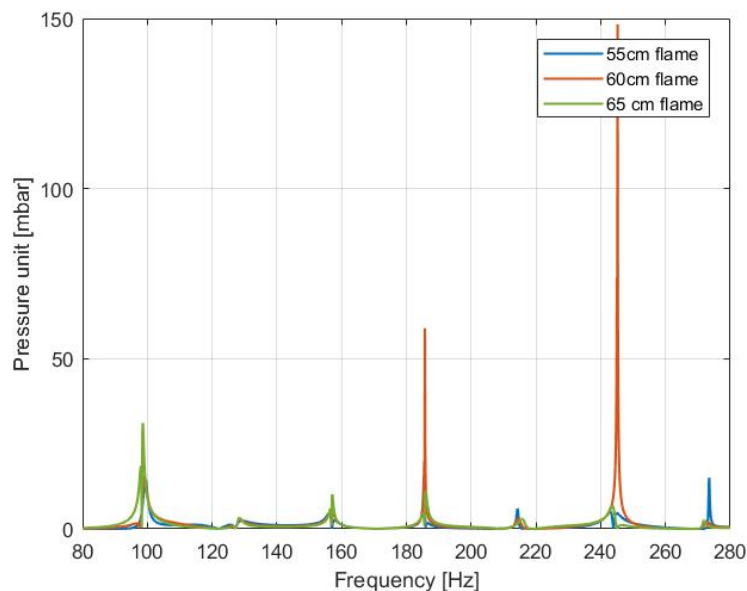


Figure 6.17: Pressure spectrum 80 - 280 Hz for different flame lengths

From this pressure spectrum, figure 6.17, it is very noticeable that the 60 cm flame shows very high pressure amplitudes at around 185 and 245 Hz. This is not a realistic pressure spectrum, as the pressure amplitudes should be highest around the 90 Hz area. In figures 6.18 and 6.19 a closer look is taken on the 95 Hz and 185 Hz ranges. For the 65 cm flame at 95 Hz it shows that the pressure amplitude has a steep increase, then suddenly drops and then increases again. This is unusual behaviour, which is slightly noticeable for the 60 cm flame, but not noticeable at the 55 cm flame. It seems that with this specific time-delay, due to the flame length, the flame transfer function effects coincide with the harmonic frequency of the combustion system. At 185 Hz, the large amplitude peak is noticed at 60 cm flame length. The 55 cm pressure amplitude at 185 Hz is high in comparison to the amplitude at 95 Hz, which should be the other way around. A flame length of 62.5 cm will be chosen, as a medium between the cases of 60 cm flame length and 65 cm flame length.

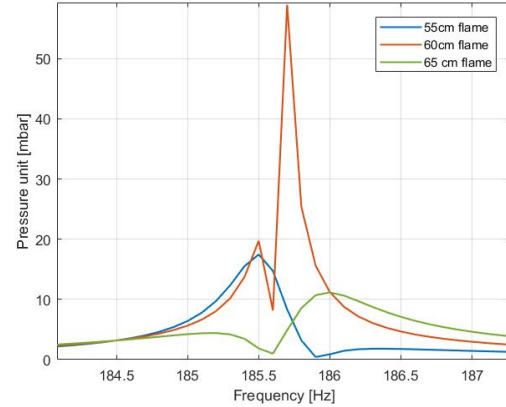
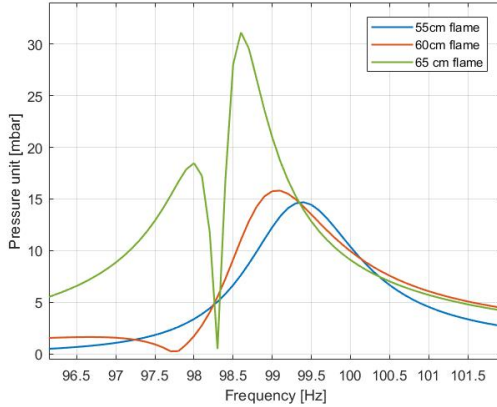


Figure 6.18: Pressure spectrum around 95 Hz for different flame lengths

Figure 6.19: Pressure spectrum around 185 Hz for different flame lengths

### 6.5.6. Conclusion

From the expected stability of the frequencies mentioned in the system, the assumption is made that FB2 will be a stable frequency, FB3 will be the most unstable frequency and FB5 will be on the edge of stability. Combining this knowledge together with the results of the sensitivity analysis results in the base-case values mentioned in table 6.2. A flame length of 62.5cm together with a time-delay correction factor of 1.0x shows damping/amplification in the expected areas. The flame speed correction factor of 2.0x takes the stability of the system further in the expected direction, decreasing the damping in the FB2/90Hz area. The heat of reaction correction factor will remain at 1.0x. The expected harmonic frequencies of the combustion system were found for a reflection factor equal to 1. By including flame effects these have shifted and the harmonic frequencies were very noticeable in the pressure spectrum. FB2 has shifted towards the 90 - 100 Hz area, FB5 towards the 180 - 190 Hz area and FB7 towards the 240 - 250 Hz area.

Parameter	Value
Gas turbine load	280 MW
Flame length	62.5 cm
Premix nozzles	9 holes
Time-delay correction $K_\tau$	1.0x
Flame speed correction $K_s$	2.0x
Heat of reaction correction $K_h$	1.0x
FB2	90 - 100 Hz
FB5	180 - 190 Hz
FB7	240 - 250 Hz

Table 6.2: Base-case values for model input at base load

# 7

## Case studies

In this chapter the behaviour of the single burner combustion system will be analyzed. Certain relationships between e.g. fuel temperature and amount of premix gas nozzles versus combustion dynamics behaviour are known from confidential Siemens reports and operational data analysis. Simulating and recreating this behaviour will allow us to validate the model on those aspects. If the model responds to these changes as expected, the model can be used to identify other relationships between operational parameters and the combustion system stability. After the validation cases the influence of the cylindrical burner outlet (CBO) will be analysed, as well as the influence of natural gas composition.

### 7.1. Fuel preheating temperature

From data analysis and communications with Siemens employees, it is known that the 90Hz combustion instabilities respond to changes in fuel preheating temperature. A decrease in fuel preheating temperature will result in an increase in 90Hz amplitude. Changing this preheating temperature in our model, should show an increase in reflection factor amplitude around this area. An increased reflection factor should also result in a decrease of the growth rate, which will be seen in the stability plot. The pressure spectra should show an increase in pressure amplitude in the 90 Hz range.

A decrease in fuel temperature is used to increase the stability of the system. The expectation is that as the 90 Hz band pressure amplitude is increased, this frequency remains stable but its growth rate will decrease. As the 90 Hz humming should be dominant to provide a stable system, a change in the response at 110-130 Hz is expected as this is the critical frequency for base load combustion. This frequency domain should become more stable and thus the reflection factor shows a decrease in that area. A changed response in the 110-130 Hz area in the modelled pressure spectrum is not expected, this is due to the fact that this area is not a fundamental frequency of the combustion chamber so resonance is not expected. The reflection factor magnitude around this frequency can be analysed to indicate what the behaviour will be with changes fuel temperatures, as this should show the amplification/damping. A decrease in the reflection factor magnitude around the 120 Hz range should indicate that, when fitted in to the actual combustion system, the pressure amplitude would decrease. This effect is seen when analysing the combustion data at different fuel temperatures. In Appendix B this data can be found, which is a series of pressure spectra from HW09 operational data, taken from the Argus system [39]. These pressure spectra are at comparable load levels but different fuel temperatures, one of them at 100°C and the other at 150°C. These pressure spectra show the influence of the gas preheating temperature on the acoustic pressure in the frequency bands of interest. The stability of the system will be analysed for three different fuel preheating temperatures: 100°C, 150°C and 200°C.

The fuel is supplied to the mixing chamber and mixed with the air through the premix gas holes in the swirler vanes. The air supplied to this mixing chamber is in much larger quantity and at higher temperature, thus the influence of the fuel temperature on the mean temperature is assumed to be negligible. The fuel premixing temperature will have an influence on the fuel density and thus the flow velocity from the premix gas nozzle. An increase in fuel temperature will result in a lower gas density and thus a higher outflow velocity. A higher outflow velocity will result in a more 'impinging' fuel jet into the air and can change the mixing of the fuel and air. Mixing effects are very difficult to describe, so this effect is not taken into account in the thermo-acoustic

model, which assumes a 100% homogeneous mixture. Another effect due to a change in the gas flow velocity is the pressure drop over the gas nozzles. A higher fuel temperature will result in a higher pressure drop over the nozzle, as the gas flow velocity is increased. It has been observed by Hulka & Hutt [18] that a low-pressure drop fuel nozzle can show more susceptibility to combustion instabilities. In the case here, a lower temperature is equivalent to a lower pressure drop and vice-versa. The basic operating conditions are shown in table 7.1, the only changed parameter will be the fuel temperature.

Operating parameter	Value
Gas turbine load	Base load - 280MW
Flame length	62.5 cm
Number of premix gas nozzles	9
$\tau_c$	0.0080 s
$\tau_f$	0.0073 s

Table 7.1: Basic operating conditions for analysis of influence of gas preheating temperature

Frequency band	Frequency range	Expected response - Reflection	Expected response - Pressure
FB2	80 - 100 Hz	Amplification	Increased amplitude
FB3	110 - 130 Hz	Damping	-
FB5	170 - 190 Hz	Damping	Decreased amplitude
FB6	210 - 230 Hz	Amplification	-
FB7	260 - 280 Hz	Amplification	Increased amplitude

Table 7.2: Frequency areas and expected responses for a gas preheating temperature decrease from 200C to 100C

### 7.1.1. Gas supply impedance

In chapter 5 it was indicated that an outlet with a high impedance is less susceptible to pressure fluctuations resulting in velocity fluctuations. If the assumption is correct that a higher pressure drop over the gas nozzles will result in a system that is less susceptible to pressure fluctuations, this should also be noticeable as an increase in the gas supply impedance. The impedance of the gas supply can be calculated using the same method as shown in chapter 5, equations (5.1)-(5.3), although  $p'$  and  $u'$  should be evaluated at node 6 of figure 5.1. Figure 7.1 shows the fuel supply impedance for different fuel temperatures. The pressure drop over the nozzle is highest for high fuel preheating temperatures, the assumption that the fuel nozzles becomes less susceptible to pressure perturbations in case of higher pressure drop over the nozzles shows to be correct.

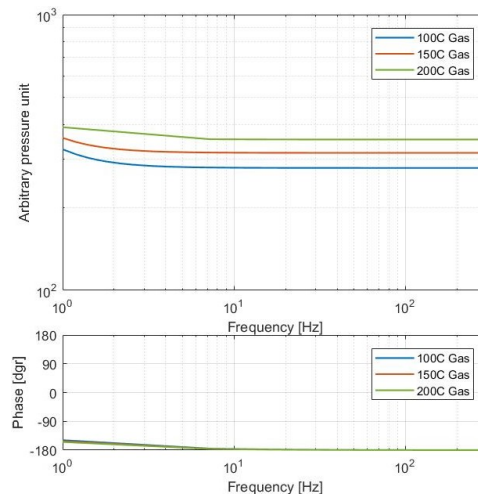


Figure 7.1: Impedance gas supply for different fuel temperatures

### 7.1.2. Unsteady heat release

The unsteady heat release by the flame can be calculated using equations (2.94a)-(2.94c) for the unsteady heat release due to velocity fluctuations at the burner mouth and using equations (2.96a)-(2.96d) for the unsteady heat release due to equivalence ratio fluctuations. With an increase in gas supply impedance at higher gas temperature, it is expected that the magnitude of the unsteady heat release due to equivalence ratio perturbations decreases. Assuming a pressure wave of equal strength travelling upstream into the burner, at higher temperature this will result in a smaller perturbation of gas outflow velocity, and thus a smaller fluctuation of gas mass flow. That will result in a smaller fluctuation of equivalence ratio, and thus a smaller fluctuation in flame speed and a decrease in heat release magnitude.

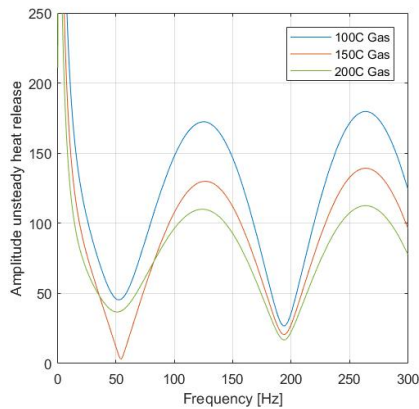


Figure 7.2: Magnitude of unsteady heat release due to equivalence ratio fluctuations

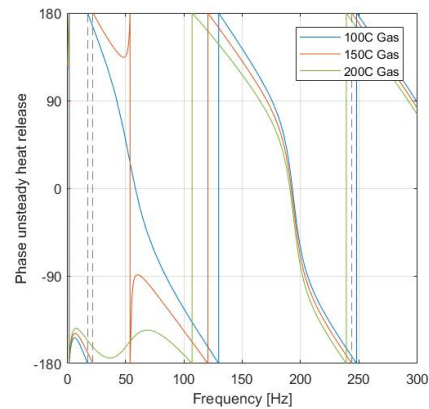


Figure 7.3: Phase of unsteady heat release due to equivalence ratio fluctuations

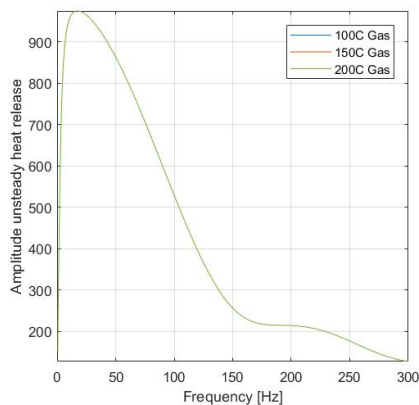


Figure 7.4: Magnitude of unsteady heat release due to velocity fluctuations at the burner mouth

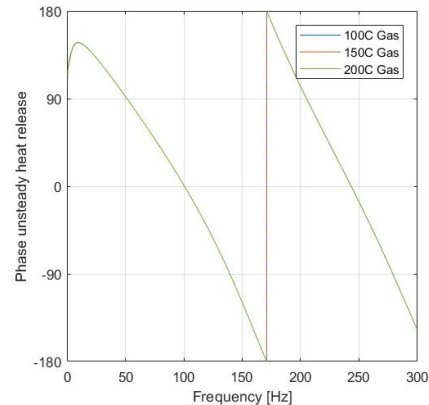


Figure 7.5: Phase of unsteady heat release due to velocity fluctuations at the burner mouth

The unsteady heat release due to velocity fluctuations at the burner mouth remains unchanged by fuel temperature changes, see figures 7.4 and 7.5. This is not surprising as the change in fuel preheating temperature only changes the dynamics at the mixing location. A significant change happens in the unsteady heat release due to equivalence ratio perturbations, as shown in figures 7.2 and 7.3. With an increase in fuel supply impedance, the gas flow velocity fluctuation was expected to decrease and thus the magnitude of the unsteady heat release should also decrease and as can be seen, it does decrease. The phase response of the unsteady heat release does however also change significantly for different fuel temperatures, especially for frequencies up to about 130 Hz. This phase change can result in increased instability, even though the magnitude has reduced. Looking at the 120 Hz area, the unsteady heat release response suggests that the least heat will be released for the 100°C gas case. For the 150°C gas case, the phase response shows a severe jump in phase around the 50 Hz area. This may suggest that acoustic effects in the burner system couple with the unsteady heat release.

### 7.1.3. Reflection factor

Below the magnitude and phase of the reflection factor are plotted. Expected is that for a lower temperature, the damping is decreased in the 90Hz area, as the 90Hz acoustic pressure should increase. From figure 7.6 it is clear that this is indeed the case. Simultaneously it is expected that the amplification in the 120Hz area is decreased, as it has been noticed that the 120Hz acoustic pressure amplitude is lower and the frequency is expected to be more stable in case of an increase in 90 Hz, this can also be seen from figure 7.6. The other harmonic frequency at around 180Hz shows little change for different fuel temperatures, this also showed for the unsteady heat release as no significant changes were present in that frequency area. With the 120Hz area being the most critical at base load, a decrease in gas preheating temperature seems to indeed increase the stability in this area. The response in FB6, while not critical at base load, seems to be as expected. The response in FB7 however is not, as it is expected here that the pressure amplitude will increase with lower gas temperature, but the reflection factor magnitude shows otherwise.

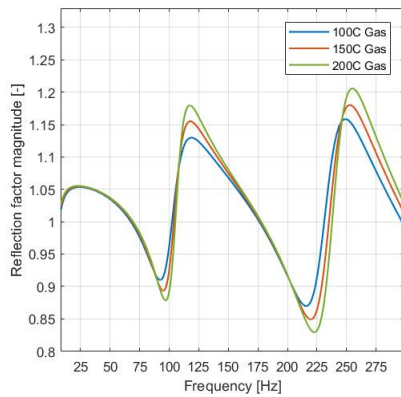


Figure 7.6: Fuel preheating temperature influence on reflection factor magnitude

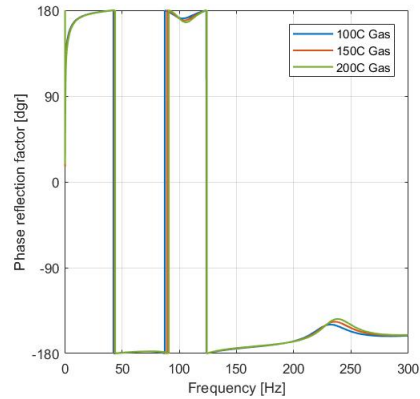


Figure 7.7: Fuel preheating temperature influence on reflection factor phase

### 7.1.4. Stability plot

Coupling the reflection factors with the one-dimensional cylindrical combustion chamber allows the stability of the frequencies to be determined. The main focus here is on the stability between 90 - 100 Hz (FB2), 180 - 190 Hz (FB5) and 240 - 250Hz (FB7), as these are the harmonic frequencies that exist in the combustion chamber. The increased or decreased stability of frequencies corresponds well with the changes in amplification and damping of the reflection factor. The changes in fuel temperature do not result in large shifts in eigenfrequencies of the system, which is as expected. An important note to make is that the acoustics of the one-dimensional cylindrical combustion chamber are taken into account in this model, in the actual combustion chamber additional damping might occur.

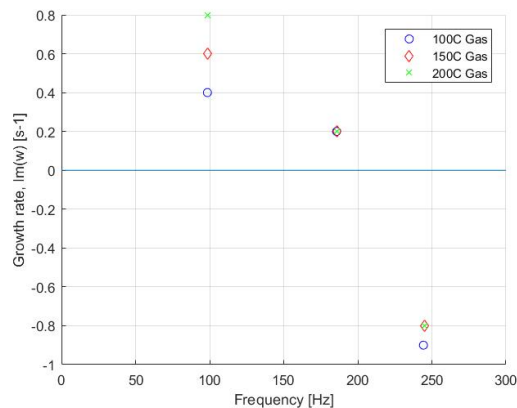


Figure 7.8: Fuel preheating temperature influence on stability plot

### 7.1.5. Pressure spectra

A pressure spectrum should provide more insight in the actual resonance in the combustion chamber. Figure 7.9 shows this pressure spectrum at different fuel temperatures for the range of 80 - 280 Hz. What is very noticeable are the harmonic frequencies of the combustion chamber, the first being close to 100 Hz, the second around 185 Hz and the third around 245 Hz. These are the frequencies indicated as FB2, FB5 and FB7. As expected there are no significant pressure amplitudes found at FB3 and FB6. The increased FB2 pressure amplitude with decreasing fuel temperature is very noticeable, so this shows that the expected behaviour in this area is correctly predicted, a closer look is shown in figure 7.10. The change in pressure amplitude while going from 150C gas to 100C gas is comparable with the absolute change in pressure amplitude that is shown in figure B.1, where the average pressure amplitude increases with about 5 mbar for this change in temperature.

The pressure spectrum from FB5 is shown in figure 7.11. The expected effect of a decreased pressure amplitude is also shown here. The absolute change in pressure is not as significant as in FB2, but this was also not expected while looking at the process data in figure B.3. The average pressure amplitude just slightly increases.

The expectations are that the pressure amplitude in FB7 would increase with a lower fuel temperature, but figure 7.12 suggests otherwise. The pressure spectra all show strange behaviour around the eigenfrequencies, which indicates that there is still a coupling of effects around the harmonic frequencies of the annular chamber. A small shift in time-delay might be able to mitigate this behaviour.

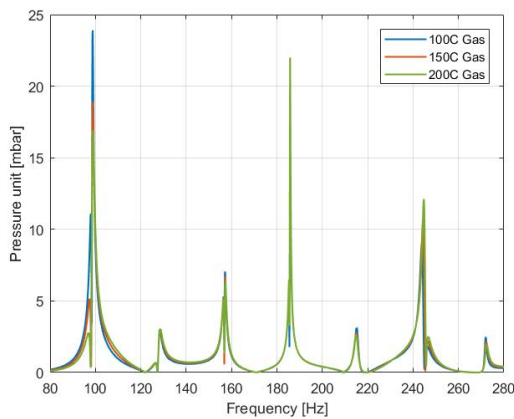


Figure 7.9: Pressure spectrum between 80 - 280 Hz for different fuel preheating temperatures

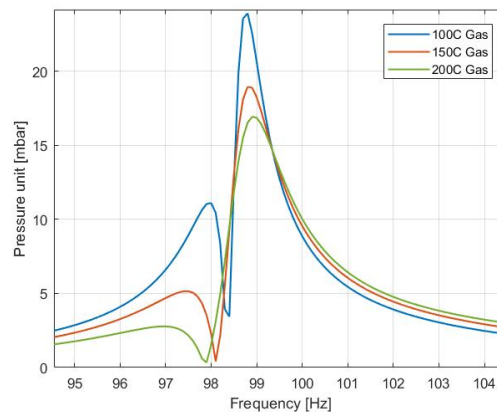


Figure 7.10: Fuel preheating temperature influence on pressure amplitude in FB2

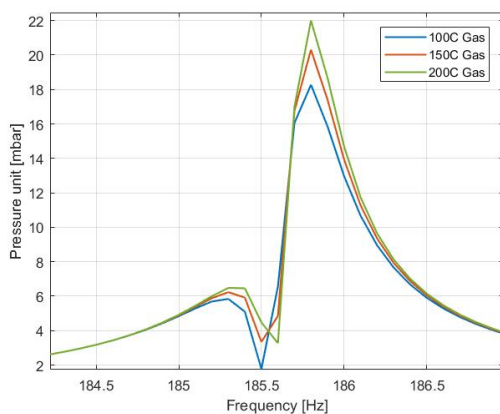


Figure 7.11: Fuel preheating temperature influence on pressure amplitude in FB5

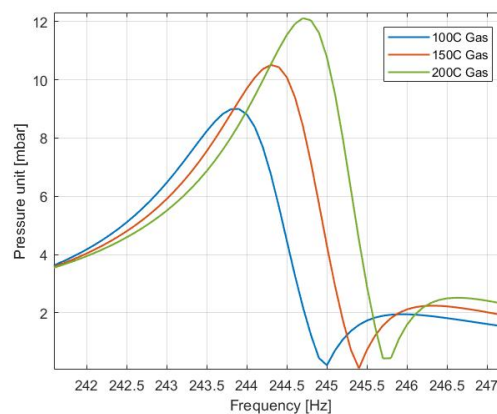


Figure 7.12: Fuel preheating temperature influence on pressure amplitude in FB7

### 7.1.6. Conclusion and discussion

The thermo-acoustic model for the SGT5-4000F gas turbine shows a comparable response due to changes in fuel preheating temperature for frequencies up to the second harmonic frequency. The fuel preheating temperature influences the dynamics of the gas flow at the gas supply, as well as the unsteady heat release due to equivalence ratio perturbation. The magnitude of the unsteady heat release changes, but also the phase changes. The shift in phase shows to shift the heat release towards the 90 Hz range, for decreasing fuel temperatures. This shows that the 90 Hz (FB2) range responds to the fuel preheating temperature as expected, which results in an increase in 90 Hz reflection. The increase in absolute pressure amplitude when changing fuel temperature is comparable in the 90 Hz range. With increasing FB2 humming, the critical frequency 120 Hz is expected to become more stable. This also shows in the unsteady heat release, as less heat is released around the 120 Hz area. The reflection factor shows that there will indeed be an increase in damping in this frequency range, which suggests that the frequency becomes more stable. This frequency does not resonate in the modelled combustion system, so the pressure amplitude response can unfortunately not be analysed. The second harmonic combustion chamber frequency, 180 Hz (FB5) also shows the assumed response. Interestingly, the reflection factor magnitude around this area is almost equal for all gas temperatures, which also shows in the stability plot. The pressure amplitude does however show the expected decrease in amplitude for a lower gas temperature. The unsteady heat release adds energy to the combustion chamber, if a frequency amplifies this energy a higher pressure amplitude is expected. The fact that a negligible change in reflection factor and stability does change the pressure amplitude in FB5, suggests that when the 90 Hz acoustic pressure amplitude increases more of the acoustic energy is shifted towards this frequency range. This explains the reasoning from Siemens to keep the 90 Hz area dominant, which lowers the pressure amplitudes in the more critical frequency ranges.

Frequency band 6 is not a critical frequency while operating a base load, and also does not resonate in the combustion chamber. The response to a temperature change on the reflection factor is however as expected. It would be interesting to see the change of its pressure amplitude in a more complete combustion system.

The only response that does not correspond to the expectations is the response of FB7, the third harmonic frequency of the combustion chamber. This response is exactly opposite of what was to be expected, as the pressure amplitude increases with increasing gas temperature instead of the other way around. As the frequency becomes higher, questions can be asked about the assumption of the compact flame. Wave lengths get shorter with increasing frequency, but the flame length remains equal. It might be the case that the assumption for the jump conditions across the compact flame are no longer valid in this frequency range, so the behaviour can not be accurately modelled. When the acoustically compact flame assumption is no longer valid this means that compressibility, 2D and 3D effects have to be taken into account.

## 7.2. Premix burner modification

The premix burner modification from 10 to 9 nozzles was done for reduction of 90 Hz humming, both during part load and base load operation, but was deemed more significant at part load combustion. A change in this parameter should result in the combustion model to show the same damping around the 90Hz frequency band. A deeper look will be taken into the influence of the reduction of premix burner gas nozzles from 10 to 9. From a confidential report by Siemens [41] it is known that a reduction of the fuel nozzles will result in decreased 90Hz humming at base load, while the 110/120Hz humming will be slightly increased at base load. The results for different load levels can be seen in figure 7.13. A reduction to just 8 nozzles will also be taken into account, as this should also result in a damping of the 90Hz humming. The influence of the reduction to 8 holes on different frequency ranges is unknown. No operational data is available to compare the response in different frequency ranges before and after the reduction in fuel gas nozzles. The data provided by Siemens is the only grasp to determine if the modelled response is valid.

This change will result in somewhat of the same physical alterations as with the fuel temperature. A reduction in amount of gas nozzles will result in an increase in gas velocity and thus an increase in pressure drop. A side-effect that might happen with a reduction in gas nozzles is a less homogeneous mixture supplied to the flame. This less homogeneous mixture will produce temperature variations downstream of the flame, which will travel towards the turbine inlet nozzle. These 'hotspots' are called entropy waves and generate pressure fluctuations at the combustor exit [46]. Those pressure fluctuations will travel back upstream and thus influence and generate an increase in acoustic pressure in the combustion system. It was indicated by Vattenfall that after the reduction to 9 holes, more issues occurred at maximum load. This suggests that the assumption of in-homogeneous mixing is correct. This effect is however not taken into account in the thermo-acoustic model.

Operating parameter	Value
Gas turbine load	Base load - 280 MW
Flame length	62.5 cm
Gas preheating temperature	150°C
$\tau_c$	0.0080 s
$\tau_f$	0.0073 s

Table 7.3: Basic operating conditions for analysis of influence of premix nozzles

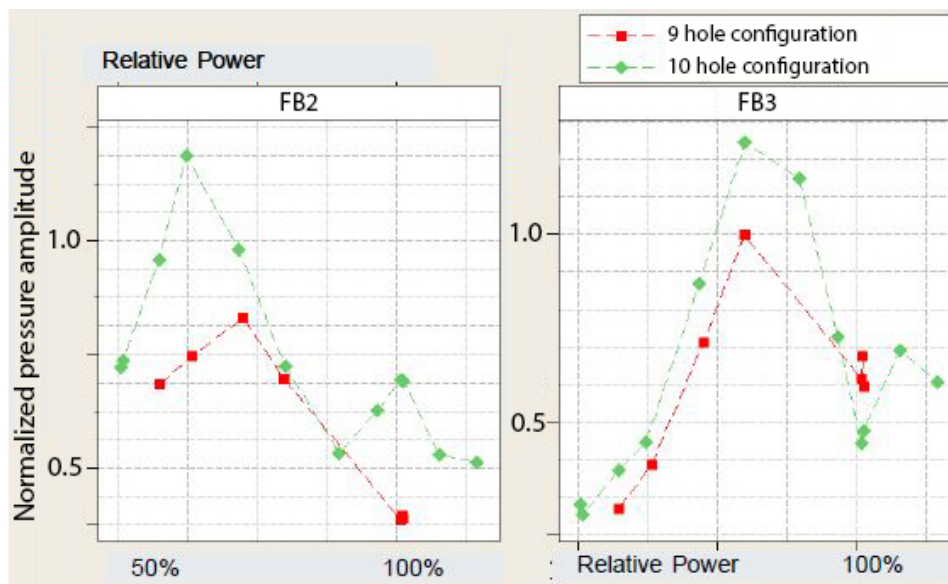


Figure 7.13: Normalized pressure amplitude versus relative power at FB2 and FB3 [41]

### 7.2.1. Gas supply impedance

The impedance of the gas supply will be calculated again using the same method as shown in chapter 5, equations (5.1)-(5.3), with  $p'$  and  $u'$  evaluated at node 6 of figure 5.1. This results in figure 7.14, which shows that for a reduction in fuel nozzles the gas supply impedance increases. This once again indicates that the gas supply will be less susceptible to pressure perturbations, which should result in a decrease in unsteady heat release magnitude for equivalence ratio perturbations. This will not necessarily result in a decrease in reflection factor magnitude, as the previous chapter has shown. The change in gas flow dynamics have shown to also result in phase changes, that will influence the combustion system stability.

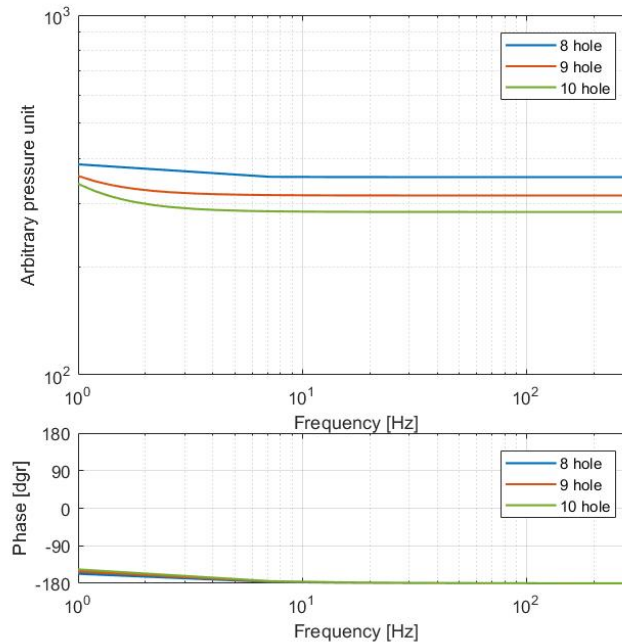


Figure 7.14: Impedance gas supply for different nozzle configurations

### 7.2.2. Unsteady heat release

Using the same method as in the previous chapter, the unsteady heat release is calculated. In figures 7.15 and 7.16 the unsteady heat release due to equivalence ratio fluctuations at different nozzle configurations is shown, both with a gas preheating temperature of 150°C. For the 9 hole configuration it can be seen that the heat release magnitude is lower, as is expected when the increased gas supply impedance is taken into consideration. Around the 50Hz area however, the magnitude of the 9 hole configuration drops below the 8 hole configuration. This can be appointed to the strange phase behaviour that happens around 50Hz for the 10 hole configuration. A steep phase change can be seen around this area, which may indicate that some acoustic effects couple with the unsteady heat release. Further phase responses show equal behaviour with the changes in fuel temperature, which is not surprising as the influence on the gas supply impedance was comparable. Once again for increasing fuel supply impedance, the heat release in 90 Hz seems to increase while around the 120 Hz area seems to decrease. No changes happen in the unsteady heat release due to velocity fluctuations.

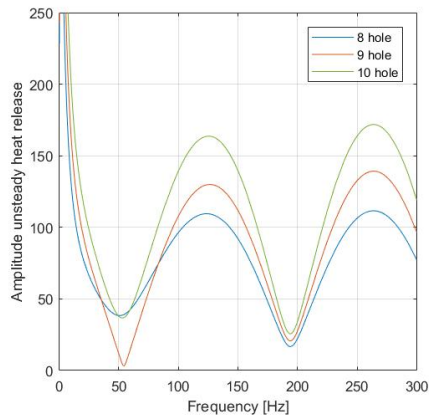


Figure 7.15: Magnitude of unsteady heat release due to equivalence ratio fluctuations

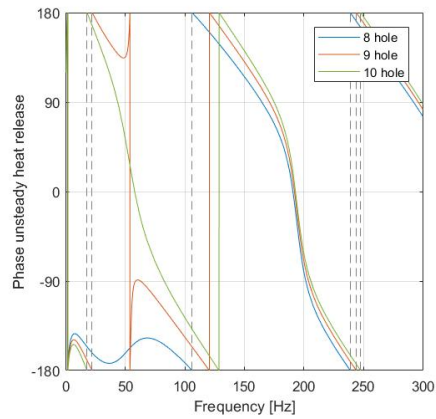


Figure 7.16: Phase of unsteady heat release due to equivalence ratio fluctuations

### 7.2.3. Reflection factor

A look into the reflection factor response shows that the expected response of the system to a change in premix nozzles does happen in the modelled results. The reduction from 10 to 9 nozzles results in increased damping in the 90Hz range, while a further reduction to 8 nozzles results in even more damping. In the 120Hz range, see figure 7.17, the 9 nozzle configuration shows an increased amplification, which was also noticeable in figure 7.13 for base load. The behaviour of the reflection factor corresponds well with the results that were analysed in the previous chapter. An increase pressure drop over the fuel nozzles results in a decrease of 90 Hz humming.

For the higher frequencies there is no data available to validate the assumptions. But the reflection factor responds in an equal manner as it does for the changes to fuel temperature. A reduction in premix nozzles has a comparable response on the gas supply system as an increase in gas preheating temperature, both increasing the flow velocity and pressure drop.

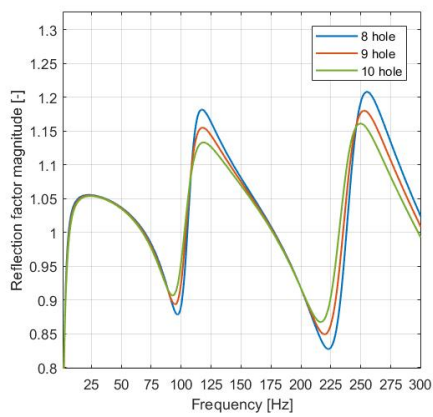


Figure 7.17: Influence of amount of premix gas nozzles on reflection factor magnitude

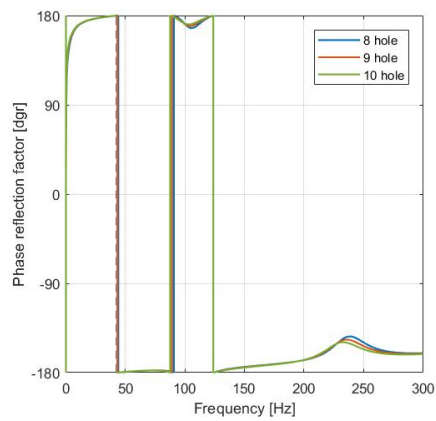


Figure 7.18: Influence of amount of premix gas nozzles on reflection factor phase

### 7.2.4. Stability plot

The stability plot shows the same behaviour as the reflection factor magnitude does. From these results it is easy to see that a reduction in gas nozzles results in a more damped 90 Hz area. Interestingly, the stability in FB5 once again does not respond to a change in pressure drop over the fuel nozzles. It does not have much effect on the third harmonic frequency either, but conclusions on this frequency should be taken carefully, as it was shown that the response at frequencies higher than 200 Hz seem off.

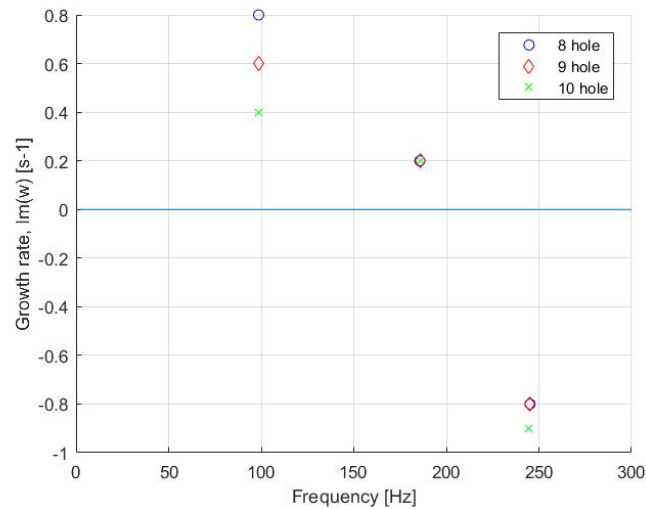


Figure 7.19: Influence of amount of premix gas nozzles on stability

### 7.2.5. Pressure spectra

The pressure spectrum between 80 - 280 Hz shows the three harmonic frequencies again, see figure 7.20. A closer look into the pressure amplitude at these three harmonic frequencies shows a decrease in 90 Hz pressure amplitude for a reduction of gas nozzles, figure 7.21, which is the reason Siemens implemented this. A further reduction to 8 nozzles was mentioned to result in an even further decrease of pressure amplitude, which is also the case. No data is available for the change in pressure amplitude at FB5 and FB7, so the results are hard to validate. The behaviour is however comparable with the results from the fuel temperature change. A decrease in number of gas nozzles has to same effect on the pressure drop over the gas nozzles as an increase in fuel temperature. Which shows in the pressure spectra of FB5, figure 7.22, and of FB7, figure 7.23.

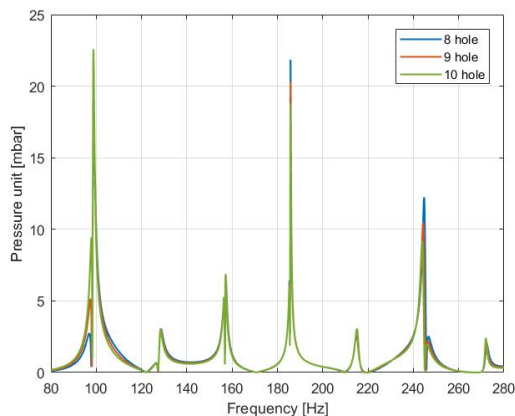


Figure 7.20: Pressure spectrum between 80 - 280 Hz for different nozzle configurations

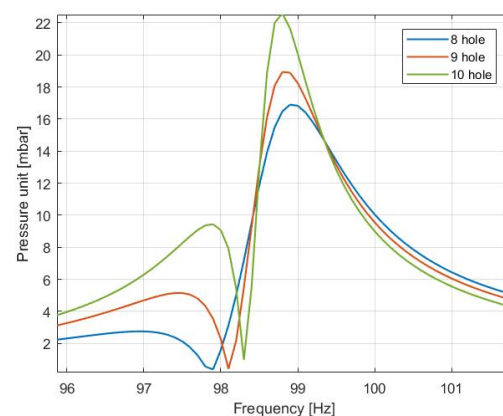


Figure 7.21: Nozzle configuration influence on pressure amplitude in FB2

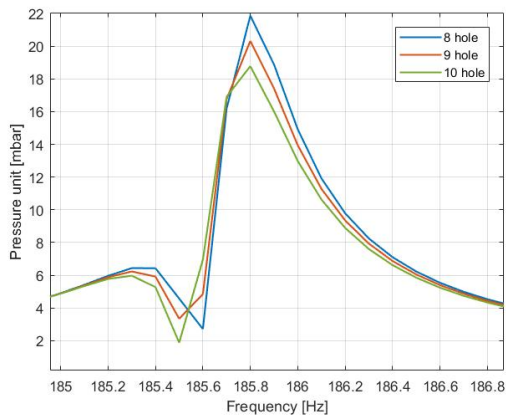


Figure 7.22: Nozzle configuration influence on pressure amplitude in FB5

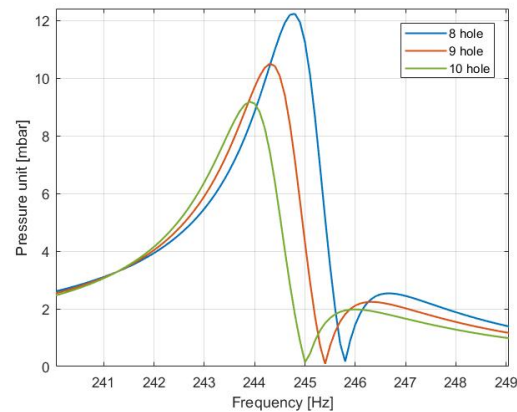


Figure 7.23: Nozzle configuration influence on pressure amplitude in FB7

### 7.2.6. Conclusion and discussion

For the relations that are known between FB2 and FB3 (90Hz and 120Hz), the nozzle reduction responds as expected. A further reduction in nozzles results in further decrease of 90Hz humming, which also corresponds to the expected response. Further relations between frequency bands and the connection with premix nozzles are unknown.

The reduction of nozzles seems to have the same effect as the increase in fuel temperature. Which shows that the combustion system is sensitive to changes in the gas supply system, mainly due to pressure drop over the nozzles. A sensitivity analysis is done on two of the other components of the gas supply system, the resonator volume and the neck length of the resonator, which represents the length of the fuel nozzle. These results are shown in Appendix C. The resonator volume is changed into  $1 m^3$ ,  $10 m^3$  and  $20 m^3$ , but the system response remains exactly equal. The fuel nozzle length is changed into 5 mm, 5 cm and 10 cm. This also does not have any influence on the system response. This leaves the speed of sound in the gas supply system, nozzle area and gas flow velocity to influence the gas supply system. The speed of sound and the gas flow velocity have been shown to have their influence in the previous case study. While this case study shows the influence of the gas flow velocity combined with the nozzle area, as these two are related.

These results together with the results from the premix gas temperature change do also show that the thermoacoustic model can predict the influence of changed operational parameters on the stability of the combustion system. The system responds as expected for the first and second harmonic frequencies, 90 Hz and 180 Hz. The third harmonic frequency does not show the same behaviour, which as mentioned is most likely the result of the compact flame assumption becoming invalid. The reflection factor around the critical frequency of 120 Hz shows the behaviour that is expected in this region. The influence it has on the pressure amplitude can not be investigated since it is no harmonic frequency of the combustion system. The results validate the chosen operational parameters for base load operation and will allow to investigate the response of the combustion system stability to changes to other operational parameters.

### 7.3. Cylindrical burner outlet

An interesting modification by Siemens has been the addition of a cylindrical burner outlet ring to a number of hybrid burners in the annular chamber. This has allowed Siemens to increase the maximum load the gas turbine can achieve without having combustion instability issues. The influence of these rings on the flow field have been shown earlier, but will be repeated here. The focus will be on the difference between the burner flow field without a CBO and the burner flow field with a short CBO, as assumed is that Siemens has chosen the short variant to implement, see figure 7.24. The colors indicate the temperature of the flow field, blue indicating cold and red hot. The arrows indicate velocity vectors, while the black line encircles the re-circulation zone of the flame. The flow field with a burner outlet ring shows to be much more narrow. It is obvious that the flame is elongated as well. With known relationships at base load for regular burners from Siemens, it was determined that the flame length without a burner ring was 62.5 cm. As expected this point is downstream of the re-circulation zone. Translating this towards the flow field with a CBO, a flame length just short of 80 cm is expected. As it is unclear if the flame length increases with the same factor as the re-circulation zone, the system will be analysed for flame lengths of 75 cm, 80 cm and 85 cm.

The CBO was implemented to increase maximum gas turbine load, and thus decreases humming. When looking at operational data, if the gas turbine load is increased the main limitation is the LN23 humming intervention, see equation (4.1c). This suggests that the ratio between the FB2 and FB3 pressure amplitudes turns towards a more dominant FB3 humming. Assumed is that the CBO thus influences these areas, so it either increases FB2 humming or decrease FB3 humming. Seeing as there have been other ways to increase FB2 humming that have proven usefull, the main expectation is to see an increased damping in FB3. The reason why Siemens has not fitted the entire combustion chamber with these changed burners is unknown, but a downside to the combustion dynamics should also be expected.

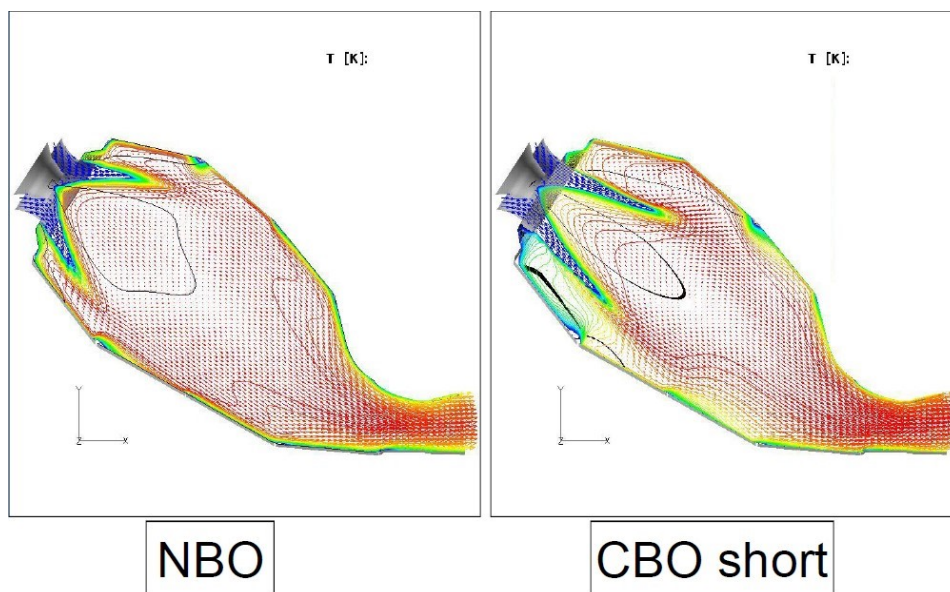


Figure 7.24: Influence of cylindrical burner outlet ring on flow field [22]

Operating parameter	Value
Gas turbine load	Base load - 280 MW
Gas preheating temperature	150°C
Number of premix gas nozzles	9
Flame length	75 - 80 - 85 cm
$\tau_c$	0.01 - 0.0106 - 0.0112s
$\tau_f$	0.0087 - 0.0093 - 0.0099s

Table 7.4: Basic operating conditions for analysis of influence of CBO

### 7.3.1. Cold flow burner impedance

The additional ring on the burner outlet influences the cold flow impedance of the burner that was evaluated in chapter 5. As a reminder, a higher burner impedance is preferred in order to prevent high acoustic velocity fluctuations occurring in the burner system [23]. Figure 7.25 indicates that for frequencies up to 120 Hz the combustion system upstream of the flame becomes less sensitive for velocity fluctuations. However, from 120 Hz upwards the system becomes more sensitive. These results indicate that the CBO functions to stabilize the low frequency areas FB2 and FB3.

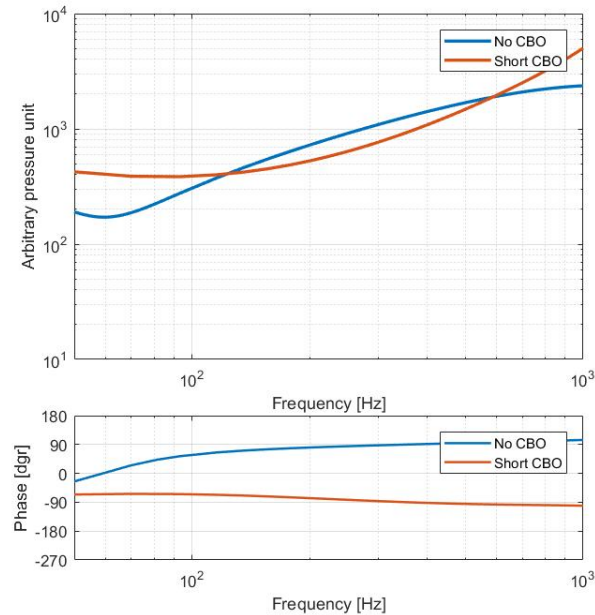


Figure 7.25: Influence of cylindrical burner outlet ring on burner system impedance

### 7.3.2. Unsteady heat release

The change in cold flow burner impedance will result in different pressure fluctuations throughout the entire burner system, which will influence the unsteady heat release. In the figures below, the case that includes a CBO is with a 80cm flame length. The change in behaviour is very obvious, very different behaviour is shown for the heat release due to equivalence ratio fluctuations. From these figures it shows that the heat release when a CBO is fitted on the burner shifts towards the area between 150-200 Hz.

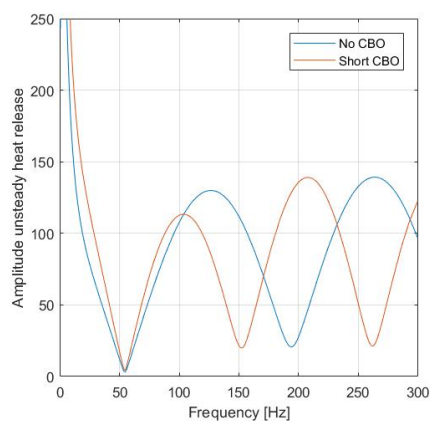


Figure 7.26: Magnitude of unsteady heat release due to equivalence ratio fluctuations

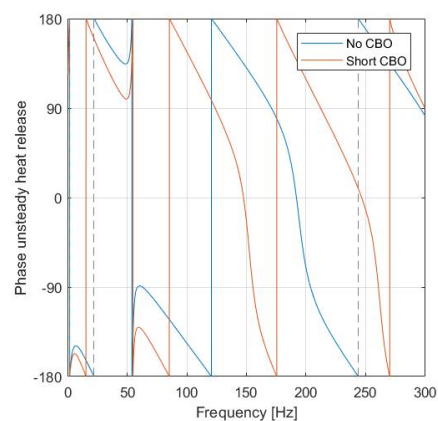


Figure 7.27: Phase of unsteady heat release due to equivalence ratio fluctuations

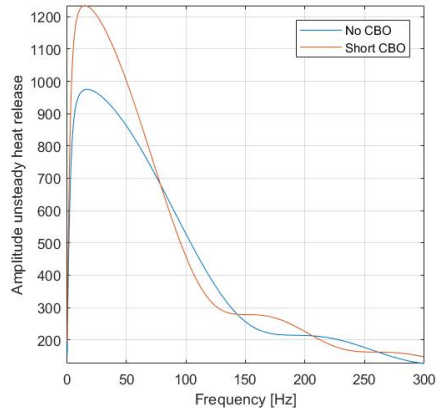


Figure 7.28: Magnitude of unsteady heat release due to velocity fluctuations at the burner mouth

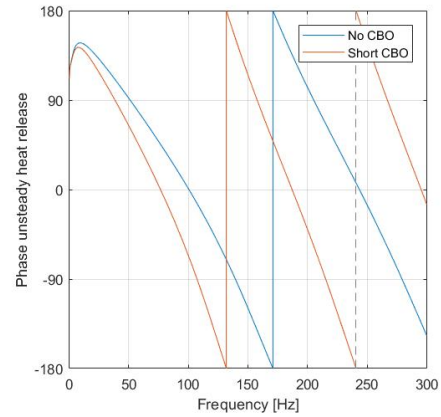


Figure 7.29: Phase of unsteady heat release due to velocity fluctuations at the burner mouth

### 7.3.3. Reflection factor

The magnitude of the reflection factor clearly shows a change in behaviour, see figure 7.30. This can be a coupled effect due to a change in burner impedance, as well as a change in time-delay due to a longer flame and longer convection time in the burner system. Until 75 Hz the system remains fairly even, while the biggest changes happen above 100 Hz. The damping in the 90 Hz range remains almost equal to the no CBO configuration. The maximum in reflection factor magnitude that was previously around 120 Hz has shifted towards the 180 Hz area. This indicates that the influence of the burner outlet shifts away the amplification from the previously critical FB3 towards the FB5 range. As this is an harmonic frequency of the combustion chamber, large amplification in this area can become problematic. This can be the reason Siemens has chosen to not change all hybrid burners to this configuration.

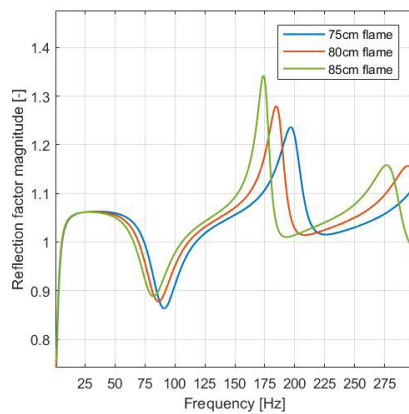


Figure 7.30: Reflection factor magnitude for the CBO burner configuration with different flame lengths

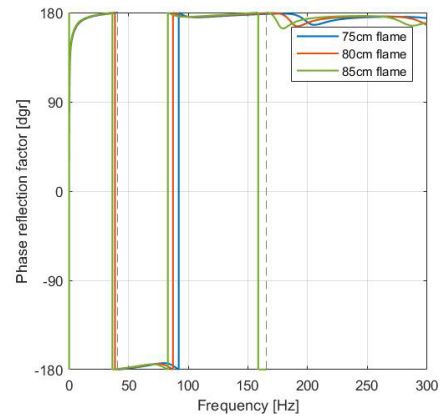


Figure 7.31: Reflection factor phase for the CBO burner configuration with different flame lengths

### 7.3.4. Stability plot

The stability plot shows what could be expected from the analysis of the reflection factor. The stability in FB2 remains, while FB5 changes from stable for no CBO to unstable with a CBO. The third harmonic frequency FB7 also remains unstable, but less so compared to the no CBO configuration.

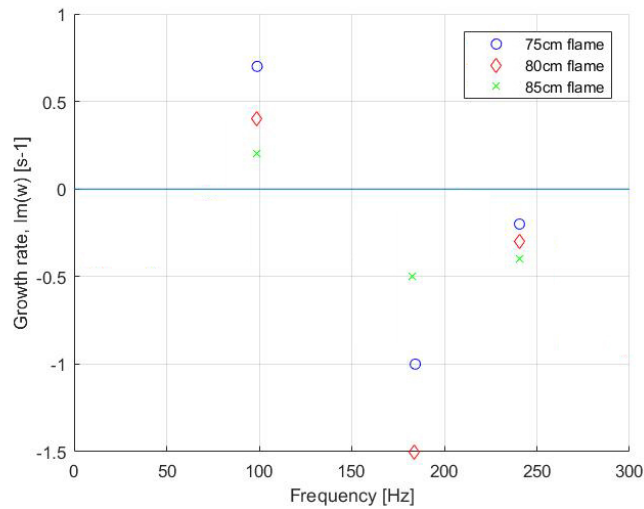


Figure 7.32: Stability plot for the CBO burner configuration with different flame lengths

### 7.3.5. Pressure spectrum

The pressure spectrum shows interesting behaviour. From figure 7.33 it shows that the pressure amplitudes in FB5 and FB7 are much lower than for the case with no CBO. It is however surprising that FB5 becomes much more unstable with a CBO fitted, but this does not reflect in the pressure spectrum. The reflection factor response suggests there is large amplification in this area, especially for the case with the 80 cm flame which shows to be the most unstable. As this pressure spectrum is taken at a single instance of time, it may be the case that when time is included the pressure in FB5 will quickly grow to reach a higher amplitude. The pressure spectrum in the FB2 range does not change much with respect to the no CBO case, which is also what was expected. The fact that the third harmonic frequency, FB7 shows a decrease in pressure amplitude is not surprising either as it shows less amplification for this configuration.

It seems that much more of the resonance in the combustion chamber is shifted to the other frequencies, as the pressure amplitudes at frequencies in between the harmonic frequencies show far higher amplitudes than before the CBO was implemented.

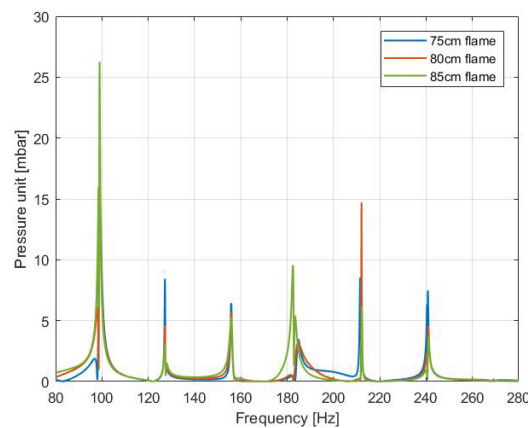


Figure 7.33: Pressure spectrum between 80 - 280 Hz for the CBO burner configuration

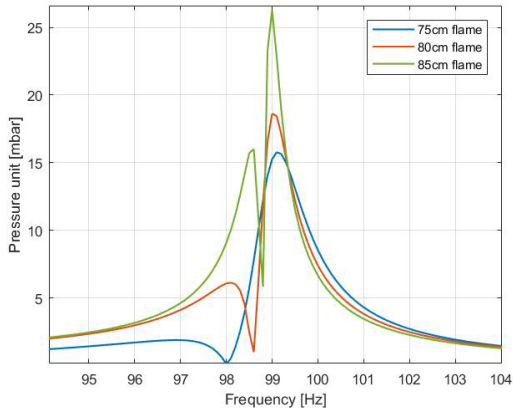


Figure 7.34: Pressure spectrum at FB2 for the CBO burner configuration

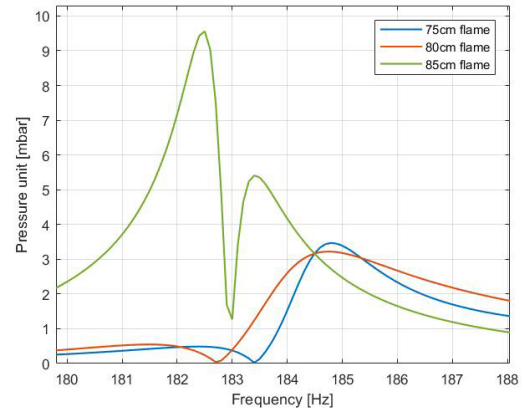


Figure 7.35: Pressure spectrum at FB5 for the CBO burner configuration

### 7.3.6. Conclusion and discussion

The CBO configuration has been used to increase the maximum load of the gas turbine, without having issues with combustion instabilities. This suggests that the critical frequencies at base load, FB2 and FB3, have to be respectively increased or decreased to improve the stability of the system at higher loads. The impedance of the burner system shows that the combustion system upstream of the flame becomes more resilient at low frequencies. This strengthens the hypothesis, as the burner impedance has been validated and has proven to respond to geometrical changes as expected in chapter 5. The reflection factor magnitude also shows the behaviour that is expected at low frequencies up to 180 Hz. It was expected that the critical frequency at 120 Hz would shift due to changes in the convective time delay, and it shows to have shifted towards the 180 Hz area. This area is the second harmonic frequency of the combustion chamber and large amplification in this area could be very dangerous. This looks to be the reason that Siemens has not equipped all of the hybrid burners in the combustion system with this type of burner.

The reflection factor and combustion system stability do however not correspond with the pressure spectrum of the system for the frequencies higher than the first harmonic. It seems that more acoustic energy is present in the frequencies between the harmonic frequencies. Which results in very low pressure amplitudes at the second harmonic frequency, where high(er) pressure amplitudes were expected.

This study shows that the behaviour of a change to burner geometry can be correctly modelled. If correct assumptions are made and the results are critically analysed. The acoustic system impedance, flame reflection factor and system stability are showing behaviour that was expected and respond correctly to changes made to the operational conditions. The pressure spectrum seems off in some cases as the combustion system shows resonance in areas where it is not expected.

## 7.4. Low calorific fuel

With Vattenfall operating two SGT5-4000F gas turbines, one operating on high-calorific fuel and the other one on low-calorific fuel, an interesting analysis can be done on the influence of the fuel composition on the combustion instabilities. The low-calorific gas is supplied from Groningen, the Netherlands. This gas supply is likely to stop in the coming years, which means that the DM34 gas turbine will switch to high-calorific gas, similar to HW09. The difference between these units is the reduced amount of gas nozzles in the HW09 unit. It will be interesting to analyse what the influence of a reduction in gas nozzles is while still operating on low-calorific fuel, as this will provide valuable insight in the way the combustion dynamics will change.

The gas composition input in the model will be changed to low-calorific fuel. The comparison will be made between high-calorific fuel with a 9 nozzle configuration and low-calorific fuel with a 9 and 10 nozzle configuration, at 150°C gas preheating temperature. The assumption is made that for low-calorific fuel the flame length slightly increases, as flame speed is expected to decrease. The steepness of the flame speed as a function of equivalence ratio is assumed to remain equal, as the change in fuel composition is expected to have a negligible influence in this case. The low-calorific fuel Wobbe Index is about 10% lower than for high-calorific fuel. At equal gas turbine load, this suggests that the volumetric flow rate of the low-calorific gas is higher than for high-calorific fuel. This will result in an increase in gas supply impedance.

Operating parameter	Value
Gas turbine load	Base load - 280 MW
Gas preheating temperature	150°C
Number of premix gas nozzles	9 - 10
Flame length	65 cm
$\tau_c$	0.0083s
$\tau_f$	0.0076s

Table 7.5: Basic operating conditions for analysis of influence of low calorific fuel influence

### 7.4.1. Gas supply impedance

The gas supply impedance responds to the different configuration as expected, as the biggest influence on the gas supply is the pressure drop over the fuel nozzles. It shows that the impedance is highest for the low-calorific fuel case with a 9 hole configuration, which is expected as this configuration will have the highest pressure drop over the gas nozzles.

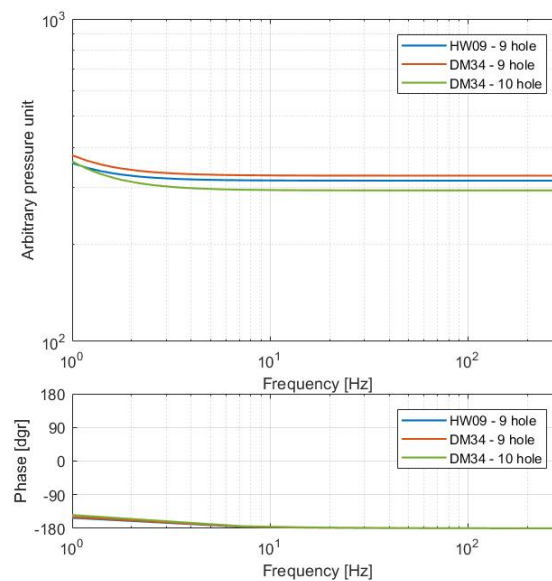


Figure 7.36: Impedance of the gas supply for different configurations

### 7.4.2. Unsteady heat release

The unsteady heat release will be influenced due to changes in gas supply impedance and flame length. The changes in gas supply impedance show to have similar effects as shown before, but the changed convective time delay also influences the unsteady heat release due to equivalence ratio perturbations, see figures 7.37 and 7.38. The unsteady heat release due to velocity fluctuations at the burner mouth is influenced by the change in flame length mostly, this influences the shape factor of the transfer function as well as the time delay. The influence of the time delay is noticeable in figure 7.40, where it shows to shift the response to a lower frequency. The response due to velocity fluctuations remains equal for both nozzle configurations.

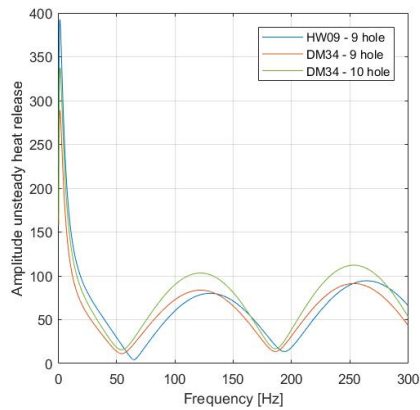


Figure 7.37: Magnitude of unsteady heat release due to equivalence ratio fluctuations

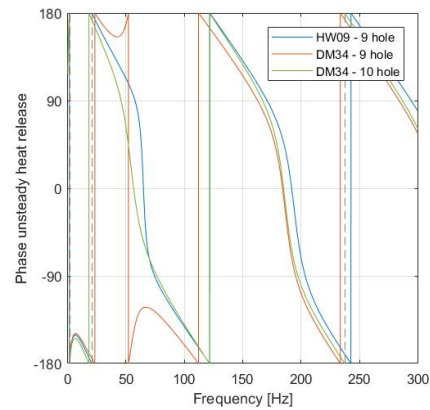


Figure 7.38: Phase of unsteady heat release due to equivalence ratio fluctuations

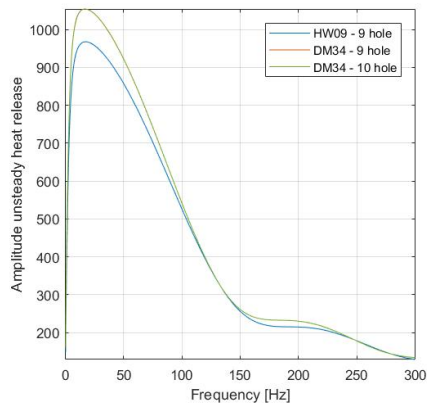


Figure 7.39: : Magnitude of unsteady heat release due to velocity fluctuations at the burner mouth

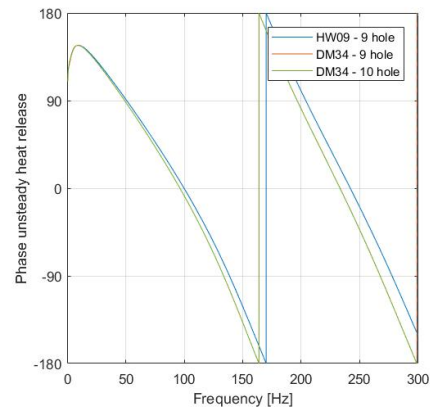


Figure 7.40: Phase of unsteady heat release due to velocity fluctuations at the burner mouth

### 7.4.3. Reflection factor

The changed time delay due to the changed flame length has shifted the reflection factor response to lower frequencies, see figure 7.41. The flame length has not increased much, but the response shows significantly different behaviour. The FB2 range is interesting, as the trough of the reflection factor has shifted to slightly lower frequencies. This indicates that the lower end of the FB2 range becomes more stable, while the upper end of this range becomes more unstable. The 120 Hz range becomes more unstable, which is the critical frequency range for this gas turbine. The same goes for the 240 Hz area, which is known to provide difficulties at low part load operation on high-calorific fuel, but also seems to be more problematic for low-calorific fuel at base load. This is however dependent on the validity of the assumption that the flame is acoustically compact. The phase of the reflection factor in figure 7.42 also shows the shift of behaviour towards lower frequencies for low-calorific fuel. This phase shift is mostly the result of the increase in flame length and slightly influenced by the change in gas dynamics.

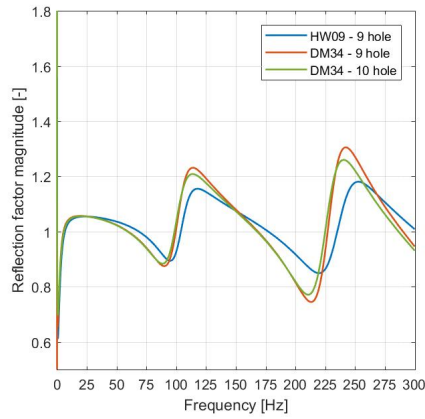


Figure 7.41: Fuel composition influence on reflection factor magnitude

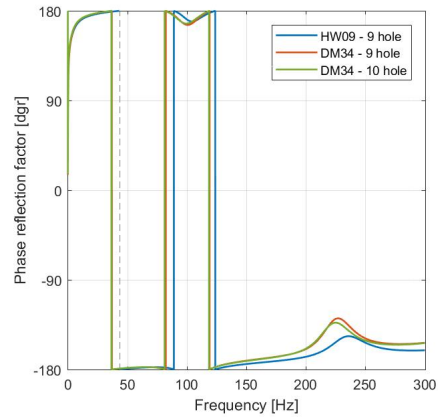


Figure 7.42: Fuel composition influence on reflection factor phase

### 7.4.4. Stability plot

The stability plot for the three harmonic frequencies of the combustion chamber needs to be analysed carefully in combination with the reflection factor response. In the combustion monitoring system the first harmonic frequency shows pressure waves in the frequency range of 80 - 100 Hz. In the modelled combustion system the first harmonic frequency is shifted towards the upper end of this range. If this is the case, the system shows a more unstable first harmonic frequency for low-calorific fuel as opposed to high-calorific fuel, as it does in figure 7.43. But the low-calorific fuel system would be more stable for pressure amplitudes in the lower end of this range, as can be seen from 7.41. This makes it difficult to compare with the high-calorific fuel case. For the second harmonic frequency it is more obvious that the low-calorific fuel shows increased stability in the entire range of observed pressure waves. The same goes for the third harmonic frequency, in that entire range it is more obvious that the low-calorific fuel shows increased amplification.

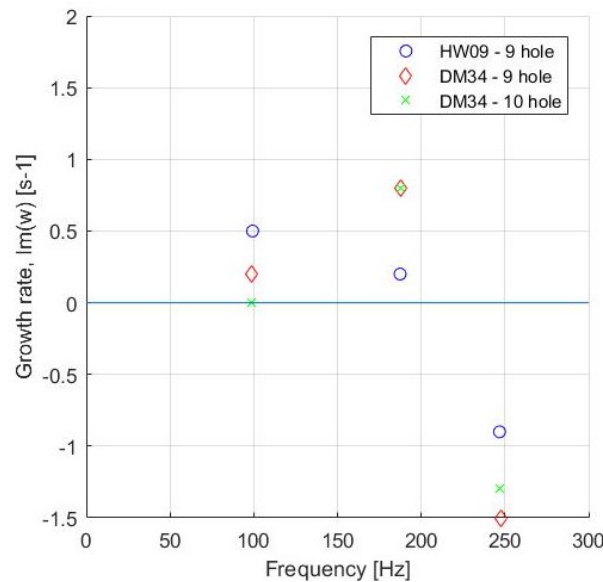


Figure 7.43: Stability plot for low-calorific fuel composition

#### **7.4.5. Conclusion and discussion**

The analysis shows that for a change in fuel composition from high-calorific (HW09) to low-calorific (DM34) in this specific gas turbine, the low-calorific fuel is inherently more unstable. It is difficult to judge the FB2 range, as low-calorific fuel shows to be more stable on the lower end of the range while it is more unstable on the high end of that range. The 120 Hz range however shows to become more unstable, while the 180 Hz range becomes more stable. The fuel supplied to the DM34 unit is unusual and is at the low end of the range of natural gasses. Increased instability in that regard is not unexpected, but the DM34 unit has shown to operate more stable as opposed to the HW09. Further research into the differences between operational data of HW09 and DM34 needs to be done to validate the combustion dynamics of the low-calorific fuel. With the possibility of the low-calorific fuel in DM34 being substituted to high-calorific fuel, the advice based on this analysis is to first change the fuel before the amount of nozzles is reduced. The 9 hole configuration on low-calorific fuel shows to be the most unstable situation in this case, which is something that should definitely be avoided.

## 7.5. Hydrogen addition

With the mention by Siemens that it is possible to operate these combined cycle gas turbines with a 30% volumetric hydrogen substitution, analysis can be done on the influence of hydrogen on the combustion dynamics. The assumption will be made that the burned fuel mixture is still 100% homogeneous. The volumetric flow rate of the gas remains equal, so the gas supply impedance is expected to remain equal as no changes in flow dynamics happen. The change in flame speed as a result of equivalence ratio perturbation,  $\frac{dS_u}{d\phi}$ , is expected to increase significantly, as was shown in figures 2.6 and 2.7. This is adjusted in the model input to show an increased response. Also the flame speed itself will be increasing so a shorter flame is expected. As the exact relationship between flame speed and flame length is unknown, the model inputs will be using a 40cm flame, 45cm flame and 50cm flame.

Operating parameter	Value
Gas turbine load	Base load - 280 MW
Gas preheating temperature	150°C
Number of premix gas nozzles	9
Flame length	40cm - 45cm - 50cm
$\tau_c$	0.0054s - 0.0059s - 0.0065s
$\tau_f$	0.0047s - 0.0052s - 0.0058s

Table 7.6: Basic operating conditions for analysis of influence of hydrogen addition

### 7.5.1. Unsteady heat release

The change to the flame speed, and thus flame length, as well as the increased  $\frac{dS_u}{d\phi}$  shows a distinct change in behaviour in the unsteady heat release due to equivalence ratio fluctuations, see figures 7.44 and 7.45. The peak of the heat release magnitude has shifted towards higher frequencies as compared to the high-calorific fuel cases. The heat release magnitude due to velocity fluctuations has doubled compared to the high-calorific fuel cases, see figures 7.46 and 7.47. Most of this will be due to the changed flame shape factor, due to the different flame length.

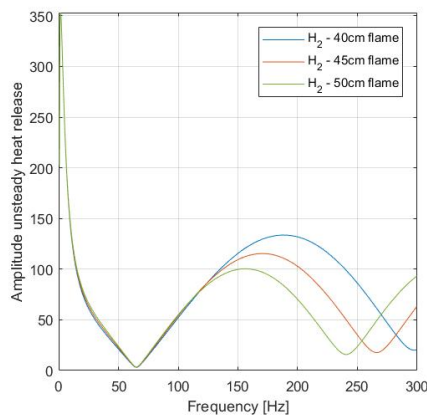


Figure 7.44: Magnitude of unsteady heat release due to equivalence ratio fluctuations

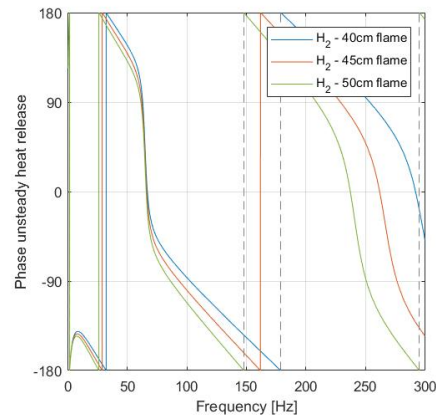


Figure 7.45: Phase of unsteady heat release due to equivalence ratio fluctuations

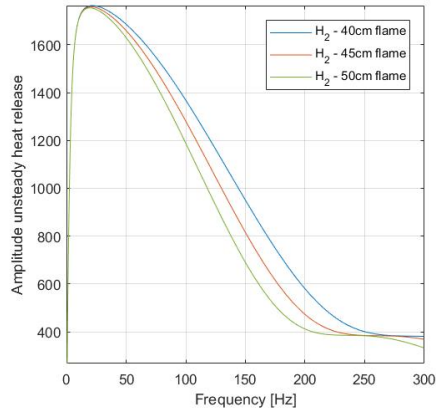


Figure 7.46: Magnitude of unsteady heat release due to velocity fluctuations at the burner mouth

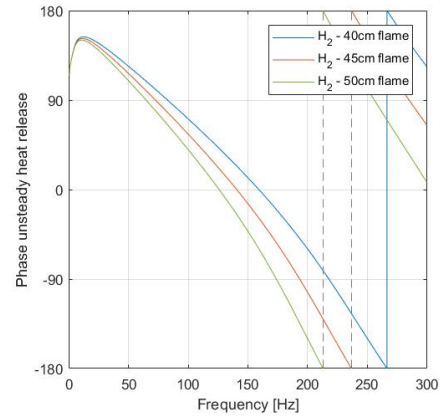


Figure 7.47: Phase of unsteady heat release due to velocity fluctuations at the burner mouth

### 7.5.2. Reflection factor

The reflection factor shows a response that was expected from previous analysis. Longer flame lengths result in larger time delays, which both shifts and contracts the first peak and trough of the reflection factor plot. If the addition of hydrogen would influence the flame such that the flame length becomes 40 cm, it shows that the peak in reflection factor magnitude is around the 180 Hz area, as can be seen in figure 7.48. This is a critical area, as the 180 Hz range corresponds with the second harmonic frequency. Large amplification in the harmonic frequency range of the combustion chamber will result in a very unstable system. The phase of the the reflection factor in figure 7.49 shows a similar pattern for all configurations, with the obvious shift in frequency due to different time delays.

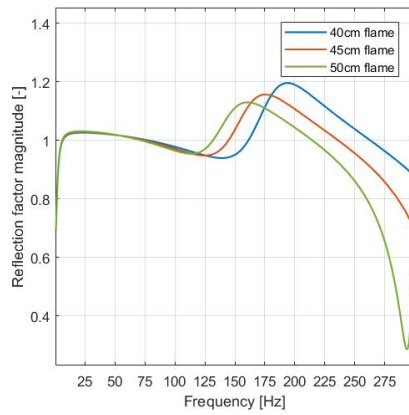


Figure 7.48: Hydrogen addition influence on reflection factor magnitude

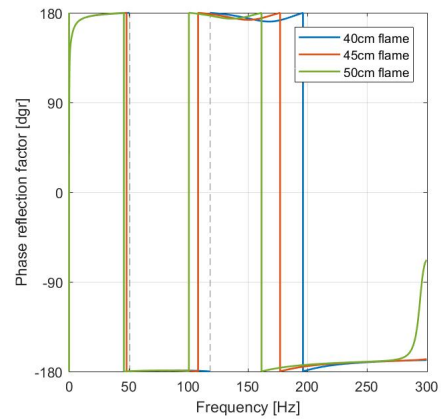


Figure 7.49: Hydrogen addition influence on reflection factor phase

### 7.5.3. Stability plot

The stability plot, figure 7.50, shows that the first harmonic frequency remains stable, but just barely. The second harmonic frequency becomes very unstable for all flame lengths. The third harmonic frequency shows to differ between instability, barely stable and stability. What shows is that the shorter flame length shows to be most unstable for all harmonic frequencies.

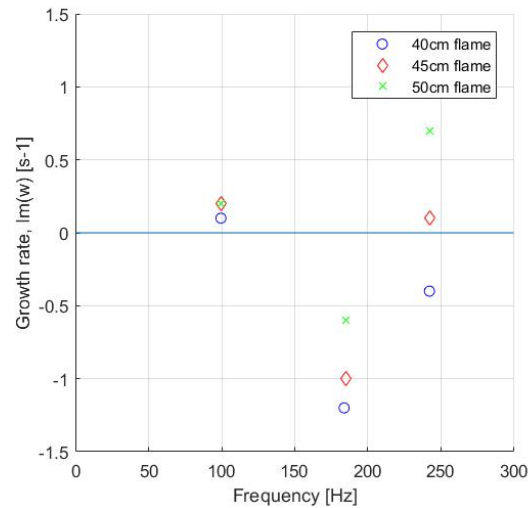
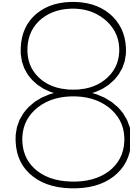


Figure 7.50: Stability plot for hydrogen addition

### 7.5.4. Conclusion and discussion

This analysis touches on a couple of the influences hydrogen addition will have on combustion dynamics. The exact relation between hydrogen addition and these changes is unknown, so the effects that are expected to happen have been exaggerated. In the most extreme case the flame length will decrease by close to 35% as a result of hydrogen addition, this is also the case that shows to be most unstable in all harmonic frequency ranges. The critical frequency shifts from the 120 Hz area, which becomes stable, towards the 180 Hz area. This is the range of the second harmonic frequency, which can result in dangerous and rapidly increasing pressure amplitudes and accelerations. Further research is necessary into the flame speed and combustion dynamics for a mixture of high-calorific natural gas with up to 30% volumetric hydrogen addition. The flame speed and resulting flame length are very important parameters to determine the system stability, as they direct influence the convective time delay of the fluctuating flow parameters.





# Conclusion and recommendations

In this final chapter, the answers to the research questions are discussed and recommendations for further research are provided.

## 8.1. Conclusion

Gas turbines are operated on the limit of their capabilities. Both the gas turbine load and the efficiency of the cycle should be as high as possible, but combustion needs to be lean to adhere to emission restrictions. This is done with a Dry Low NO<sub>x</sub> system that supplies an excess of air into the combustion chamber to keep the flame temperature low, which has a positive effect on NO<sub>x</sub> emissions. This way of operating makes the gas turbine susceptible to combustion instabilities, which occur due to a coupling between unsteady heat release and combustion acoustics. To limit these instabilities, the maximum gas turbine load has to be reduced or the gas preheating temperature decreased, which both have a negative effect on the efficiency and thus power output. To analyse these effects research was done into the combustion instabilities at Vattenfalls powerplant in Amsterdam. The main research objective was stated as:

*What is the impact of operating conditions on thermo-acoustic combustion instabilities in Vattenfalls SGT5-4000F combined cycle gas turbine?*

To assist in answering this research objective, additional research questions were formulated:

- What is the dominant mechanism to drive combustion instabilities?
- How can the (thermo-)acoustic system be modelled?
- What relations exist between physical or operational parameters and combustion instabilities in the SGT5-4000F?
- What is the impact of the fuel composition upon combustion instability?

The driving mechanism for combustion instabilities is the coupling between unsteady heat release and the combustion system acoustics. The dominant mechanisms driving the unsteady heat release are fluctuations of equivalence ratio or fluctuations of mass convected to the flame front. At lean fuel conditions, a small perturbation in equivalence ratio results in a large fluctuation of flame speed, which also results in a change in flame area. An increase or decrease of amount of gas in the supplied mixture also results to a change in the heat content of the fuel. A fluctuation in total mass supplied to the flame also leads to a subsequent increase in flame area, and thus heat release. These effects have been identified as the main drivers for the unsteady heat release and thus combustion instabilities.

Transfer matrices are able to relate (thermo-)acoustic properties when elements are one-dimensionalised and linearised. These assumptions are valid for an acoustically compact system, where characteristic dimensions are significantly smaller than acoustic wavelengths. The identified mechanisms that drive combustion instabilities have been described using this method in a so called flame transfer matrix. The premix burner

geometry of the Siemens SGT5-4000F gas turbine was analysed and also transformed in a transfer matrix model. Coupling both models results in a matrix that is able to describe the combustion behaviour of the burner.

From data analysis and internal documents it was found that several measures by Siemens had been taken to improve stability and limit the occurrence of combustion instabilities. These measures revolved around the pressure drop over the premix gas nozzles. An increase in pressure drop over these nozzles showed to limit the severity of combustion dynamics in the 90 Hz area. However, decreasing the pressure amplitudes in the 90 Hz area too much would result in an increase in amplification at the 120 Hz range, which would make the already critical frequency even more unstable.

Another measure used by Siemens was the addition of a cylindrical burner outlet on several of the 24 burners in the annular combustion chamber. This resulted in an increase in maximum load of the combustion chamber. Changing the outlet of the burner results in a changed flow field of the flame, which changes the convective time-delay of the fluctuations travelling towards the flame. The hypothesis was that this effect would shift the response of these burners away from the critical 120 Hz area.

The fuel composition shows to influence the combustion dynamics mostly due to changes in flame speed and flame speed fluctuations due to equivalence ratio fluctuations. Exact relations between flame speed and flame length have been proven difficult to find, this is also the case for finding a relationship between the fluctuations of equivalence ratio and flame speed. The fact that low-calorific fuel will result in a slightly decreased flame speed and that hydrogen addition would result in increased flame speed was however found. These relationships have allowed to make assumptions on the effects a change in fuel composition would have on flame behaviour.

The thermo-acoustic model showed the expected and analysed response when changes to the pressure drop of the combustion system were done. These were mainly changing the gas preheating temperature or the amount of premix gas nozzles, which influences the gas outflow area. It was shown that increasing the pressure drop does indeed reduce the 90 Hz pressure amplitudes and a side-effect was an increase in amplification around the critical 120 Hz area. From analysis of the influence of fuel preheating temperature it was shown that the pressure amplitude at the second harmonic frequency slightly decreases with a decrease in fuel preheating temperature. This effect was also shown in the pressure spectrum, while the amplification factor of this frequency remained equal for all fuel temperatures. This shows why Siemens suggests that if the FB2 frequency is dominant, the combustion system is stable, as the acoustic pressure amplitudes in other frequency areas decrease while the stability of these frequencies increase. The results of the model seemed to be accurate up to the second harmonic frequency of the combustion chamber. At higher frequencies the results were no longer as expected. At these higher frequencies the assumption of an acoustically compact flame is no longer valid. At frequencies above the second harmonic frequency the assumption should be dropped, which means compressibility and both 2D and 3D effects should be taken into account.

The effect of the cylindrical burner outlet ring was correctly predicted. The characteristics of the burner upstream of the flame showed more resilience towards acoustic fluctuations at lower frequencies. It however became more susceptible at frequencies above the critical 120 Hz frequency. The amplification seemed to shift towards the second harmonic frequency, which suggests to be the reason Siemens has not fitted 24 of these burners. High amplification at the harmonic frequency of the combustion chamber could result in large damages to the combustion chamber. Higher frequencies than the second harmonic frequency are hard to analyse, as the assumption of the compact flame was deemed invalid at these frequencies.

The fuel composition shows to influence the system stability a lot. Mainly the changed flame speed which results in changed flame lengths and convective time-delays changes the combustion behaviour significantly. For increased flame speed with hydrogen addition, the critical frequency shifts towards a higher frequency than the 120 Hz, even towards the second harmonic frequency for the most extreme case. The opposite is true for decreased flame speed at low-calorific fuel, where the instability shifts to slightly decreased frequencies. Exact relations between fuel compositions and flame behaviour are crucial to correctly determine their influence.

Based on the result from the thermo-acoustic model and data analysis, the SGT5-4000F gas turbine seems sensitive at low pressure drop across the premix gas nozzles. A lower pressure drop will increase the 90 Hz acoustic pressure amplitude, which also has its benefits, as a more dominant 90 Hz range should provide a

more stable combustion system. This effect balances on a fine line, as a too low pressure drop can result in very high 90 Hz pressure waves, while a too high pressure results in a more unstable 120 Hz frequency. The cylindrical burner outlets are fitted in the combustion chamber to make the system more resilient at frequencies up to 120 Hz, but are shown to increase the sensitivity for higher frequencies and mostly for the second harmonic frequency. The influence of fuel composition needs further research to correctly determine the flame behaviour. Shifts in crucial frequency areas are however expected, as a change in fuel composition will go hand in hand with changed convective time-delays. Increased flame speed will result in the amplification and instability shifting towards the second harmonic frequency, which should be avoided at all times. The correct response of the thermo-acoustic model to effects seen in analysis from the data of HW09, provides a solid basis for further investigation of the stability of the combustion system. The ability to predict the influence of different operational parameters or changes to burner geometry on the stability of the combustion system can be very beneficial for analysis of future changes to the gas turbine and its operation.

## **8.2. Recommendations**

In this section recommendations are done on points of improvement for the thermo-acoustic model as well as suggestions on further research.

### **8.2.1. Thermo-acoustic model**

#### **Annular combustion chamber**

The combustion chamber in the thermo-acoustic model should be expanded to an annular combustion chamber. Fitting this combustion chamber with 24 burners would allow for analysis of the influence the burners have on one another. This would also allow for further investigation of the effects the CBO has on the acoustic combustion instabilities.

#### **Gas supply system**

The gas supply system has been shown to greatly influence the stability of the combustion system. Currently the gas supply is modelled as a Helmholtz resonator connected to the mixing chamber, with a mean flow coming out of the resonator. Replacing the Helmholtz resonator with a more realistic acoustic system of gas supply piping will be beneficial for the model. Further sensitivity analysis can be done to see what components of the gas supply system also influence the combustion stability.

#### **Part load combustion**

The base parameters for the thermo-acoustic model are validated at base-load operation. More data analysis on part-load operation has to be done to validate new base parameters for the thermo-acoustic model at part load. Frequencies above the second harmonic frequencies are deemed critical at part load, so further analysis of the compact flame assumption needs to be done to determine if this behaviour can be correctly modelled.

#### **Entropy waves**

An additional effect of the reduction of premix gas nozzles might be in-homogeneous mixing when operating at maximum load. This can result in entropy waves, which generate pressure waves at the turbine inlet which influence the combustion acoustics. Including these pressure waves results in a more complete combustion model.

#### **Turbulent flame speed model**

Turbulent flame speeds are difficult to find. There are turbulent flame speed models that relate laminar flame speed to their turbulent counterparts as a function of the turbulence intensity. Incorporating a turbulent flame speed model in the thermo-acoustic model can be a step to further increase the accuracy of the predictions.

## 8.2.2. Further research

### Stability intervention system

A further analysis can be done on the times the stability intervention system has intervened in the operation of the gas turbine. Analysing an additional amount of these events on a selected number of parameters will result in more knowledge of the effect of those parameters on the combustion stability. Verifying these relationships between operational parameters and combustion instabilities allows for further validation of the thermo-acoustic model while also providing better insight into the combustion dynamics.

### Fuel composition

The power plant in Diemen, DM34, is of the same type as the power plant in Amsterdam, HW09. The DM34 power plant is supplied with low-calorific fuel. Changing the fuel inputs in the thermo-acoustic model gave preliminary results based on assumptions of the impact of fuel composition on combustion dynamics. Further data analysis of the DM34 power plant as well as investigation into the exact difference in combustion between higher and lower calorific fuels will provide a basis for further analysis.

### Hydrogen addition

Research is being done on the addition of hydrogen gas to the premixed fuel of gas turbines. Siemens mentioned that without any changes to the gas turbine, 30% of the volumetric flow rate of fuel can be changed to hydrogen. As mentioned this will result in changes in flame speed, flame length and the response to equivalence ratio perturbations. There will be other combustion effects that are influenced by the addition of hydrogen, which need to be researched to provide additional information with the aim for future combustion on hydrogen.

### Flame response

The response of the flame to perturbations in mass burned or equivalence ratio at the flame front is very important to correctly determine the (in)stability of the combustion system. Experiments on the response of the flame originating from the hybrid burner in the SGT5-4000F will provide better insights and allow modification of the flame function in the thermo-acoustic model if required.

# Bibliography

- [1] D. J. Abbott, J. P. Bowers, and S. R. James. The impact of natural gas composition variations on the operation of gas turbines for power generation. In *The Future of Gas Turbine Technology*, Brussels, 2012.
- [2] A. Banerji, J. K. Kurien, M. K. Ashok, M. Balakrishnan, and N. Kishore. Comparative study on the performance and emission characteristics of a diesel engine with internal jet piston using vegetable oil methyl esters. In *International Conference on Emerging Trends in Energy and Environment*, Chennai, India, 2010. URL <https://www.researchgate.net/publication/303994758>.
- [3] D. W. Bechert. Sound absorption caused by vorticity shedding, demonstrated with a jet flow. *Journal of Sound and Vibration*, 70(3):389–405, 1980.
- [4] J. J. Bijlsma. Thermo-acoustic analysis of the GE F9A gas turbine operating at the Eems power plant. Technical report, University of Twente, 2008.
- [5] Sebastian M. Candel. Combustion instabilities coupled by pressure waves and their active control. In *Twenty-fourth Symposium on Combustion*, pages 1277–1296, 1992.
- [6] J. H. Cho and T. C. Lieuwen. Modeling the response of premixed flames to mixture ratio perturbations. In *American Society of Mechanical Engineers, International Gas Turbine Institute, Turbo Expo (Publication) IGTI*, volume 2, pages 67–76, 2003. doi: 10.1115/GT2003-38089.
- [7] H. Cohen, G.F.C. Rogers, and H.I.H. Saravanamuttoo. *Gas Turbine Theory*. Longman Group Limited, 4th edition, 1996. ISBN 0-582-23632-0.
- [8] B. de Jager. *Combustion and noise phenomena in turbulent alkane flames*. PhD thesis, University of Twente, 2007.
- [9] P. Dirrenberger, H. Le Gall, R. Bounaceur, O. Herbinet, P.-A. Glaude, A. Konnov, and F. Battin-Leclerc. Measurements of Laminar Flame Velocity for Components of Natural Gas. Technical Report 9, Nancy Université, 2011. URL <https://hal.archives-ouvertes.fr/hal-00776646>.
- [10] E. Distaso. *Measured and Predicted Particle Number and Mass Emissions from Spark-Ignition Engines*. PhD thesis, Politecnico di Bari, 2016. URL <https://www.researchgate.net/publication/319007325>.
- [11] A. P. Dowling and S. Hubbard. Instability in lean premixed combustors. *Proceedings of the Institution of Mechanical Engineers, Part A: Journal of Power and Energy*, 214(4):317–332, 2000. ISSN 09576509. doi: 10.1243/0957650001537903.
- [12] A. P. Dowling and S. R. Stow. Acoustic Analysis of Gas Turbine Combustors. *Journal of Propulsion and Power*, 19(5):751–764, 2003. doi: 10.2514/2.6192.
- [13] S. Ducruix, T. Schuller, D. Durox, and S. Candel. Combustion Instability Mechanisms in Premixed Combustors. In *Combustion instabilities in Gas Turbine Engines : Operational Experience, Fundamental Mechanism, and Modeling*, chapter 9. Reston, VA : American Institute of Aeronautics and Astronautics, 2005.
- [14] S. Ducruix, D. Durox, and S. Candel. Theoretical and experimental determinations of the transfer function of a laminar premixed flame. *Proceedings of the Combustion Institute*, 28(1):765–773, 9 2007. doi: 10.1016/s0082-0784(00)80279-9.
- [15] M. Fleifil, A. M. Annaswamy, Z. A. Ghoneim, and A. F. Ghoniem. Response of a Laminar Premixed Flame to Flow Oscillations: A Kinematic Model and Thermoacoustic Instability Results. *Combustion and Flame*, 106:487–510, 1996.

- [16] Maria A. Heckl. Active control of the noise from a rijke tube. *Topics in Catalysis*, 124(1):117–133, 1988. ISSN 0022460x. doi: 10.1016/S0022-460X(88)81408-1.
- [17] H. Hermsmeyer, B. Prade, U. Gruschka, U. Schmitz, S. Hoffmann, and W. Krebs. V64.3A Gas turbine natural gas burner development. In *ASME Turbo Expo*, Amsterdam, 2002. URL <http://www.asme.org/about-asme/terms-of-use>.
- [18] J. Hulka and J.J. Hutt. Instability Phenomena in Liquid Oxygen/Hydrogen Propellant Rocket Engines. In V. Young and W.E. Andersen, editors, *Liquid Rocket Engine Combustion Instability*, chapter 2, page 580. American Institute of Aeronautics and Astronautics, 1995. ISBN 9781600864186.
- [19] J.F. van Kampen. *Acoustic pressure oscillations induced by confined turbulent premixed natural gas flames*. PhD thesis, University of Twente, 2006.
- [20] L.V. King. On the convection of heat from small cylinders in a stream of fluid: Determination of the convection constants of small platinum wires, with applications to hot-wire anemometry. *Proceedings of the Royal Society of London. Series A, Containing Papers of a Mathematical and Physical Character*, 90 (622):563–570, 9 1914. doi: 10.1098/rspa.1914.0089.
- [21] S.A. Klein. *On the acoustic of turbulent non-premixed flames*. PhD thesis, University of Twente, 2000.
- [22] W. Krebs and et al. Thermoacoustic design tools and passive means for suppression of combustion dynamics. In *ASME Combustion Dynamics Panel*, 2004. URL <https://www.researchgate.net/publication/288268538>.
- [23] U. Krüger, J. Hüren, S. Hoffman, S. Krebs, P. Flohr, and D. Bohn. Prediction and measurement of thermoacoustic improvements in gas turbines with annular combustion systems. *Journal of Engineering for Gas Turbines and Power*, 123(3):557–566, 7 2001. ISSN 07424795. doi: 10.1115/1.1374437.
- [24] H. Laget, M. Deneve, E. Vanderhaegen, and T. Museur. Combustion dynamics data mining techniques: A way to gain enhanced insight in the combustion processes of fielded gas turbines. In *Proceedings of the ASME Turbo Expo*, volume 2, pages 445–453, 2009. ISBN 9780791848838. doi: 10.1115/GT2009-59553.
- [25] T. Lieuwen. *Investigation of combustion instability mechanisms in premixed gas turbines*. PhD thesis, Georgia Institute of Technology, 1999. URL <https://www.researchgate.net/publication/27535682>.
- [26] T. Lieuwen. Modeling Premixed Combustion-Acoustic Wave Interactions: A Review. *Journal of Propulsion and Power*, 19(5):765–781, 8 2008. ISSN 0748-4658. doi: 10.2514/2.6193.
- [27] T. Lieuwen, V. McDonnell, E. Petersen, and D. Santavicca. Fuel Flexibility Influences on Premixed Combustor Blowout, Flashback, Autoignition, and Stability. *Journal of Engineering for Gas Turbines and Power*, 130(1):011506, 2008. doi: 10.1115/1.2771243.
- [28] M.J. Lighthill. On sound generated aerodynamically I. General theory. *Proceedings of the Royal Society of London. Series A. Mathematical and Physical Sciences*, 211(1107):564–587, 3 1952. doi: 10.1098/rspa.1952.0060.
- [29] M.J. Lighthill. On sound generated aerodynamically II. Turbulence as a source of sound. *Proceedings of the Royal Society of London. Series A. Mathematical and Physical Sciences*, 222(1148):1–32, 2 1954. doi: 10.1098/rspa.1954.0049.
- [30] A. Morones, S. Ravi, D. Plichta, E. L. Petersen, N. Donohoe, A. Heufer, H. J. Curran, F. Güthe, and T. Wind. Laminar and turbulent flame speeds for natural gas/hydrogen blends. In *Proceedings of the ASME Turbo Expo*, volume 4B. American Society of Mechanical Engineers (ASME), 2014. ISBN 9780791845691. doi: 10.1115/GT2014-26742.
- [31] V. Pflug, E. Zindel, G. Zimmermann, O. Rubio Olvera, I. Pyc, and C. Trulley. Power-to-X: The crucial business on the way to a carbon-free world, 2019.
- [32] T. Poinso and D. Veynante. *Theoretical and Numerical Combustion*. R.T. Edwards, inc., 2nd edition, 2005. ISBN 1-930217-10-2.

- [33] W. Polifke. Combustion Instabilities, 2004. URL <https://www.researchgate.net/publication/255738492>.
- [34] W. Polifke and C.O. Paschereit. Suppression of Combustion Instabilities through Destructive Interference of Acoustic and Entropy Waves. In *Sixth international congress on sound and vibration*, Copenhagen, Denmark, 1999. URL <https://www.researchgate.net/publication/255738674>.
- [35] B. Prade, H. Streb, P. Berenbrink, B. Schetter, and G. Pyka. Development of an Improved Hybrid Burner - Initial Operating Experience in a Gas Turbine. In *International Gas Turbine and Aero-engine Congress & Exhibition*, Birmingham, United Kingdom, 1996. URL <https://proceedings.asmedigitalcollection.asme.org>.
- [36] A. Prakash. Prediction of NO<sub>x</sub> Emissions for an RQL Aero-engine Combustor using a Stirred Reactor Modelling Approach. In *AIAA/SAE/ASEE Joint Propulsion Conference*, Salt Lake City, 2016.
- [37] J.L. Rayleigh. The explanation of certain acoustical phenomena 1. pages 319–321, 1878. doi: 10.1038/018319a0.
- [38] S. W. Rienstra and A. Hirschberg. *An Introduction to Acoustics*, 2015.
- [39] Siemens. Argus [Computer Software] - Combustion dynamics monitoring, .
- [40] Siemens. WIN\_TS plus training - Argus humming analysis, .
- [41] Siemens - Confidential. Information regarding potential burner modification, 2016.
- [42] H. Streb, B. Prade, T. Hahner, and S. Hoffmann. Advanced Burner Development for the VX4.3A Gas Turbines. In *ASME Turbo Expo*, New Orleans, USA, 2001. URL <http://www.asme.org/about-asme/terms-of-use>.
- [43] L. C. Valdès and D. Santens. Influence of permanent turbulent air flow on acoustic streaming. *Journal of Sound and Vibration*, 230(1):1–29, 2000. ISSN 0022460X. doi: 10.1006/jsvi.1999.2601.
- [44] J.P. van Buijtenen. Gas Turbines, WB4420 / 4421 Thermodynamics and Gas Turbines, AE3-235, 2007.
- [45] Y. Wu, V. Modica, B. Rossow, and F. Grisch. Effects of pressure and preheating temperature on the laminar flame speed of methane/air and acetone/air mixtures. *Fuel*, 185:577–588, 12 2016. doi: 10.1016/j.fuel.2016.07.110.
- [46] M. Zhu, A. P. Dowling, and K. N.C. Bray. Self-excited oscillations in combustors with spray atomizers. *Journal of Engineering for Gas Turbines and Power*, 123(4):779–786, 10 2001. ISSN 07424795. doi: 10.1115/1.1376717.



# Nomenclature

$\underline{f}$	Momentum generation due to force exerted on fluid	[N/m <sup>3</sup> ]
$A_f$	Flame area	[m <sup>2</sup> ]
$c$	Speed of sound	[m/s]
$c_p$	Specific heat at constant pressure	[J/kg · K]
$c_v$	Specific heat at constant volume	[J/kg · K]
$d_f$	Length of flame zone	[m]
$D_q$	Heat conduction	[W/m · K]
$F$	Transfer function	
$f$	Frequency	[Hz]
$h$	Enthalpy	[J/kg]
$H_f$	Flame transfer function	
$i$	$\sqrt{-1}$	[-]
$k^+$	Wave number of the acoustic wave in the positive axial direction	[1/m]
$k^-$	Wave number of the acoustic wave in the negative axial direction	[1/m]
$L$	Length	[m]
$L_f$	Flame length	[m]
$m$	Mass	[kg]
$Ma$	Mach number	[-]
$P$	Pressure	[Pa]
$p$	Acoustic pressure	[Pa]
$p_i^+$	Complex amplitude of the acoustic wave in positive axial direction at node $i$	[Pa]
$p_i^-$	Complex amplitude of the acoustic wave in negative axial direction at node $i$	[Pa]
$Q$	Heat release	[W]
$q$	Heat release	[W]
$R$	Burner outlet radius	[m]
$R$	Reflection factor	
$S$	Cross sectional area	[m <sup>2</sup> ]
$s$	Entropy	[J/K]
$s, S$	Source term	[kg/s]

$S_u$	Flame speed	[m/s]
$St$	Strouhal number	[-]
$T$	Temperature	[K]
$t$	Time	[s]
$u$	Flow velocity	[m/s]
$V$	Volume	[m <sup>3</sup> ]

### Abbreviations

CBO	Cylindrical burner outlet
CCGT	Combined cycle gas turbine
DLN	Dry Low NO <sub>x</sub>
DM34	Diemen 34 power plant, Diemen
FB	Frequency band
FTF	Flame transfer function
HBR	Hybrid burner ring
HW09	Hemweg 9 power plant, Amsterdam
OTC	Outlet temperature calculated
SGT5-4000F	Gas turbine type
TIT	Turbine inlet temperature

### Greek symbols

$\beta$	Flame geometry factor	
$\beta$	Heat transfer from heating gauze to perpendicular air flow	[W]
$\gamma$	Ratio of specific heats	[-]
$\kappa$	Heat conductivity	[W/(m·K)]
$\lambda$	Wave length	[m]
$\omega$	Frequency	[rad/s]
$\phi$	Fuel-air equivalence ratio	[-]
$\rho$	Density	[kg/m <sup>3</sup> ]
$\rho_e$	Excess density	[kg/m <sup>3</sup> ]
$\tau$	Time delay	[s]
$\zeta$	Damping factor	[-]
$\underline{\underline{\tau}}$	Viscous stress tensor	[kg/s <sup>2</sup> ·m]

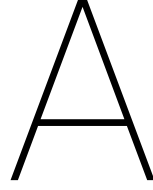
### Operators

$\cdot$	Time dependent
$'$	(Acoustic) Fluctuation

**Subscripts**

0	Far field variable
7,FB2	Measured at burner flange 7 in frequency band 2
a	At the air inlet in mixing chamber
air	Property of air flow
b	At the burner outlet
c	Property of cold flow
f	At the flame front
f	At the mixing location
fg	Property of flue gas flow
g	At the gas inlet in mixing chamber
gas	Property of gas flow
h	Property of hot flow
stp	Property at standard temperature and pressure





## Thermo-acoustic source term

In this chapter it is shown how the thermo-acoustic source term of the flame is derived. It will show how the LHS of equation (A.1) is transformed into the RHS of equation (A.1).

$$\frac{\partial^2}{\partial t^2} \left( \frac{p'}{c_0^2} - \rho' \right) = \frac{\partial}{\partial t} \left[ \frac{\gamma - 1}{c^2} q' \right] \quad (\text{A.1})$$

The starting point is a thermodynamic relationship between pressure, density and entropy:

$$\frac{Dp}{Dt} = \frac{\partial p}{\partial \rho} \Big|_s \frac{D\rho}{Dt} + \frac{\partial p}{\partial s} \Big|_\rho \frac{Ds}{Dt} \quad (\text{A.2})$$

This equation will be simplified by transforming both partial derivatives. The first partial derivative can be rewritten in terms of the speed of sound at the source location:

$$\frac{\partial p}{\partial \rho} \Big|_s = c_s^2 \quad (\text{A.3})$$

The second partial derivative will be rewritten using thermo-dynamic relationships for an ideal gas. First this partial derivative is simplified:

$$\frac{\partial p}{\partial s} \Big|_\rho = \frac{\frac{\partial p}{\partial T} \Big|_\rho}{\frac{\partial s}{\partial T} \Big|_\rho} \quad (\text{A.4})$$

Using the relationships for an ideal gas, this can be further simplified.

$$p = \rho RT \quad (\text{A.5a})$$

$$\frac{\partial p}{\partial T} \Big|_\rho = \rho R \quad (\text{A.5b})$$

$$ds = \frac{c_v}{T} dT + p \frac{d}{d\rho} \quad (\text{A.6a})$$

$$\frac{\partial s}{\partial T} \Big|_\rho = \frac{c_v}{T} \quad (\text{A.6b})$$

Combining equation (A.2), equation (A.3) and equation (A.4), while also linearising this equation results in:

$$\frac{Dp'}{Dt} = c_s^2 \frac{D\rho'}{Dt} + \frac{\rho TR}{c_v} \frac{Ds'}{Dt} \quad (\text{A.7})$$

This is rewritten by dividing all terms by  $c_0^2$ , which is the speed of sound at the observer location, after which  $\frac{D\rho'}{Dt}$  is subtracted from both sides of the equation, which results in:

$$\frac{D}{Dt} \left( \frac{p'}{c_0^2} - \rho' \right) = \left( \frac{c_s^2}{c_0^2} - 1 \right) \frac{D\rho'}{Dt} + \frac{\rho TR}{c_v c_0^2} \frac{Ds'}{Dt} \quad (\text{A.8})$$

The negative of the term inside the brackets of the LHS of equation (A.8) is what is called the excess density,  $\rho_e = (\rho' - \frac{p'}{c_0^2})$ . The excess density can be substituted into equation (A.8):

$$-\frac{D\rho'_e}{Dt} = \left( \frac{c_s^2}{c_0^2} - 1 \right) \frac{D\rho'}{Dt} + \frac{\rho TR}{c_v c_0^2} \frac{Ds'}{Dt} \quad (\text{A.9})$$

The term on the LHS represents the material derivative of the excess density, which is equal to:

$$\frac{D\rho'_e}{Dt} = \frac{\partial \rho'_e}{\partial t} + \underline{u} \nabla \cdot \rho'_e = \frac{\partial \rho'_e}{\partial t} + \nabla \cdot (\underline{u} \rho'_e) - \rho'_e \nabla \cdot \underline{u} \quad (\text{A.10})$$

The excess density satisfies the mass conservation equation, so the material derivative of the continuity equation (A.11) can be used to transform the last term of equation (A.10).

$$\frac{D\rho}{Dt} = -\rho(\nabla \cdot \underline{u}) \quad (\text{A.11a})$$

$$\nabla \cdot \underline{u} = -\frac{1}{\rho} \frac{D\rho}{Dt} \quad (\text{A.11b})$$

Combining this with equation (A.10) results in:

$$\frac{D\rho'_e}{Dt} = \frac{\partial \rho'_e}{\partial t} + \nabla \cdot (\underline{u} \rho'_e) + \frac{\rho'_e}{\rho} \frac{D\rho}{Dt} \quad (\text{A.12})$$

This result can be used in equation (A.9), which results in:

$$\frac{\partial \rho'_e}{\partial t} + \nabla \cdot (\underline{u} \rho'_e) + \frac{\rho'_e}{\rho} \frac{D\rho}{Dt} = \left( \frac{c_s^2}{c_0^2} - 1 \right) \frac{D\rho'}{Dt} + \frac{\rho TR}{c_v c_0^2} \frac{Ds'}{Dt} \quad (\text{A.13})$$

The first term in equation (A.1) is equal to  $-\frac{\partial^2 \rho'_e}{\partial t^2}$ . So equation (A.13) needs to be rewritten as a function of the partial derivative with respect to time of the excess density:

$$-\frac{\partial \rho'_e}{\partial t} = \left( \frac{c_s^2}{c_0^2} - 1 + \frac{\rho'_e}{\rho} \right) \frac{D\rho'}{Dt} + \frac{\rho TR}{c_v c_0^2} \frac{Ds'}{Dt} + \nabla \cdot (\underline{u} \rho'_e) \quad (\text{A.14})$$

To get to the term for the monopole source term, the time-derivative of equation (A.14) has to be taken.

$$-\frac{\partial^2 \rho'_e}{\partial t^2} = \frac{\partial}{\partial t} \left[ \left( \frac{c_s^2}{c_0^2} - 1 + \frac{\rho'_e}{\rho} \right) \frac{D\rho'}{Dt} + \frac{\rho TR}{c_v c_0^2} \frac{Ds'}{Dt} + \nabla \cdot (\underline{u} \rho'_e) \right] \quad (\text{A.15})$$

If the ideal gas is assumed to have a constant heat capacity  $(\frac{c_s^2}{c_0^2} - 1 + \frac{\rho'_e}{\rho})$  is equal to zero. Dimensional analysis by Van Kampen [19] has shown that the third term on the RHS of equation (A.15) can be neglected. This term  $\nabla \cdot (\underline{u} \rho'_e)$  is a source term for sound generation by density fluctuations, while the term  $\frac{\rho TR}{c_v c_0^2} \frac{Ds'}{Dt}$  is due to sound generation by combustion. The sound generation by combustion is  $\mathcal{O}(Ma^{-2})$  stronger than the sound generation by density fluctuations, so the last one is discarded. This results in the following equation:

$$-\frac{\partial^2 \rho'_e}{\partial t^2} = \frac{\partial}{\partial t} \left[ \frac{\rho TR}{c_v c_0^2} \frac{Ds'}{Dt} \right] \quad (\text{A.16})$$

The term  $\frac{Ds'}{Dt}$  can be rewritten in terms of heat release perturbations  $\frac{q'}{\rho T}$ , this results in:

$$-\frac{\partial^2 \rho'_e}{\partial t^2} = \frac{\partial}{\partial t} \left[ \frac{R}{c_v c_0^2} q' \right] \quad (\text{A.17})$$

The ideal gas law allows  $R$  to be rewritten as  $c_p - c_v$ , which can be used to rewrite  $\frac{R}{c_v c_0^2}$ , which also uses  $\gamma = \frac{c_p}{c_v}$ :

$$-\frac{\partial^2 \rho'_e}{\partial t^2} = \frac{\partial}{\partial t} \left[ \frac{(\frac{c_p}{c_v} - \frac{c_v}{c_v}) c_v}{c_v c_0^2} q' \right] = \frac{\partial}{\partial t} \left[ \frac{\gamma - 1}{c_0^2} q' \right] \quad (\text{A.18})$$

This term can now be substituted in equation (2.9) to get to the wave equation (2.10):

$$\frac{1}{c_0^2} \frac{\partial^2 p'}{\partial t^2} - \nabla^2 p' = \frac{\partial}{\partial t} \left[ \frac{\gamma - 1}{c^2} q' \right] \quad (\text{A.19})$$



# B

## Fuel temperature influence

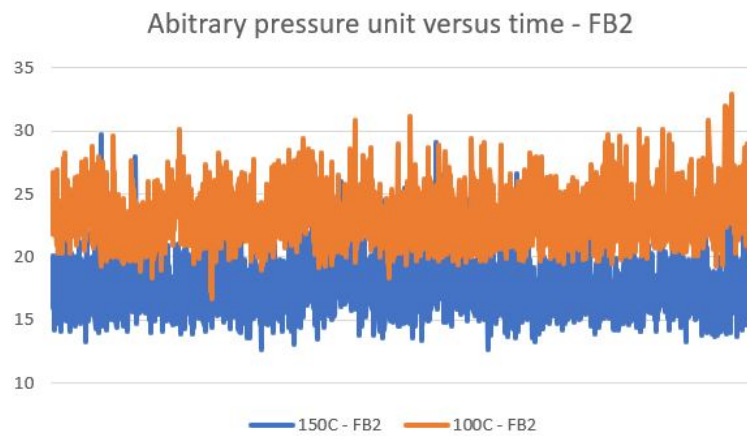


Figure B.1: Change in acoustic pressure amplitude as a result of gas preheating temperature reduction - FB2

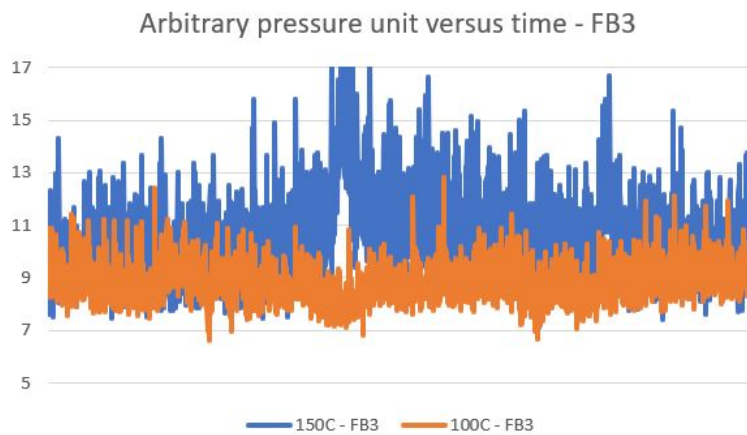


Figure B.2: Change in acoustic pressure amplitude as a result of gas preheating temperature reduction - FB3

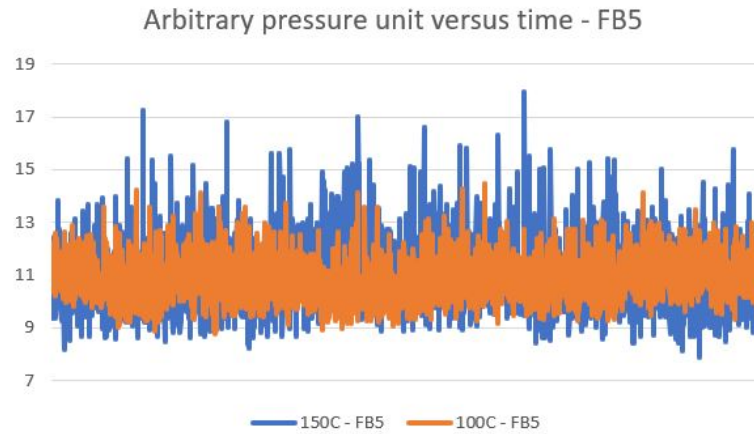


Figure B.3: Change in acoustic pressure amplitude as a result of gas preheating temperature reduction - FB5

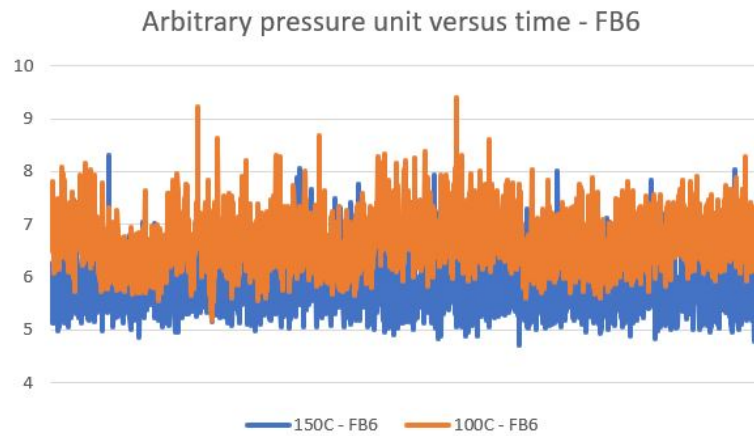


Figure B.4: Change in acoustic pressure amplitude as a result of gas preheating temperature reduction - FB6

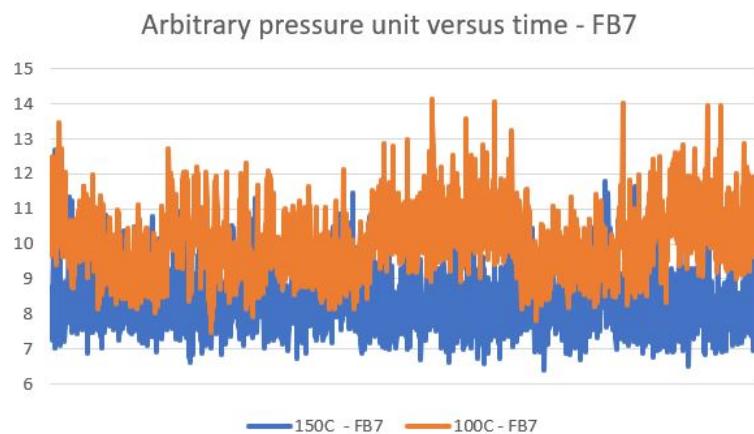


Figure B.5: Change in acoustic pressure amplitude as a result of gas preheating temperature reduction - FB7

# C

## Fuel supply sensitivity

It was noticed that the fuel supply system, mainly the pressure drop over the nozzles, had a big influence on the combustion dynamics. To see if any of the other factors had an influence, a sensitivity analysis has been performed. The gas supply is modelled as a Helmholtz resonator, using the following transfer matrix, which was derived in chapter 2.5, equation (2.58). In this equation there are 5 factors that influence the fuel supply. These are the resonator volume  $V_1$ , the length of the fuel piping  $L$ , the speed of sound  $c_2$ , the flow velocity  $u_2$  and the cross sectional area of the fuel outlet  $S_2$ . The last two are related to one another, and have been shown to influence the combustion dynamics in case study 7.2.  $u_2$  and  $c_2$  have been shown to also influence the combustion dynamics, as they are both influenced by the gas preheating temperature, of which the influence has been analysed in case study 7.1. The only two that remain to be analyzed are the volume and the length of the fuel piping. The resonator volume is changed into  $1 \text{ m}^3$ ,  $10 \text{ m}^3$  and  $20 \text{ m}^3$ . The fuel nozzle length is changed into 5 mm, 5 cm and 10 cm.

$$\begin{bmatrix} 1 & 1 & -\frac{c^2 S_2}{i\omega V_1 c_2} & \frac{c^2 S_2}{i\omega V_1 c_2} \\ -S_2 & -S_2 & \frac{i\omega L S_2}{c^2} + \frac{2S_2 u_2}{c_2} + S_2 & -\frac{i\omega L S_2}{c^2} - \frac{2S_2 u_2}{c_2} + S_2 \end{bmatrix} \cdot \begin{bmatrix} p_1^+ \\ p_1^- \\ p_2^+ \\ p_2^- \end{bmatrix} = \mathbf{0} \quad (\text{C.1})$$

### Resonator volume

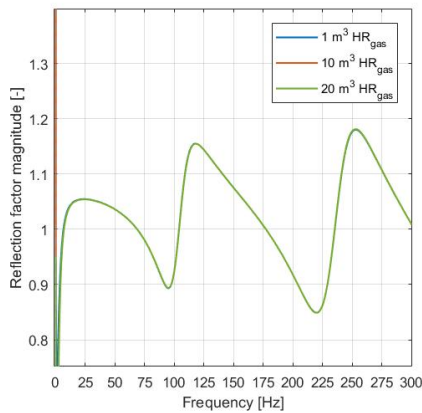


Figure C.1: Reflection factor magnitude for different Helmholtz resonator volumes

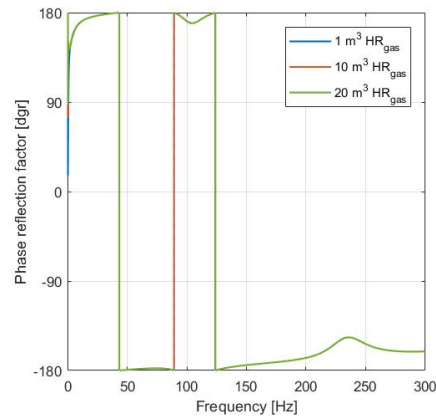


Figure C.2: Reflection factor phase for different Helmholtz resonator volumes

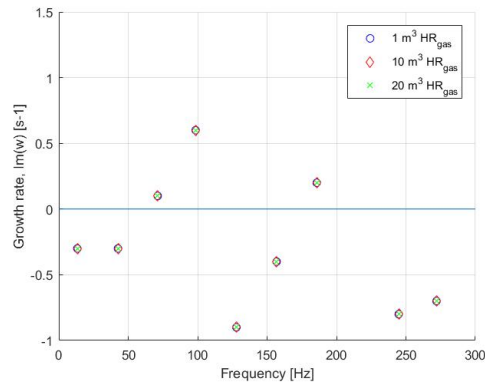


Figure C.3: System stability for different Helmholtz resonator volumes

## Fuel piping length

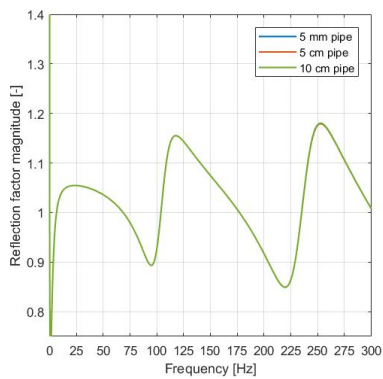


Figure C.4: Reflection factor magnitude for different fuel piping lengths

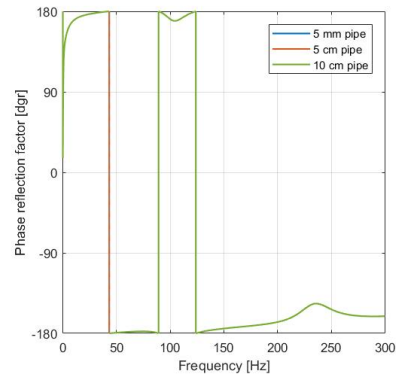


Figure C.5: Reflection factor phase for different fuel piping lengths

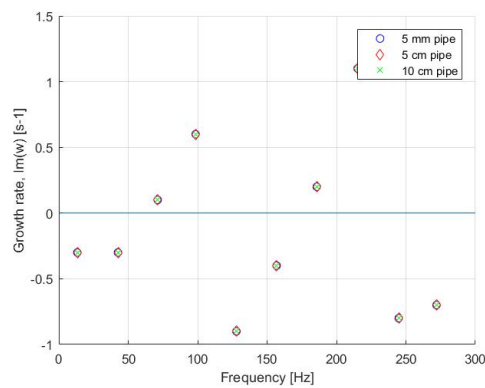


Figure C.6: System stability for different fuel piping lengths

## Conclusion

Neither of these two parameters have any influence on the combustion system response, it remains exactly the same. This suggests that the speed of sound, nozzle cross sectional area and gas flow velocity are the parameters that influence the fuel supply system.



# Acoustics of a clarinet

## Introduction

To test the Transfer Matrix Method, a simple model of a clarinet will be described, modelled and analysed, with the idea coming from Bijlsma [4] but the model being different. The clarinet will have a total length ( $L_{cl}$ ) of 1.00 m and a diameter which will be constant along its length. The left side of the clarinet will have a closed end, while the right side of the clarinet will be an open end. Since the clarinet will be modelled as a simple cylindrical duct, the resonance frequencies can be calculated by hand, which allows the validation of the solution methods to find the resonance frequencies. Assuming that the clarinet is used at an average room temperature of around 20°C, the speed of sound ( $c$ ) will be approximately 343 m/s. The first couple of resonance frequencies can be calculated from the corresponding wave length and the speed of sounds, using equation (D.1).

$$f = \frac{c}{\lambda} \tag{D.1}$$

	Wave length [m]	Frequency [Hz]
1 <sup>st</sup>	$L_{cl} \cdot 4 = 4,00$ [m]	85,75
2 <sup>nd</sup>	$L_{cl} \cdot \frac{4}{3} = 1,33$ [m]	257,25
3 <sup>rd</sup>	$L_{cl} \cdot \frac{4}{5} = 0,80$ [m]	428,75

Table D.1: First resonance/eigenfrequencies for the clarinet

## Acoustic network model

The clarinet will be split up in to 7 different cylindrical duct elements, all varying in length, with a total length of 1.00 m. This can be represented in a so called acoustic network model. Each cylindrical duct element has an input and output node, which are numbered 1 through 8. All cylindrical duct elements connecting to nodes are numbered using roman numbers, I through VII. A mass flow source is present at node 3, this is assumed to be the node where air is blown into the clarinet.

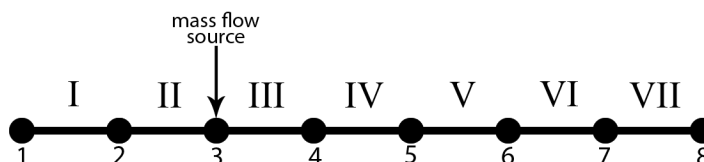


Figure D.1: Acoustic network model clarinet

For each element, the matrix for the cylindrical duct element (2.30) is used in the total system matrix. The only cylindrical duct element that will differ is the one for element III, in which a mass flow source term

will be present, see equation D.2. This source term has an arbitrarily chosen value and functions as a passive source of sound. Node 1 and node 8 will also have a boundary condition, corresponding with a closed and an open end, respectively. So in this case the boundary elements (2.61) and (2.63) will be used.

$$\begin{bmatrix} e^{-ik^+L_{III}} & 0 & -1 & 0 \\ 0 & e^{ik^-L_{III}} & 0 & -1 \end{bmatrix} \cdot \begin{bmatrix} p_3^+ \\ p_3^- \\ p_4^+ \\ p_4^- \end{bmatrix} = \begin{bmatrix} 1 \cdot 10^{-7} \\ 0 \end{bmatrix} \quad (\text{D.2})$$

## Eigenfrequencies of the clarinet

With the model now being complete, the eigenfrequencies can be found using Matlab. All elements are put into one (square) matrix, this allows us to calculate the determinant of this matrix as a function of the frequency ( $f$ ). The eigenfrequencies are all values of  $f$  for which the matrix determinant equals 0. The solution of this equation will provide a complex frequency of the form  $f + i \cdot \alpha$ . In this form, the real part of the frequency is the actual eigenfrequency, while the imaginary part,  $\alpha$ , provides a picture of the stability of the system. For negative values of  $\alpha$  the system is unstable, which means pressure waves will increase over time, while for positive values of  $\alpha$  the system remains stable.

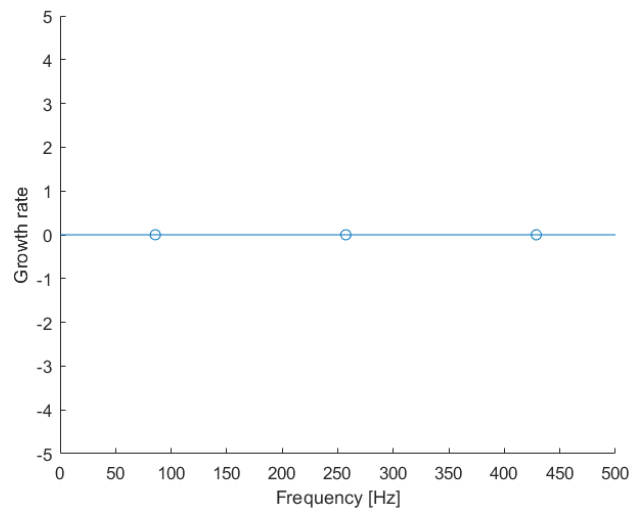


Figure D.2: Eigenfrequencies of the clarinet

The eigenfrequencies for the clarinet are plotted in figure D.2. This figure shows that there are eigenfrequencies found at 85.75, 257.25 and 428.75 Hz, which are exactly equal to those frequencies calculated by hand, using equation (D.1). So this method of solving the transfer matrix to find eigenfrequencies for a simple system works. The eigenfrequencies that are found all have an imaginary part that is equal to zero, so this means that the found eigenfrequencies are stable. This can be explained by the fact that there is no feedback-loop present in the clarinet. With a feedback-loop, pressure perturbations that are present in the clarinet will influence the acoustics of the clarinet. If an excited pressure perturbation influences the acoustic of the system, this can show either damping or an increase of the excited pressure perturbation. Because there is no such loop implemented in this clarinet, the eigenfrequencies will be stable.

## Acoustic pressure spectrum

The matrix system can also be solved, using equation (D.3) and (D.4) to provide the positive and negative travelling pressure waves at each node. Solving this allows a plot to be made of the pressure spectrum at each node versus the frequency. The eigenfrequencies should also show in these plots.

$$[A] \cdot \mathbf{p} = \mathbf{S} \quad (\text{D.3})$$

$$\mathbf{p} = [A]^{-1} \cdot \mathbf{S} \quad (\text{D.4})$$

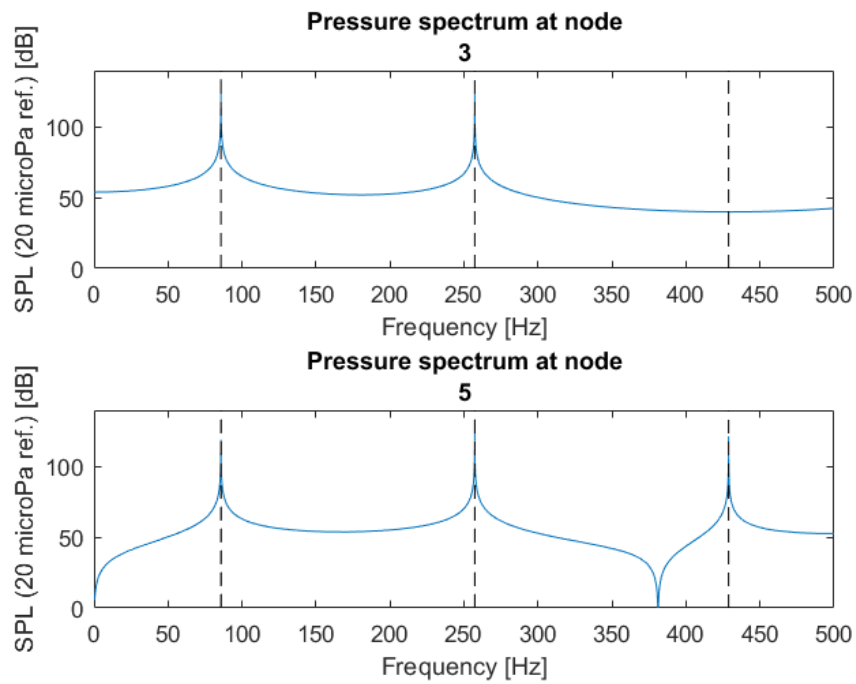


Figure D.3: Pressure spectrum at node 3 and 5 of the clarinet

Only 2 distinct resonance peaks can be seen in the pressure spectrum at node 3, while the pressure spectrum at node 5 shows a peak for all found eigenfrequencies. As the pressure perturbation travels in wave form, an explanation might be that the resonance frequency of 428.75 Hz has a minimum at node 3. The normalized pressure fluctuations can be calculated and plotted, these should provide an explanation for the missing resonance peak at node 3.

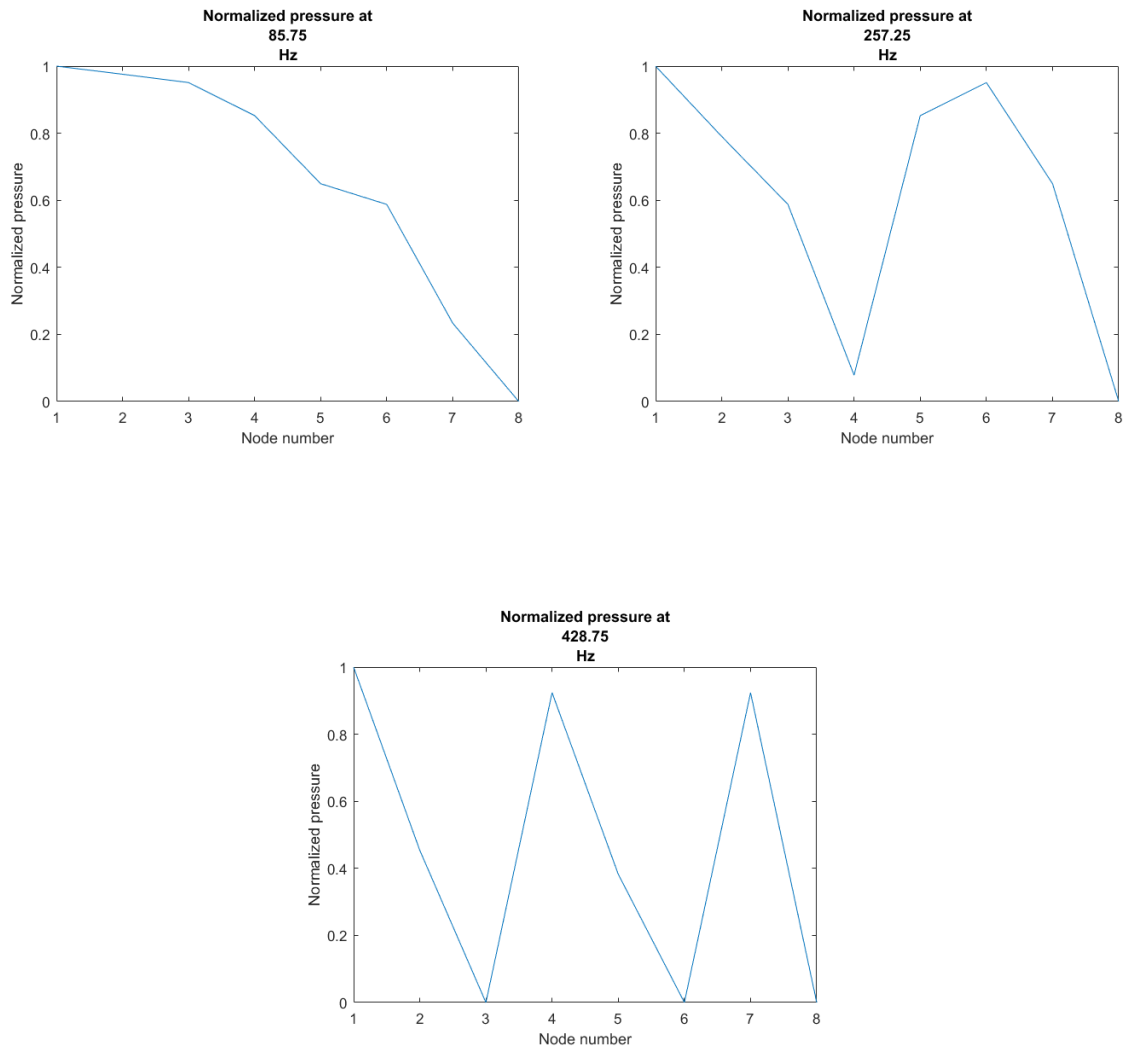


Figure D.5: Normalized pressure fluctuations evaluated at each node for the three found eigenfrequencies

In figure D.5 the normalized pressure fluctuations for the three eigenfrequencies are shown, the pressures are calculated at each node for all three frequencies. As can be seen, they show a wave like pattern. The plot for the first eigenfrequency shows a quarter-wave pattern, for the second eigenfrequency it shows a three-quarter-wave pattern and for the third eigenfrequency it shows a one and a quarter wave pattern. This corresponds to the wave pattern which is expected be found in a pipe with an open and a closed end. From D.5.c it is obvious that at 428.75 Hz, node 3 has a pressure minimum and thus does not show a resonance peak in figure D.3.

## Source influence

An arbitrary source strength of  $1 \cdot 10^{-7}$  kg/s was chosen for the first plots, see matrix (D.2). An increase in the absolute value of the pressure fluctuations should be shown if the source strength is increased to  $1 \cdot 10^{-5}$  kg/s. Figure D.6 clearly shows that for an increase in source strength the absolute value of the pressure fluctuation increase at all frequencies. All of this shows that the expected behaviour of a clarinet can be modelled using the Transfer Matrix Method. Where the eigenfrequencies can be calculated by finding the complex frequencies for which the matrix determinant equals zero and the pressure fluctuations can be found by solving the matrix system by inverting the system matrix and multiplying it with the source vector (D.4).

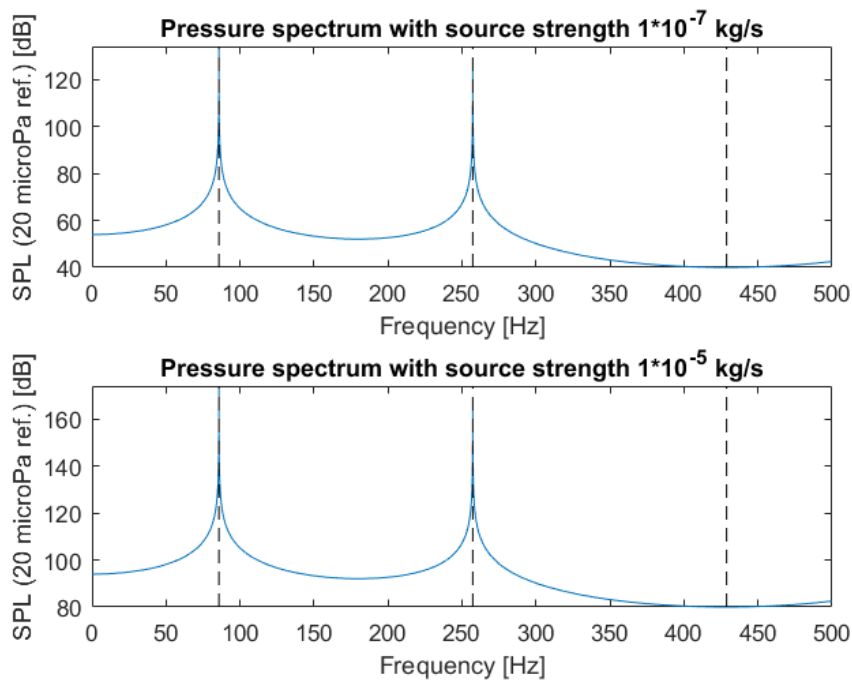


Figure D.6: Pressure spectrum at node 3 for varying source strength